

**Precision Measurement of Neutrino Oscillation Parameters with
KamLAND**

by

Daniel Andrew Dwyer

B.S. (Massachusetts Institute of Technology) 2000

M.A. (University of California, Berkeley) 2006

A dissertation submitted in partial satisfaction of the
requirements for the degree of
Doctor of Philosophy

in

Physics

in the

GRADUATE DIVISION

of the

UNIVERSITY OF CALIFORNIA, BERKELEY

Committee in charge:

Professor Stuart J. Freedman, Chair

Professor Hitoshi Murayama

Professor Chung-Pei Ma

Spring 2007

The dissertation of Daniel Andrew Dwyer is approved:

Chair

Date

Date

Date

University of California, Berkeley

Spring 2007

Precision Measurement of Neutrino Oscillation Parameters with
KamLAND

Copyright 2007

by

Daniel Andrew Dwyer

Abstract

Precision Measurement of Neutrino Oscillation Parameters with KamLAND

by

Daniel Andrew Dwyer

Doctor of Philosophy in Physics

University of California, Berkeley

Professor Stuart J. Freedman, Chair

Between Apr. 2002 and May 2006 KamLAND measured the electron antineutrino flux at the Kamioka mine (2700 *m.w.e.*) in Japan. The $\bar{\nu}_e$ sources were 19 Japanese nuclear reactor facilities at distances of 87 *km* to 830 *km*. Antineutrinos were detected by inverse beta decay, $\bar{\nu}_e + p \rightarrow e^+ + n$; detection of a positron and neutron pair constituted a neutrino signal. 1 *kton* of liquid scintillator served as both target and detector; the total exposure was 4.14×10^{34} *proton days*. In 1179.3 days of detector livetime, 550 antineutrino interactions were detected above a 3.4 *MeV* threshold, with an estimated 55 ± 18 from backgrounds. The number, spectrum, and time of the $\bar{\nu}_e$ signals support neutrino flavor oscillation with $\Delta m_{12}^2 = (7.72 \pm 0.24) \times 10^5 \text{ eV}^2$ and $\tan^2 \theta_{12} = 0.48 \pm 0.12$, in the Large Mixing Angle region. Assuming CPT invariance, KamLAND and solar neutrino results combined give $\Delta m_{12}^2 = (7.71 \pm 0.25) \times 10^5 \text{ eV}^2$ and $\tan^2 \theta_{12} = 0.49 \pm 0.05$.

Professor Stuart J. Freedman
Dissertation Committee Chair

●○○○○○○○○●●●○○○○●

○○●○○●●○○○○●○○●●

To Jackie

●●○○●○○●●○○●○○○○

○○●○○○○○○●○○●○○●

Contents

List of Figures	vi
List of Tables	ix
1 Introduction	1
1.1 A History of Missing Neutrinos	2
1.2 The Role of KamLAND	5
2 Theory of Neutrino Oscillation	7
2.1 Majorana Neutrinos	11
2.2 Matter Enhanced Neutrino Oscillations	13
3 Experimental History	17
3.1 Solar Neutrino Experiments	17
3.1.1 Homestake	21
3.1.2 SAGE	22
3.1.3 Gallex and GNO	22
3.1.4 Kamiokande	23
3.1.5 Super-Kamiokande	24
3.1.6 Sudbury Neutrino Observatory	25
3.1.7 Summary of Solar Neutrino Measurements	28
3.2 Reactor Neutrino Experiments	29
3.2.1 The Delayed-Coincidence Method	30
3.2.2 Hanford	32
3.2.3 Savannah River	32
3.2.4 Institut Laue-Langevin (ILL)	35
3.2.5 Gösgen	35
3.2.6 Rovno	36
3.2.7 Bugey	37
3.2.8 Krasnoyarsk	37
3.2.9 CHOOZ	38
3.2.10 Palo Verde	39

3.2.11	Reactor Experiment Summary	39
3.2.12	Spectral Distortion	40
4	The Kamioka Liquid Scintillator Anti-Neutrino Detector	41
4.1	Site Description	42
4.2	Detector Overview	42
4.2.1	Physical Detector Design	43
4.2.2	Detection Principle	43
4.2.3	The Scintillator	43
4.2.4	The Balloon	45
4.2.5	The Buffer Region	46
4.2.6	Photomultipliers	46
4.2.7	Magnetic Compensation Coils	47
4.2.8	Outer Detector	47
4.2.9	Chimney and Glove Box	47
4.2.10	Radioactive Calibration Sources	48
4.2.11	Z-Axis Calibration System	48
4.2.12	4π Calibration System	48
4.3	Data Acquisition System	50
4.3.1	The Front-End Electronics: Pass 1	52
4.3.2	The Trigger	53
4.3.3	The Front-End Electronics: Pass 2	55
4.3.4	Data Read-out	55
4.3.5	The Event Builder	55
4.3.6	KiNOKO	56
4.3.7	Data Volume and Lossless Data Compression	56
5	Determining the Antineutrino Flux from the Reactors	57
5.1	Reactor Power and Fission Rates	58
5.2	Antineutrino Flux By Isotope Fission	61
5.3	Inverse Beta Decay Cross Section	62
5.4	Positron Energy	62
6	Event Reconstruction	65
6.1	PMT Signal Processing	66
6.1.1	<i>Gain Filtering</i>	67
6.1.2	Pedestal Subtraction	68
6.1.3	Waveform Smoothing	68
6.1.4	Determining the ADC Offset	70
6.1.5	Pulse Finding	71
6.2	Event Classification	71
6.2.1	Low-level Event Classification	73
6.2.2	Event Types	76
6.3	Vertex Reconstruction	79
6.3.1	Position Calibration	80

6.4	Energy Reconstruction	82
6.4.1	Charge Probability Distribution	84
6.4.2	The Energy Likelihood Function	85
6.4.3	Energy Calibration	86
6.4.4	Energy Response Model	86
6.5	Muon Track Reconstruction	92
6.5.1	The “Fastest-Light” Model	92
6.5.2	“Fastest-Light” Likelihood and Minimization	94
6.5.3	Performance	95
7	Muon Spallation	97
7.1	Muon Rates	97
7.2	Spallation Neutrons	98
7.2.1	Neutron Energy Spectrum	99
7.2.2	Neutron Rate	101
7.2.3	Spatial Distribution of Neutron Capture Events	104
7.3	Boron and Nitrogen	106
7.3.1	^{12}B and ^{12}N Energy Spectrum	107
7.3.2	^{12}B Decay Rate	108
7.3.3	Spatial Distribution of ^{12}B Decay Events	109
7.4	Lithium and Helium	109
7.4.1	Decay Rate of ^9Li and ^8He	112
7.4.2	Energy Spectrum of ^9Li	112
7.4.3	Spatial Distribution of ^9Li Events	113
7.5	Showering Muons and Spallation Production	113
8	$\bar{\nu}_e$ Selection	116
8.1	Reactor Antineutrino Signal	116
8.2	Backgrounds	117
8.2.1	Accidental Coincidences	118
8.2.2	Muon Spallation	118
8.2.3	High-Energy Alpha Particle Correlated Background	120
8.2.4	Fast Neutrons	121
8.2.5	Geoneutrinos	122
8.3	Selecting Antineutrino Candidates	123
8.3.1	Reconstruction Quality	123
8.3.2	Prompt-Delayed Event Time Separation	123
8.3.3	Prompt-Delayed Event Spatial Separation	124
8.3.4	Prompt and Delayed Interaction Energies	126
8.3.5	Target Volume Selection	128
8.3.6	Muon Spallation	131
8.3.7	Antineutrino Candidate Events	132
8.4	Residual Background Estimation	135
8.4.1	Accidental Coincidences	135
8.4.2	^9Li Background	135

8.4.3	$^{13}\text{C}(\alpha,n)$ -induced Backgrounds	137
8.4.4	Fast Neutrons	140
8.4.5	Background Summary	143
8.5	Detector Exposure	144
8.5.1	Livetime	144
8.5.2	Proton Density	144
8.5.3	Target Volume	145
8.5.4	Muon Spallation	158
8.5.5	Exposure Summary	158
9	Antineutrino Oscillation Analysis	160
9.1	The Likelihood Model	161
9.1.1	Nuisance Parameter Penalty	163
9.1.2	Rate Term	163
9.1.3	Unbinned Spectral Shape Likelihood	164
9.1.4	Unbinned Spectral Shape and Time Likelihood	164
9.2	Analysis Details	165
9.2.1	Best Fit Parameter Estimation	165
9.2.2	Goodness-of-fit Determination	165
9.2.3	Confidence Regions	165
9.3	Rate and Shape Analysis	166
9.4	Rate, Shape, and Time Analysis	168
9.5	Global Analysis	169
10	Conclusions	172
	Bibliography	174
A	Lossless Compression of Waveform Data	184
A.1	Summary	184
A.2	Introduction	185
A.3	Compression Method	185
A.3.1	Entropy Reduction	186
A.3.2	Entropy Encoding	187
A.4	Compression Results	188
A.4.1	Entropy Reduction Results	188
A.4.2	Entropy Encoding Results	188
A.4.3	Speed and Reliability	189
A.5	Implementation for KamLAND	189

List of Figures

2.1	Two-flavor Oscillation Signature	10
2.2	Solar Neutrino Matter-Enhanced Oscillation	16
3.1	Solar Neutrino Energy Spectrum	20
3.2	SNO Solar Neutrino Flux	28
3.3	Solar Neutrino Measurements	29
3.4	Delayed-Coincidence Signal	31
3.5	Herr Auge	33
3.6	Savannah River Signals	34
3.7	Reactor Flux Measurements	40
4.1	The KamLAND Detector	44
4.2	Z-axis Calibration	49
4.3	4π Calibration	51
4.4	Data Acquisition	52
4.5	Front-End Electronics Board	54
5.1	Estimated Reactor Antineutrino Flux	60
5.2	Reactor Antineutrino Spectra	61
5.3	Inverse Beta Decay Cross-Section	63
5.4	Positron Event Energy Spectrum	64
6.1	PMT Waveform	66
6.2	Waveform Gains	68
6.3	Waveform Processing	69
6.4	PMT Pulse Area	72
6.5	Inner Detector Light Distribution	74
6.6	Outer Detector n_{summax} vs. Inner Detector Light	75
6.7	Outer vs. Inner Detector n_{summax}	77
6.8	Calibration Source Position	82
6.9	Vertical Position Reconstruction	83
6.10	Position Resolution	83
6.11	Calibration Source Energy	87

6.12	Energy Calibration Over Time	87
6.13	Z-Axis Energy Bias	88
6.14	Off-Axis Energy Bias	88
6.15	Energy Response Model	90
6.16	Energy Resolution Model	91
6.17	Muon Scintillation Light Model	93
6.18	Muon PMT Hit Time Probability	94
6.19	Muon Track Reconstruction	96
7.1	Muon Rates	98
7.2	Neutron Capture Spectrum	100
7.3	Neutron Capture Spectrum at Late Times	101
7.4	Neutron Capture Time	103
7.5	Detector Biases to Neutron Capture Time	103
7.6	Multiplicity of Events Following Muons	104
7.7	Low-multiplicity Neutron Capture Time	105
7.8	Neutron Capture Radial Distribution	105
7.9	^{12}B and ^{12}N Decay Scheme	106
7.10	^{12}B Decay Spectral Fit	107
7.11	^{12}B Decay Rate	108
7.12	^{12}B Decay Radial Distribution	109
7.13	^9Li Decay Scheme	110
7.14	^8He Decay Scheme	111
7.15	^9Li Decay Rate	112
7.16	^9Li Decay Spectrum	113
7.17	^9Li Radial Distribution	114
7.18	Spallation Production and Muon Light	115
8.1	Singles Events Position Distribution	119
8.2	Singles Events Energy Spectrum	120
8.3	Geoneutrino Spectrum	122
8.4	Event Reconstruction Efficiency	124
8.5	Time between Prompt and Delayed Events	125
8.6	Estimated Distance between Prompt and Delayed Events	127
8.7	Distance between Prompt and Delayed Events	128
8.8	Energy of Prompt and Delayed Events	129
8.9	Antineutrino Event Distribution in the Detector Volume	130
8.10	^9Li Background in Reactor $\bar{\nu}_e$ Signal	131
8.11	^9Li Background by Muon Type	133
8.12	^{12}B Distance from Muon	134
8.13	Accidental Coincidence Prompt Energy Spectrum	136
8.14	^9Li Background Estimate	136
8.15	^{210}Po α Energy Peak	138
8.16	α Ranging in KamLAND Liquid Scintillator	139
8.17	$^{13}\text{C}(\alpha,n)$ Neutron Kinetic Energy Spectrum	139

8.18	$^{13}\text{C}(\alpha,n)$ Visible Energy Spectrum	140
8.19	Time Spectrum after OD Muons	141
8.20	Neutron Capture Time from OD Muons	142
8.21	Fast Neutron Energy Spectrum	143
8.22	Fiducial Volume Ratio vs. Visible Energy	147
8.23	4π Measurement Method	149
8.24	4π Pin-to-pin Distances	150
8.25	4π Center-to-tip Measurement	150
8.26	4π Accessible Region	151
8.27	Angular Variation of Radial Position Bias	152
8.28	Energy Dependence of Radial Bias: ^{68}Ge On-Axis	154
8.29	Energy Dependence of Radial Bias: ^{68}Ge Off-Axis	155
8.30	Energy Dependence of Radial Bias: ^{241}Am - ^9Be On-Axis	156
8.31	Energy Dependence of Radial Bias: ^{241}Am - ^9Be Off-Axis	156
8.32	Energy Dependence of Radial Bias: ^{210}Po - ^{13}C Off-Axis	157
9.1	Rate and Shape Best Fit Spectrum	166
9.2	Rate and Shape Confidence Intervals	167
9.3	Two-flavor Oscillation Signature	168
9.4	L over E Oscillation Signature	169
9.5	Rate, Shape and Time Confidence Intervals	170
9.6	KamLAND + Solar Confidence Intervals	171

List of Tables

3.1	ν_e Detection Methods	19
4.1	Scintillator Composition By Isotope	45
4.2	Calibration Sources	48
5.1	Reactor Sites	59
6.1	Vertex Reconstruction Status	81
6.2	Energy Reconstruction Status	86
6.3	Energy Model Parameters	91
7.1	Summary of Muon Rates	98
7.2	Thermal Neutron Interactions By Isotope	99
8.1	Reactor Antineutrino Event Selection Efficiencies	134
8.2	Summary of Expected Backgrounds	143
8.3	4π $r = 5.5$ m Radial Bias Systematic Uncertainties	153
8.4	4π $r = 5.5$ m Radial Bias Measurements	157
8.5	4π Target Volume Measurements	157
8.6	Summary of Detector Exposure	158
8.7	Summary of Exposure Systematic Uncertainties	159
8.8	Summary of $\bar{\nu}_e$ Signal Systematic Uncertainties	159
9.1	Oscillation Likelihood Terms	162
A.1	Standard Compression Results	185
A.2	Waveform Entropy	188

Acknowledgments

Many have supported me while working on the research presented here. First and foremost thanks go to Patrick Decowski for constant advice and encouragement. I owe Stuart Freedman for giving me the opportunity to work on KamLAND and for supporting me over the past six years. I survived graduate school due to my partner in crime, Lindley Winslow, and the hardworking example she set. Tommy O'Donnell deserves much for the work he contributed as well as the levity he brought to our group. I am forever indebted to Brian Fujikawa for showing me how physics is done properly. Lauren Hsu is owed for her persistent attempts to bring order to our research. Bruce Berger provided an endless source of all knowledge of KamLAND. With Herculean effort Kazumi Tolich reviewed my analysis in detail, though any remaining errors are my fault only. Hopefully my fiancée Jackie will forgive me for all the neglect over recent years. She has shown infinite patience as I gave all my attention to research. My family has also been supportive and understanding, asking nothing in return even as they face more daunting challenges. Lastly, I owe all those who do the real work every day so that I can spend my time exploring the nature of things.

Chapter 1

Introduction

The Kamioka Liquid Scintillator Antineutrino Detector (KamLAND) was designed to measure neutrino properties. In particular, the experiment provides a precise, indirect measurement of neutrino mass. For most of this century the neutrino was assumed to be massless, yet a number of unexpected experimental results hinted at a non-zero mass. The results presented here provide strong evidence for massive neutrinos. Understanding the character of this fundamental particle not only impacts physics at the subatomic level, but also affects our understanding of the Sun and the structure of the Universe.

KamLAND is able to detect antineutrinos, $\bar{\nu}$, specifically those emitted by nuclear reactors. This thesis describes a measurement of antineutrinos which have traveled an average distance of 200 *km* to the KamLAND detector from 19 reactor facilities located across Japan. The detected rate and energy spectrum of the antineutrinos provide information about their mass. The measurement is not sensitive to the absolute mass of the neutrino, only the differences of the squared masses of neutrino states. In the context of this relation-

ship, the precise results of KamLAND imply a non-zero neutrino mass. Furthermore, the results provide the strongest evidence so far obtained for *neutrino oscillation*, a phenomenon requiring massive neutrinos and quantum mechanical mixing.

Before discussing the KamLAND reactor antineutrino experiment and its results, the following section provides a concise history of neutrino physics. A detailed discussion of the theory of massive neutrinos is given in Chap. 2. A closer look at previous reactor and solar neutrino experiments is found in Chap. 3. The KamLAND experiment and results are described in Chap. 4 through Chap. 10.

1.1 A History of Missing Neutrinos

The neutrino is the most elusive of the observed fundamental particles. The experimental story of this particle is punctuated by puzzling experimental results. Chadwick showed in 1914 that energy was apparently not conserved in beta decays, because the energy of the emitted beta particle from ^{214}Pb decay was continuously distributed instead of discrete. To avoid giving up the fundamental principle of energy conservation, in 1930 Pauli proposed the existence of a nearly undetectable neutral particle to explain the missing energy [72]. This invisible particle (which Pauli named the *neutron*) was responsible for carrying away the missing energy. Three years later, Fermi developed a model for beta decay using Pauli's idea, renaming the particle the *neutrino* [45, 44]. (In the intervening years the name *neutron* had been taken over for the nucleon that we now know.)

The next two decades provided no direct experimental evidence for the neutrino. According to Fermi's theory, the probability for a neutrino to interact was exceedingly

small. Detection required an intense neutrino source and a very sensitive detector. In 1953, Reines and Cowan exploited the 10^{19} antineutrinos per second emitted from a nuclear reactor providing the first tentative evidence for the existence of the neutrino [76]. The required detection selectivity was achieved by relying on the process of inverse beta decay, which produces a unique signal that is easily separated from background events. With an improved experiment at the Savannah River reactor, Reines and Cowan obtained convincing evidence of the neutrino in 1956 [38].

Experiment then shifted to a different neutrino source: the Sun. The first solar experiment was done at Homestake by Ray Davis [36]. Unfortunately, the benefits of the inverse beta decay signal are not applicable to solar experiments. The Sun is expected to produce neutrinos which must be detected using other reactions¹. To cope with backgrounds, solar neutrino detectors are very large, very clean, and very deep underground. They must be large enough to detect the rare solar neutrino interactions, while avoiding backgrounds due to radioactive contamination and cosmic rays. Davis first detected solar neutrinos in 1968, but the rate was only 1/3 of that expected according to the then current model of nuclear fusion in the Sun. This deficit came to be known as the *solar neutrino problem*. At the time, it was uncertain whether the discrepancy was due to experimental difficulties, a misunderstanding of solar physics, or properties of the neutrino itself.

Neutrinos from the Sun or nuclear reactors are only produced in conjunction with electrons or positrons. In 1962, an experiment at Brookhaven showed that there was a

¹Only antineutrinos interact via inverse beta decay with the proton. The neutrinos produced in the Sun could interact via inverse beta decay with the antiproton, $\nu_e + \bar{p} \rightarrow e^- + \bar{n}$, but an experimental target of antiprotons is not easily assembled.

different type of neutrino associated with muons [39]. In 2000, the DONUT experiment provided evidence of yet a third type of neutrino paired with the previously discovered tau lepton [64]. Neutrino states associated with the charged leptons are denoted by *flavor*: electron, muon, or tau.

Neutrinos are also produced by cosmic ray interactions with the Earth's atmosphere. Pion decay, $\pi \rightarrow \mu\nu_\mu$, followed by muon decay, $\mu \rightarrow e\nu_e\nu_\mu$, give an expected ratio of approximately two muon neutrinos for every electron neutrino. Early discrepancies with this prediction were observed in a number of underground proton decay experiments. Given the weakness of neutrino interactions, essentially all of the atmospheric neutrinos easily pass through the Earth. Therefore, for a given solid angle, a detector placed on one side of the Earth is expected to see an equal number of neutrinos coming from the atmosphere above it and below it. Two experiments capable of detecting these neutrinos, the Kamiokande² (1988) [56] and IMB³ (1991) experiments, both found a deviation of the total number of muon-to-electron neutrinos observed [33, 28]. The Super-Kamiokande experiment, similar to the Kamiokande but 25 times larger, proved by measuring the angular distribution that the deficit was in muon neutrinos coming up from the other side of the Earth [50]. The question became why are the muon neutrinos but not electron neutrinos disappearing as they travel the extra distance through the Earth.

Through the final decades of the twentieth century, the evidence for solar and atmospheric neutrino deficits grew stronger. In contrast, experiments using reactor and accelerator neutrinos failed to see any deficits. The LSND experiment reported evidence of

²Kamioka Nucleon Decay Experiment

³Irvine, Michigan, Brookhaven Experiment

electron neutrino *appearance* in a beam of muon neutrinos in 1996 [22]; recent results from the MiniBooNE experiment do not support this result [7].

In 2002, the Sudbury Neutrino Observatory (SNO) presented a clear picture of the solar neutrino problem [9, 10]. In the reaction $d + \nu_e \rightarrow p + p + e$ reaction, which is only sensitive to electron neutrinos, SNO measured a deficit. In $d + \nu \rightarrow n + n$, which is sensitive to all three neutrino flavors, the experiment measured a total flux consistent with the Standard Solar Model [24]. The solar neutrino problem was clearly due to neutrino flavor change.

The new challenge was to explain the physical process that converted electron neutrinos produced in the Sun to muon and tau neutrinos at the Earth, compatible with other neutrino experiments. A consistent explanation is provided by the theory of neutrino oscillation, described in Chap. 2.

1.2 The Role of KamLAND

The KamLAND experiment is well-positioned to test the theory of neutrino oscillation. Previous reactor neutrino experiments and a well-developed model of fission reactors has shown that the rate and energy spectrum of reactor antineutrinos are understood to 2%.

Moreover, oscillation is expected to leave a clear signature in the neutrino energy spectrum. Solar and atmospheric experiments provide a limited measurement of the neutrino energy. Reactor neutrino experiments provide a more direct measurement of the antineutrino energy spectrum, and have the capability to reveal the effect of oscillation.

Solar and reactor neutrino oscillation is a two-state mixing problem described by two physical parameters: the mixing angle θ_{12} and the difference of the squared masses Δm_{12}^2 . These parameters are chosen by nature and determined by experiment. Assuming neutrino oscillation is the solution to the solar neutrino problem, only a limited range of values are allowed by experiment. One region of allowed values, corresponding to $\sin^2 2\theta_{12} \sim 1$ and $10^{-6} eV^2 < \Delta m_{12}^2 < 10^{-3} eV^2$, is referred to as the Large Mixing Angle (LMA) solution. The LMA solution would produce a clear oscillation signal in the KamLAND experiment. KamLAND can either confirm or exclude the LMA solution to the solar neutrino problem. By confirming LMA, it can rule out all other solutions.

Massive neutrinos are a necessary condition for neutrino oscillation. By demonstrating a clear oscillation signal, KamLAND provides evidence of neutrino mass. The remainder of this thesis describes the KamLAND measurement and the results, which support oscillation of massive neutrinos and the LMA solution of the solar neutrino problem.

Chapter 2

Theory of Neutrino Oscillation

The basic idea of neutrino oscillation was proposed in 1957 when Pontecorvo considered the possibility of neutrino-antineutrino oscillation, a phenomenon similar to the oscillation in the neutral kaon system. In 1962, Maki, Nakagawa, and Sakata expanded on Pontecorvo's idea, introducing the theory of neutrino flavor oscillation. Flavor oscillation accounts for the possible conversion between electron, muon and tau neutrinos. When solar neutrino experiments measured a deficit in the electron neutrino flux, flavor oscillation became a possible explanation. The discussion here follows that of Ref. [60].

In this theory, two conditions are necessary for flavor transition. First, the neutrino mass eigenvalues cannot all be equal. This condition implies at least one massive neutrino eigenstate. Second, the neutrino mass eigenstates must not be equivalent to the weak interaction (flavor) eigenstates.

The neutrino mass eigenstates can be written as ν_1 , ν_2 , and ν_3 associated with masses m_1 , m_2 , and m_3 respectively. The flavor eigenstates are expressed as ν_e , ν_μ , and

ν_τ . To satisfy the first condition, at least one of the masses m_i must be different from the other masses. For the second condition, at least two flavor eigenstates ν_f are different from the mass eigenstates. In general, a flavor eigenstate is written as a linear combination of the mass eigenstates,

$$|\nu_f\rangle = \sum_i U_{fi}^* |\nu_i\rangle. \quad (2.1)$$

Here, U_{fi} is a unitary matrix relating the mass eigenstates i to the flavor eigenstates f .

Considering a neutrino in a mass eigenstate in its rest frame at proper time τ , it will obtain a phase determined by its rest mass, in units of \hbar and c equal to 1,

$$|\nu_i(\tau)\rangle = e^{-im_i\tau} |\nu_i(0)\rangle. \quad (2.2)$$

Shifting this phase to the lab frame (time t , distance L) under the assumption that the neutrino energy E_i is much greater than its mass,

$$m_i\tau = E_it - p_iL = E_it - \sqrt{E_i^2 - m_i^2}L \quad (2.3)$$

$$\simeq E_i(t - L) + \frac{m_i^2L}{2E_i}. \quad (2.4)$$

The amplitude that an electron neutrino remains in an electron neutrino state after traveling a distance L in the lab frame is then,

$$\text{Amp}(\nu_e \rightarrow \nu_e) = \sum_i U_{ei}^* e^{-i\frac{m_i^2L}{2E_i}} U_{ei}. \quad (2.5)$$

Considering a simple two-flavor mixing model (ignoring the tau neutrino) is instructive. In this case, the two-by-two unitary mixing matrix U is parameterized with a single variable θ_{12} ,

$$\begin{pmatrix} \nu_e \\ \nu_\mu \end{pmatrix} = \begin{pmatrix} \cos\theta_{12} & \sin\theta_{12} \\ -\sin\theta_{12} & \cos\theta_{12} \end{pmatrix} \begin{pmatrix} \nu_1 \\ \nu_2 \end{pmatrix}. \quad (2.6)$$

The probability of detecting an electron neutrino as an electron neutrino after it has traveled a distance L is,

$$P(\nu_e \rightarrow \nu_e) = |Amp(\nu_e \rightarrow \nu_e)|^2 \quad (2.7)$$

$$= 1 - \sin^2 2\theta_{12} \sin^2 \frac{\Delta m_{12}^2 L}{4E}, \quad (2.8)$$

where,

$$\Delta m_{12}^2 = m_1^2 - m_2^2. \quad (2.9)$$

It is clear that the wavelength of the flavor oscillations are determined by the difference of the squared masses Δm_{12}^2 , and the amplitude is determined by the mixing parameter θ_{12} . Reintroducing \hbar and c , the oscillation length L_{osc} ¹ for a neutrino of energy E is,

$$L_{osc} \equiv \frac{4\pi E \hbar c}{\Delta m_{12}^2}, \quad (2.10)$$

$$\simeq \frac{2.48 E (\text{MeV})}{\Delta m_{12}^2 (\text{eV}^2)} \text{ meters}. \quad (2.11)$$

Figure 2.1(a) shows the signature of neutrino oscillation according to Eq. 2.8. An electron neutrino of energy E (MeV) is produced and travels to a detector at distance L . The probability that it is detected as an electron-type neutrino oscillates with distance. The period of the oscillation is determined by Δm_{12}^2 , while the amplitude is given by $\sin^2 2\theta_{12}$. Figure 2.1(b) shows the combination of oscillation signals from two sources. The oscillatory signal is reduced after a few oscillation lengths when the signal from multiple sources cannot be separated. The case of combined sources is representative of the KamLAND experiment, where the signal is from multiple sources at a range of distances.

¹The oscillation length is half the wavelength.

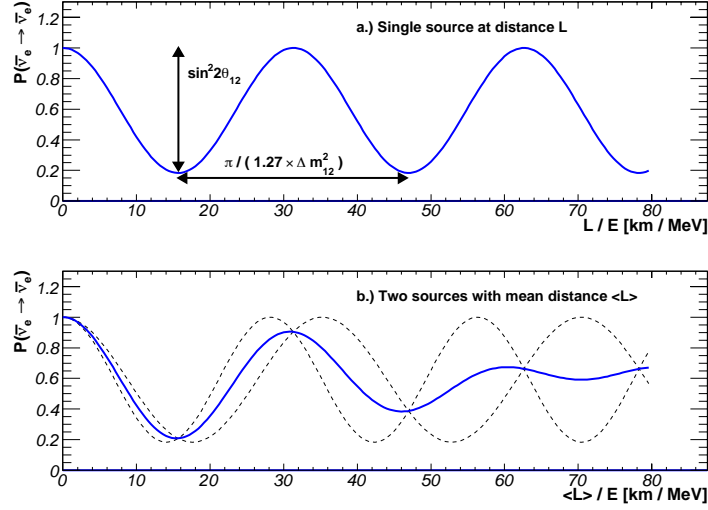


Figure 2.1: a.) The electron neutrino survival probability shown versus the propagation distance L divided by the neutrino energy E . b.) The combined survival probability due to two neutrino sources at different distances from the detector.

Because of the pattern of neutrino masses realized in nature, two state mixing usually dominates in a given experiment, and the expression above is often sufficient. The three-flavor case requires three mixing angles (θ_{12} , θ_{23} , θ_{13}), and a CP-violating phase δ to fully parameterize the mixing matrix. This full three-flavor mixing matrix is commonly decomposed into the product of four matrices,

$$\begin{aligned}
 U_{if} = & \begin{pmatrix} 1 & 0 & 0 \\ 0 & c_{23} & s_{23} \\ 0 & -s_{23} & c_{23} \end{pmatrix} \times \begin{pmatrix} c_{13} & 0 & s_{13}e^{-i\delta} \\ 0 & 1 & 0 \\ -s_{13}e^{i\delta} & 0 & c_{13} \end{pmatrix} \times \begin{pmatrix} c_{12} & s_{12} & 0 \\ -s_{12} & c_{12} & 0 \\ 0 & 0 & 1 \end{pmatrix} \\
 & \times \begin{pmatrix} e^{i\alpha_1/2} & 0 & 0 \\ 0 & e^{i\alpha_2/2} & 0 \\ 0 & 0 & 1 \end{pmatrix} \quad (2.12)
 \end{aligned}$$

In this expansion, $c_{ij} \equiv \cos \theta_{ij}$ and $s_{ij} \equiv \sin \theta_{ij}$. The first three matrices parameterize

two-flavor mixing between two mass eigenstates similar to Eq. 2.6. When combined, the resulting 3×3 matrix accounts for the full three-flavor mixing, except for the possibility of an off-diagonal complex phase. By convention, this complex phase δ is inserted into the second sub-matrix. The fourth matrix in the expansion is necessary if the neutrino is a Majorana particle as opposed to a Dirac particle; the details of this will be discussed in the following section. In any case, the Majorana phases do not effect neutrino oscillation.

This factorization of the mixing matrix separates the terms relevant for different experiments. Experiments measuring neutrinos produced in the atmosphere have the greatest sensitivity to θ_{23} which is only present in the first matrix. Short-distance reactor neutrino experiments and moderate-distance accelerator experiments measure θ_{13} present in the second matrix. Solar neutrino and long-distance reactor experiments are predominantly sensitive to θ_{12} . Since the KamLAND experiment measures reactor neutrinos which have traveled a long distance, the analysis presented here mostly concerns the third matrix.

2.1 Majorana Neutrinos

According to Dirac's theory, every spin- $\frac{1}{2}$ fermion is associated with an antimatter partner. A massive neutrino can be added to the Standard Model in two ways. If the neutrino is a Dirac particle, then the antiparticle is distinct. If it is a Majorana particle, then the antiparticle is identical to the neutrino. Although all other fermions in the Standard Model are Dirac particles, it is theoretically attractive to have Majorana neutrinos. With no electric charge, the neutrino is unique relative to the other leptons and quarks. Since an antiparticle has the opposite charge, neutrality is a requirement for Majorana particles.

Leptons and quarks have masses on the order of 1 to $10^5 MeV$, but neutrino masses are at least 6 orders of magnitude smaller. A process referred to as the *see-saw* mechanism gives a plausible story for how Majorana neutrinos obtain especially small masses. For every Dirac particle, there are four states: two helicity states (R and L) for the particle and its antiparticle. These states may be written $|\nu_R\rangle$, $|\bar{\nu}_R\rangle$, $|\nu_L\rangle$, and $|\bar{\nu}_L\rangle$. For a Majorana neutrino, the state $|\nu_h\rangle$ is equivalent to the antineutrino state $|\bar{\nu}_h\rangle$ of the same helicity h .

With this knowledge, the parameterization of the neutrino mixing matrix U is easily understood. In the two flavor mixing case (Eq. 2.6), a generic complex matrix may be written using four real numbers and four phase angles. Given that the mixing matrix must be unitary, this produces three real constraints and one phase constraint. In quantum theory, each particle state has an unmeasurable imaginary phase. The arbitrary phase can be used to absorb some phases from the mixing matrix. If the two neutrino mass eigenstates are Dirac, then four phases may be absorbed, leaving a common unobservable phase. This results in a mixing matrix that may be described with a single real parameter, the mixing angle θ . For a Majorana neutrino, only three phases may be absorbed into the particle states. This leaves one phase in the 2×2 mixing matrix.

A similar argument is used for the 3×3 mixing matrix. In this case, three real parameters and one phase are sufficient for the Dirac case. The fourth matrix in the expansion given in Eq. 2.12 accounts for the possibility that the neutrino is a Majorana particle by introducing two additional complex phases α_1 and α_2 in the mixing matrix.

2.2 Matter Enhanced Neutrino Oscillations

The propagation of neutrinos in vacuum is naturally described in terms of the mass eigenstates. Neutrino propagation in matter is conveniently described in terms of the flavor eigenstates. This process was first described by Wolfenstein [86]; the possibility of resonant oscillation in matter was later explored by Mikheev and Smirnov [67]. Accordingly, matter-enhanced neutrino oscillation is often referred to as the MSW effect.

While traversing matter, neutrinos will interact with electrons by both neutral current (NC) and charged current interactions (CC), obtaining an effective potential energy that depends on flavor. The strength of this interaction is proportional to the Fermi coupling constant G_F and the density of electrons N_e in the matter. The Standard Model provides the numerical coefficients for the effective potential energies,

$$V_{NC} = -\frac{\sqrt{2}}{2}G_F N_e, \quad (2.13)$$

$$V_{CC} = \sqrt{2}G_F N_e. \quad (2.14)$$

The neutral current interaction affects all neutrino flavors equally. Since ordinary matter is composed of electrons, but not muon or tau particles, the charged current interaction will only occur for electron neutrinos. Using the same two-flavor basis as Eq. 2.6, the Hamiltonian of the system is,

$$H = H_{vac} + V_{CC} \begin{pmatrix} 1 & 0 \\ 0 & 0 \end{pmatrix} + V_{NC} \begin{pmatrix} 1 & 0 \\ 0 & 1 \end{pmatrix}. \quad (2.15)$$

Any multiple of the identity matrix may be subtracted from the Hamiltonian since this corresponds to a constant potential which produces no detectable result. Therefore, the NC

component is discarded and the CC component is altered,

$$H = H_{vac} + \frac{V_{CC}}{2} \begin{pmatrix} 1 & 0 \\ 0 & -1 \end{pmatrix}. \quad (2.16)$$

The vacuum component of the Hamiltonian, H_{vac} , is diagonal in the mass eigenstates.

Written in terms of the flavor eigenstates, this becomes,

$$H_{vac} = \frac{\Delta m^2}{4E} \begin{pmatrix} -\cos 2\theta & \sin 2\theta \\ \sin 2\theta & -\cos 2\theta \end{pmatrix}. \quad (2.17)$$

By introducing the parameter x ,

$$x \equiv \frac{2\sqrt{2}G_F N_e E}{\Delta m^2}, \quad (2.18)$$

the sum of the vacuum and matter components can be written,

$$H = \frac{\Delta m^2}{4E} \begin{pmatrix} -\cos 2\theta + x & \sin 2\theta \\ \sin 2\theta & -\cos 2\theta - x \end{pmatrix}. \quad (2.19)$$

The physical impact of including the neutrino interactions with matter can be seen by writing H in terms of the parameters,

$$\Delta m_M^2 \equiv \Delta m^2 \sqrt{\sin^2 2\theta + (\cos 2\theta - x)^2} \quad (2.20)$$

and

$$\sin^2 2\theta_M \equiv \frac{\sin^2 2\theta}{\sin^2 2\theta + (\cos 2\theta - x)^2}. \quad (2.21)$$

The full Hamiltonian is then,

$$H_{vac} = \frac{\Delta m_M^2}{4E} \begin{pmatrix} -\cos 2\theta_M & \sin 2\theta_M \\ \sin 2\theta_M & -\cos 2\theta_M \end{pmatrix}. \quad (2.22)$$

Therefore, matter alters the effective mixing angle and difference of the squared masses to θ_M and Δm_M^2 . If the electron density is approximately constant between the neutrino source and detector, the case for KamLAND, then the description above is sufficient to analyze the experimental results using,

$$P(\nu_e \rightarrow \nu_e) = 1 - \sin^2 2\theta_M \sin^2 \frac{\Delta m_M^2 L}{4E}, \quad (2.23)$$

which is Eq. 2.7 including matter effects. The size of the matter effect is determined by the parameter x (Eq. 2.18). For oscillation parameters from the LMA region probed by KamLAND, the electron density in the Earth, and the energy of reactor antineutrinos gives $x \ll 1$. Therefore, the matter effect is very small for KamLAND.

For the neutrinos produced in the dense core of the Sun and which travel to Earth, the electron density varies greatly. In this case, the change of θ_M and Δm_M^2 must be considered. In Ref. [23], the survival probability $P(\nu_e \rightarrow \nu_e)$ is calculated as a function of solar neutrino energy (Fig. 2.2). This calculation is appropriate for parameters in the LMA region. At energies below an MeV , the matter effect does not enhance the oscillation probability. At an energy of roughly $2 MeV$, there is a transition to matter-enhanced oscillation. This calculation is appropriate for neutrinos detected during the daytime. During the night there is an additional effect due to the Earth, which may be detected by comparing the day and night signals.

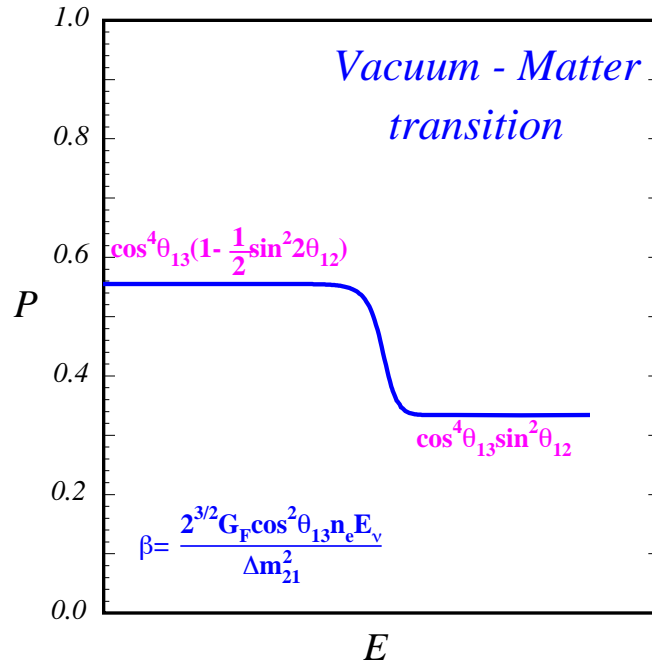


Figure 2.2: The matter-enhanced survival probability $P(\nu_e \rightarrow \nu_e)$ as a function of solar neutrino energy. The neutrino oscillation parameters lie in the LMA region. At energies below an MeV , the matter effect does not enhance the oscillation probability. At an energy of roughly $2 MeV$, there is a transition to matter-enhanced oscillation. Figure is taken from [23].

Chapter 3

Experimental History

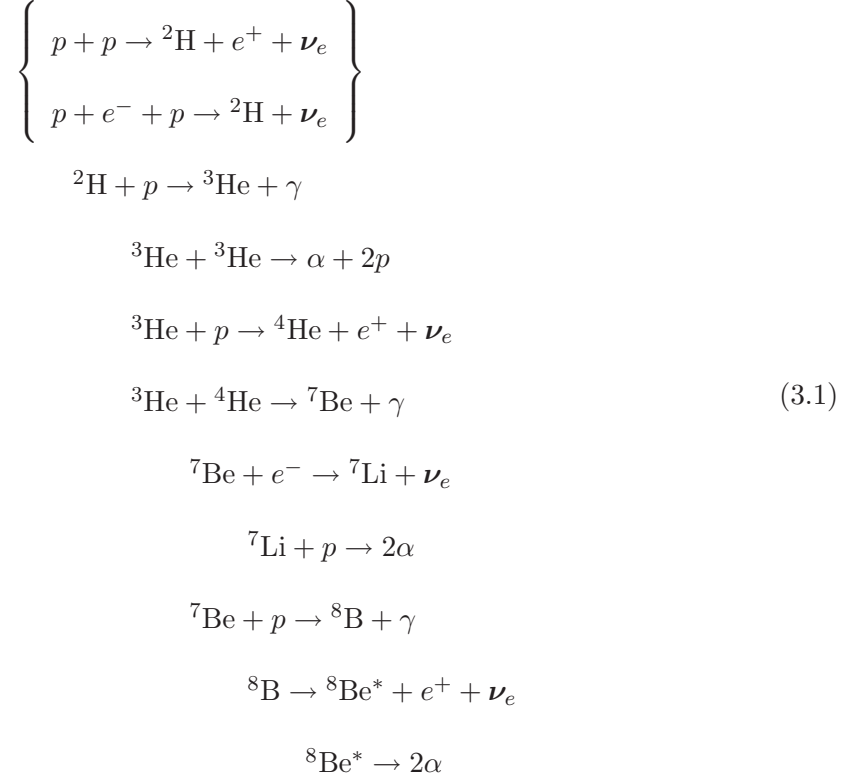
A review of selected neutrino oscillation experiments is discussed in this chapter. Atmospheric, accelerator, and other neutrino experiments have probed neutrino properties, but the following discussion will focus on reactor and solar experiments. The experimental results relevant to the solar neutrino problem are followed by the results of reactor experiments. These results provided the motivation for the KamLAND experiment.

3.1 Solar Neutrino Experiments

Following the puzzling conclusions of the Homestake experiment, a series of experiments attempted to resolve the solar neutrino problem.

The solar fusion processes are dominated by the reactions in Eq. 3.1 which convert four protons into ${}^4\text{He}$. This reaction is called the proton-proton, or pp , chain. The rates for each reaction are determined by the cross-sections and the conditions of the solar interior.

The neutrino producing reactions are highlighted by the bolded neutrino.

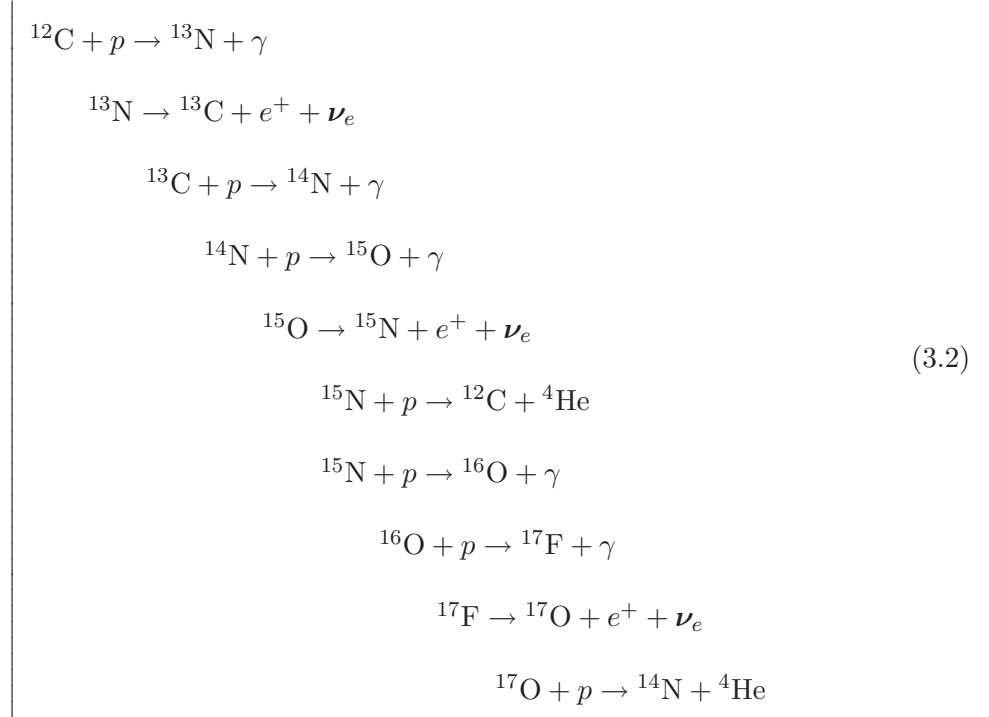


The Carbon-Nitrogen-Oxygen, or *CNO*, cycle is shown in Eq. 3.2. A ${}^{12}\text{C}$ nucleus catalyzes the conversion of four protons into ${}^4\text{He}$. An estimated 2% of the Sun's helium is produced

Table 3.1: Solar ν_e detector energy thresholds. For gallium and chlorine experiments, the threshold is set by nuclear kinematics. For the water Čerenkov detectors, the threshold is limited by the background, which grows rapidly below 5 MeV [31].

Detector	Threshold [MeV]
^{71}Ga	0.236
^{37}Cl	0.813
H_2O	~ 5
D_2O	~ 5

in the *CNO* cycle.



The *Standard Solar Model* [24, 25], estimates the rate of reactions in each branch.

Fig. 3.1 shows the predicted neutrino energy spectrum. Depending on the detection method, solar neutrino experiments are sensitive to different ν_e energy ranges (Table 3.1). The water Čerenkov detectors see only a small piece of the ν_e flux from the decay of ^8B . Only the ^{71}Ga detectors are able to detect part of the *pp* neutrinos, which account for more than 90% of the solar neutrino flux.

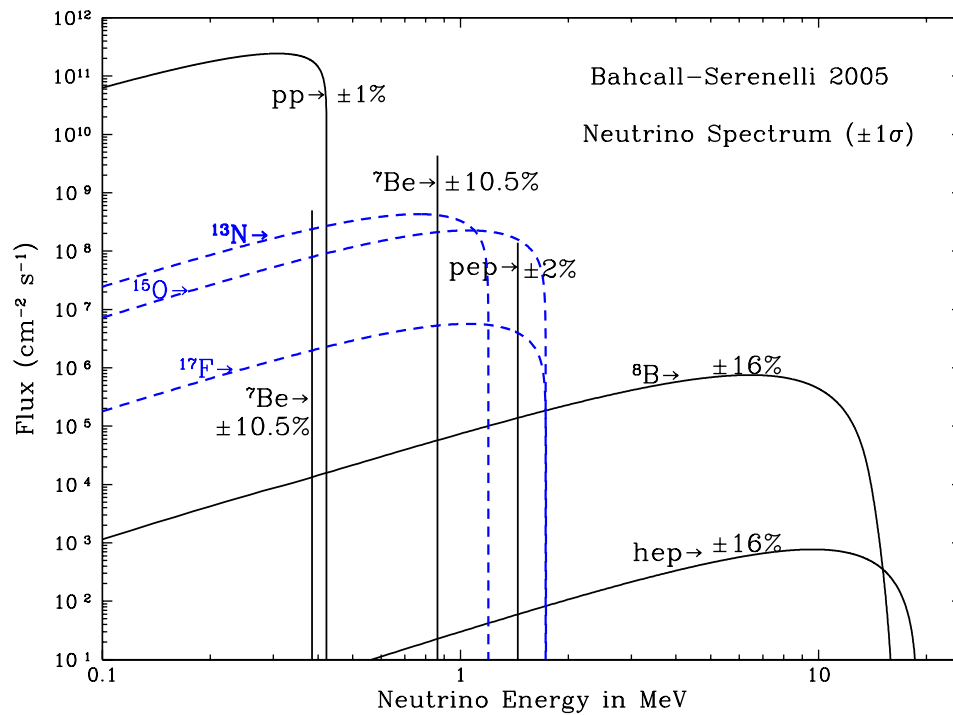


Figure 3.1: The energy spectrum predicted by the Standard Solar Model taken from [25]. The detection thresholds in Table 3.1 show that the water Čerenkov detectors are only sensitive to the higher energy ^8B and *hep* solar neutrino flux. The ^{37}Cl detectors have some sensitivity to the ^7Be , *pep*, *CNO* neutrinos. So far only the ^{71}Ga detectors manage to detect any of the low-energy *pp* neutrinos which account for more than 90% of the total flux.

3.1.1 Homestake

The Homestake experiment [36] detected solar ν_e with energy greater than 813 *keV* using the beta decay reaction,



The detector consisted of 615 tons tetrachloroethylene (C_2Cl_4)¹ contained in a large steel tank. Every few months, the detector was purged with helium to extract ${}^{37}\text{Ar}$ atoms. The argon was concentrated and inserted into a 0.5 *cm*³ gas proportional counter. The number of ${}^{37}\text{Ar}$ decays was fit to the known half-life of 35.04 *days*. The entire detector was located at a depth of 1500 *m* (4200 meters of water equivalent, or *m.w.e.*) in the Homestake Gold Mine at Lead, South Dakota to avoid ${}^{37}\text{Ar}$ produced by cosmic ray neutrons.

From 1970 to 1994, 108 extractions of ${}^{37}\text{Ar}$ were performed; 875 decays were detected. Accounting for extraction and detection efficiencies, this corresponds to an estimated 2200 ${}^{37}\text{Ar}$ atoms produced during the exposure. Above the ${}^{37}\text{Cl}$ threshold, a solar neutrino rate of 2.56 ± 0.16 (stat.) ± 0.16 (syst.) *SNU* was inferred. One *SNU* (solar neutrino unit) is defined as one interaction for 10^{36} target atoms. Neglecting neutrino oscillation, the expected rate from the solar model (BP04) is $8.5_{1.5}^{1.8}$ *SNU*. Only 30% of the expected flux was observed in the Homestake experiment.

¹ 2.2×10^{30} ${}^{37}\text{Cl}$ atoms

3.1.2 SAGE

The Russian-American Gallium Experiment [4, 5] (originally called the Soviet-American Gallium Experiment, or SAGE) detected solar ν_e with the reaction,



The 236 keV neutrino energy threshold allowed SAGE to investigate the low-energy pp neutrinos.

The target consists of 50 tons of liquid metal gallium stored in 7 chemical reactors. The experiment is located at the Baksan Neutrino Observatory in the Northern Caucasus mountains with 4700 m.w.e. overburden. After a typical 4 week exposure, the germanium is extracted in the form of germane (GeH_4). This gas is placed in a proportional counter and counted for approximately 4 to 6 months. The ${}^{71}\text{Ge}$ is identified by electron capture events which return it to ${}^{71}\text{Ga}$, with a half life of 11.43 days .

In 92 runs taken from Jan. 1990 to Dec. 2001, 406 ${}^{71}\text{Ge}$ decays were detected in the proportional counters. Accounting for detector efficiencies, this corresponds to $70.8_{-5.2}^{+5.3}$ (stat.) $_{-3.2}^{+3.7}$ (syst.) SNU . The expected rate according to the solar model (BP04) is $131_{-10}^{+12} SNU$ in the absence of neutrino oscillation. Only 54% of the flux was seen.

3.1.3 Gallex and GNO

Similar to the SAGE experiment, the GALLium EXperiment (Gallex) and its successor the Gallium Neutrino Observatory (GNO) [14, 15] used neutrino interactions with ${}^{71}\text{Ga}$ to measure the solar ν_e flux. The target was 100 tons of gallium chloride, instead of metallic gallium, providing 30.3 tons of gallium. The experiment was located at the

Laboratori Nazionali del Gran Sasso (LNGS) in Italy.

After a standard exposure of 4 weeks, the germanium was extracted, converted to GeH_4 gas, and inserted into proportional counters. Combining the GALLEX and GNO solar neutrino analyses, this process was repeated 123 times in the period from May 14, 1991 to Apr. 9, 2003. The measured solar ν_e flux above 233 keV was measured to be $69.3 \pm 4.1(\text{stat.}) \pm 3.6(\text{syst.}) \text{ SNU}$, in agreement with the result from the SAGE experiment. This is only 53% of the expected rate.

3.1.4 Kamiokande

The Kamioka Neutron Decay Experiment (Kamiokande) [57, 49] was a water Čerenkov detector designed to search for proton decay; it was also capable of measuring solar neutrinos by elastic scattering on electrons. The recoiling electrons emit Čerenkov radiation in the water, which was detected with photomultiplier tubes. Unlike the radiochemical experiments, this method allowed for a real time measurement of the energy-dependent neutrino flux and the neutrino direction. All neutrino flavors interact via elastic scattering, although the cross section for ν_μ and ν_τ is approximately 1/6 of that for ν_e . Due to radioactive backgrounds at lower energies, the detector was only sensitive to the electron recoils above 7 MeV . This corresponds to only a small fraction of the total solar neutrino flux, particularly the upper end of the ^8B neutrino energy spectrum.

The Kamiokande detector consisted of 2140 tons of water, with the inner 680 tons as the fiducial volume. The detector was located 1000 m underground (2700 $m.w.e.$) in the Kamioka mine in the Gifu prefecture in Japan².

²The Kamiokande detector cavity is now occupied by the KamLAND detector.

The total solar neutrino data comprises 2079 *days* taken between Jan. 1987 and Feb. 1995. During this time, the detector energy threshold was lowered from the original 9.3 *MeV* (449 *days*) to 7.5 *MeV* (794 *days*) and finally 7.0 *MeV* (836 *days*). After accounting for background events, a total of 597_{-40}^{+41} solar neutrino events were detected. This results in a measured solar neutrino flux of 2.80 ± 0.1 (stat) ± 0.33 (syst) $\times 10^6 \text{ cm}^{-2} \text{ s}^{-1}$. With no oscillation, the expected ^8B flux according to the solar model (BP04) is $5.79 \times 10^6 \text{ cm}^{-2} \text{ s}^{-1}$, with a 23% theoretical uncertainty. Only 48% of the expected flux was measured.

Aside from solar neutrinos, Kamiokande had the distinction of making an additional contribution to neutrino physics. Both the Kamiokande and Irvine, Michigan, Brookhaven (IMB) experiments detected neutrinos emitted by the supernova 1987a [55, 29]. This was the first and is currently the only detection of supernova neutrinos, and resulted in the 2002 Nobel prize for Masatoshi Koshiba who led the Kamiokande collaboration.

3.1.5 Super-Kamiokande

The Super-Kamiokande detector [51, 47, 48, 80, 58] was constructed with a goal of making a high-statistics solar neutrino measurement. The volume of Super-K is 50,000 tons of ultra-pure water, of which a 22,500 ton fiducial volume is used for the solar neutrino analysis. The detector is located in the same mine as the Kamiokande experiment, under the same overburden of 2700 *m.w.e.*

By carefully controlling radioactive contamination and by ignoring events near the detector boundary, a lower threshold of 5 *MeV* for recoil electrons was achieved. In 1496 *days* of running from Apr. 1996 to Jul. 2001, a total of $22,404 \pm 226$ (stat.) $_{-717}^{+784}$ (syst.) were detected in a 5.0 *MeV* to 20 *MeV* window. This corresponds to a solar ^8B neutrino

flux measurement of 2.35 ± 0.02 (stat.) ± 0.08 (sys.) $\times 10^6 \text{ cm}^{-2} \text{ s}^{-1}$. This is 41% of the solar model prediction with no neutrino oscillation.

The Super-Kamiokande experiment currently continues to take data.

3.1.6 Sudbury Neutrino Observatory

The Sudbury Neutrino Observatory (SNO) experiment [9, 10, 11, 12, 8] is a water Čerenkov detector, similar to Kamiokande and Super-Kamiokande, but the detector is filled with heavy water (D_2O). SNO detects three neutrino interactions,

$$\begin{aligned}
 \nu_e + d &\rightarrow p + p + e^- - 1.442\text{MeV} & (\text{CC}) \\
 \nu_x + d &\rightarrow p + n + \nu_x - 2.224\text{MeV} & (\text{NC}) \\
 \nu_x + e^- &\rightarrow \nu_x + e^- & (\text{ES})
 \end{aligned} \tag{3.5}$$

The charged-current interaction (CC) is sensitive only to electron neutrinos; detection is by the Čerenkov radiation of the emitted electron. The neutral current interaction (NC) has *equal* sensitivity to all neutrino flavors; detection is by the gamma rays emitted when the liberated neutron is captured by a nucleus. With some sensitivity of the elastic scattering (ES) interaction to non-electron flavors, this reaction adds an over-constrained measurement of the electron and non-electron neutrino fluxes.

The SNO detector is located in the Creighton mine near Sudbury, Ontario, Canada, at a depth of 2000 *m* (6000 *m.w.e.*). The neutrino target is 1000 *tons* of D_2O (99.92% isotopically pure) contained within a 6.0 *m* radius transparent acrylic sphere. The experiment was performed in three phases. In the first, the NC events were detected by the 6.25 *MeV* gamma ray emitted by neutron capture on deuterium. In the second phase, NaCl was added to the target volume to increase the sensitivity to and discrimination of NC events. In the

third and final phase, ^3He proportional tubes were inserted to further improve the detection of NC events independent of the photodetection method. Data taking has been completed for all three phases, and the analyses of the Phase I and II results have been completed.

For the first phase of SNO, 306 live days of data taking were between Nov. 1999 and May 2001. Due to an increasing rate of backgrounds at larger distances from the detector center, the analysis was limited to events with reconstructed positions within 5.5 m of the detector center. A threshold corresponding to an electron kinetic energy of 5 MeV was required to avoid low energy radioactive backgrounds. After all cuts, 2928 candidate events remained. Using a likelihood analysis of the event distributions, the estimates of $1967.7^{+61.9}_{-60.9}$ CC events, $263.6^{+26.4}_{-25.6}$ ES events, and $576.5^{+49.5}_{-48.9}$ NC events were obtained (statistical errors only). For this analysis, it was necessary to constrain the fit using the undistorted solar ^8B neutrino spectrum. The resulting solar neutrino fluxes (in units of $10^6\text{ cm}^{-2}\text{ s}^{-1}$) were,

$$\phi_{CC}^{con} = 1.76^{+0.06}_{-0.05}(\text{stat.})^{+0.09}_{-0.09}(\text{syst.}), \quad (3.6)$$

$$\phi_{ES}^{con} = 2.39^{+0.24}_{-0.23}(\text{stat.})^{+0.12}_{-0.12}(\text{syst.}), \quad (3.7)$$

$$\phi_{NC}^{con} = 5.09^{+0.44}_{-0.43}(\text{stat.})^{+0.46}_{-0.43}(\text{syst.}). \quad (3.8)$$

In the second phase of the experiment, $\sim 2000\text{ kg}$ of NaCl were added to the detector. Neutral current interactions were detected by neutron capture on ^{35}Cl , which emits multiple gamma rays with a total energy of 8.6 MeV . The higher cross-section and total energy tripled the neutron capture detection efficiency. The increased symmetry of energy deposition due to the multiple gamma rays allowed for a statistical separation of the NC from the CC and ES events. Using this separation, the likelihood analysis could be

performed without the constraint of the ${}^8\text{B}$ neutrino spectrum.

In this phase, 391 *live days* of data were collected from Jun. 2001 to Oct. 2003. The energy threshold was increased to an electron kinetic energy of 5.5 *MeV*. A total of 4722 candidates events were detected. The resulting estimates of interaction rates were 2176 ± 78 CC events, 279 ± 26 ES events, and 2010 ± 85 NC events. The resulting solar neutrino fluxes (in units of $10^6 \text{ cm}^{-2} \text{ s}^{-1}$) were,

$$\phi_{CC}^{uncon} = 1.68_{-0.06}^{+0.06}(\text{stat.})_{-0.09}^{+0.08}(\text{syst.}), \quad (3.9)$$

$$\phi_{ES}^{uncon} = 2.35_{-0.22}^{+0.22}(\text{stat.})_{-0.15}^{+0.15}(\text{syst.}), \quad (3.10)$$

$$\phi_{NC}^{uncon} = 4.94_{-0.21}^{+0.21}(\text{stat.})_{-0.34}^{+0.38}(\text{syst.}). \quad (3.11)$$

The neutrino fluxes measured by SNO are summarized in Fig. 3.2. The SNO ES rate is consistent with the high-statistics measurement from the Super-Kamiokande experiment. The flux of ν_e measured by the CC interaction rate is inconsistent with the assumption that the neutrino flux is entirely composed of electron neutrinos. The total active neutrino flux measured by the NC interaction rate agrees with that predicted by the other two fluxes, accounting for the decreased sensitivity of the ES interaction to non-electron neutrinos. This measurement of the total active neutrino flux is consistent with the flux of ${}^8\text{B}$ neutrinos predicted by the standard solar model. The results of the SNO experiment were seen as both evidence for neutrino flavor transformation and confirmation of the Standard Solar Model.

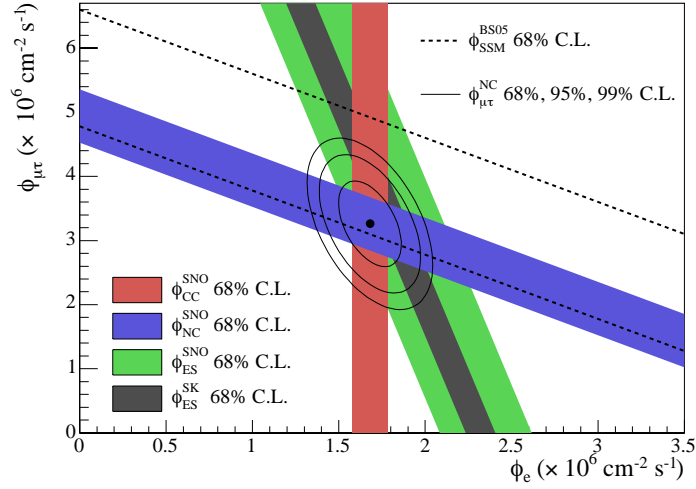


Figure 3.2: The SNO (second phase) flux measurement. The CC, NC, and ES over-constrain the electron and non-electron neutrino flux estimates. The three reaction rates provide evidence for neutrino flavor transformation and confirm the Standard Solar Model. Consistency with the higher-statistics measurement of the ES rate from the Super-Kamiokande is shown. Figure taken from Ref. [8].

3.1.7 Summary of Solar Neutrino Measurements

Fig. 3.3 summarizes the current solar neutrino measurements, showing the solar neutrino fluxes compared with the predictions of the Standard Solar Model (BP04) without oscillation. The points indicate the flux measurement with statistical and systematic errors combined. The horizontal axis loosely characterizes the energy threshold; actual thresholds are listed. The scale is identical to Fig. 3.1 for easy comparison. The colored bars represent the uncertainties in the prediction (BP04). The gallium, chlorine, and SNO CC measurements, only sensitive to ν_e , all show a deficit relative to the expectation. The SNO NC measurements, sensitive to all flavors, and are consistent with the model prediction. The ES measurements measure the ν_e flux and have a reduced sensitivity ($\sim 1/6$) for $\nu_{\mu,\tau}$. The discrepancy between the ν_e flux measurements over different energy regions hints at matter

enhanced oscillation (see Fig. 2.2). The flux suppression for the low energy pp neutrinos is less than the other CC measurements, which could be seen as a transition from matter enhanced to vacuum oscillation.

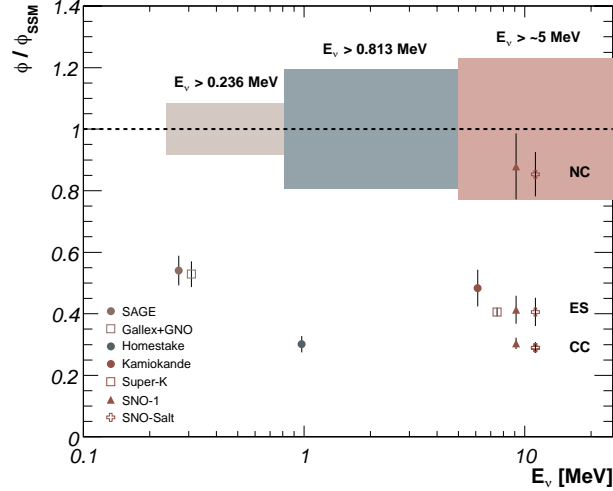


Figure 3.3: The solar neutrino fluxes compared with the no oscillation predictions of the Standard Solar Model (BP04). The points show the flux measurement with total experimental errors. The horizontal position loosely indicates the energy threshold; the actual thresholds are shown. The colored bars represent the uncertainties in the prediction.

3.2 Reactor Neutrino Experiments

Until the turn of the last century, the solar neutrino problem continued to cast doubt on the physical model of the Sun. A series of experiments were performed using neutrinos produced in nuclear reactors to see if there was a consistent deficit, and to look for direct evidence of neutrino oscillation. While the Sun produces ν_e , nuclear reactors are a source of the anti-matter partner $\bar{\nu}_e$. The CPT symmetry of the Standard Model predicts the same oscillation phenomena. Assuming CPT, solar and reactor experimental results

can be combined. Before discussing the individual experiments, it is useful to discuss the commonly-used technique for detecting $\bar{\nu}_e$: the delayed-coincidence method.

3.2.1 The Delayed-Coincidence Method

The Sun and nuclear reactors both produce $\approx MeV$ neutrinos. Experiments must cope with radioactive and cosmic ray induced backgrounds which may mimic the rare neutrino interactions in the energy range of interest. Nuclear reactor produced antineutrinos have a distinct detection advantage over solar neutrinos. An antineutrino interacts with a proton to produce a positron and a neutron,

$$\bar{\nu}_e + p \rightarrow e^+ + n. \quad (3.12)$$

The *inverse beta decay* process has a neutrino energy threshold of $1.8 MeV$. Both the positron and neutron can be independently detected, producing a pair of signals. The characteristic *pair* of signals is a powerful tool for rejecting backgrounds, dramatically improving sensitivity to the lower rate of neutrino events.

One common detector design is a large volume of scintillator, where the scintillator functions as both the target and detector. The $\bar{\nu}_e$ interacts with a proton in the scintillator according to the reaction in Eq. 3.12. Kinematically, the positron carries away the neutrino kinetic energy minus the interaction threshold energy ($1.8 MeV$). Within nanoseconds, the positron will slow in the scintillator and annihilate with an electron. This process is detected as the *prompt* antineutrino event.

The free neutron is not stable, and in isolation it would decay with a mean time of $886 s$. In the presence of matter it is more likely captured by an atomic nucleus, releasing

gamma radiation,



The gamma rays can be detected by interaction in the active target or a separate detector. The mean capture time for a neutron varies greatly depending on the nuclear composition of the detector, anywhere from a few microseconds to hundreds of microseconds. Since this process occurs after the positron is detected, it is called the *delayed* antineutrino event. The detection of the prompt and delayed events together represent a single $\bar{\nu}_e$ detection. Using this signal pair, also called the *delayed-coincidence* signature, the first direct measurement of the neutrino was made by an experiment at the Hanford reactor in eastern Washington.

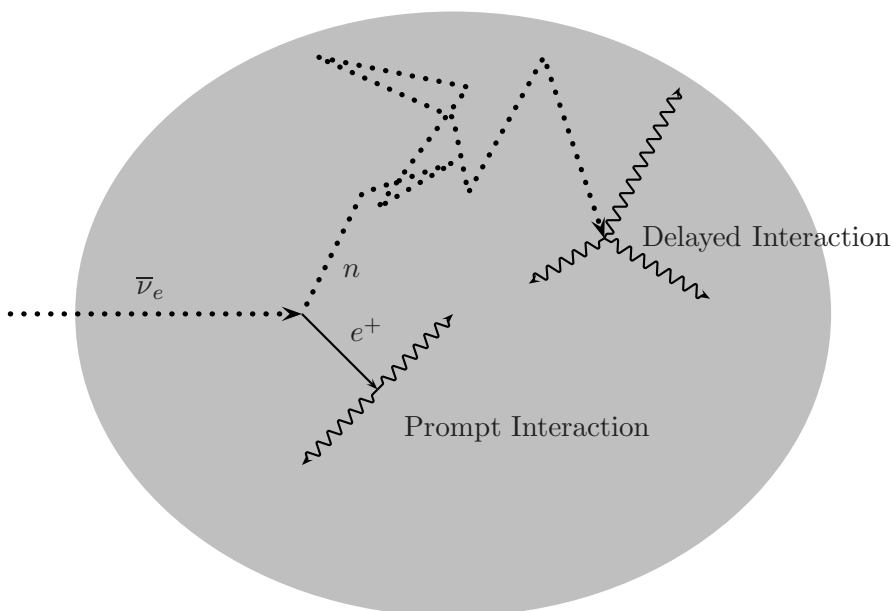


Figure 3.4: The delayed-coincidence signal of inverse beta decay. A neutrino interacts with a proton, producing a neutron and a positron. The positron and annihilation gamma rays are visible by their ionization of the detector (prompt interaction). After the neutron thermalizes, it is captured by a nucleus which releases deexcitation gamma rays (delayed interaction).

3.2.2 Hanford

More than 20 years after Pauli postulated the existence of the neutrino, Reines and Cowan made the first experimental measurement of the antineutrino in 1953 [76]. A 300 *l* tank of scintillator loaded with cadmium and instrumented with 90 photomultiplier tubes was placed next to the core of the Hanford nuclear reactor (Fig. 3.5). Cadmium has a high neutron capture cross-section, resulting in a capture time of 5 μ s. With the reactor not running, the experiment measured a coincidence event pair rate of 2.14 ± 0.13 delayed counts per minute. With the reactor running, this rate increased to $2.55 \pm 0.15 \text{ min}^{-1}$, a change of $0.41 \pm 0.20 \text{ min}^{-1}$. Although the change was consistent with the expected rate of antineutrino interactions, the high rate of background events prevented this measurement from being definitive evidence for the existence of the neutrino.

3.2.3 Savannah River

Using the experience of the Hanford Experiment, Reines and Cowan performed another experiment at the Savannah River nuclear facility [38, 77]. Two 3" \times 4' \times 6' vessels of water were sandwiched between three 2' \times 4' \times 6' vessels of liquid scintillator. The water was loaded with cadmium and served as the antineutrino target. The gamma rays produced by positron annihilation and subsequent neutron capture in the water targets were detected in the scintillator volumes. An antineutrino interaction is accepted when the multiple gamma rays from both the positron and neutron deposit energy in both of the neighboring scintillator volumes. This multiple-layer requirement increased the signal-to-background ratio to 3 to 1, which was significantly better than the Hanford experiment. Photographs



Figure 3.5: The Hanford antineutrino detector, also known as Herr Auge (Mr. Eye). The detector consisted of a 300 l cylindrical tank of liquid scintillator instrumented with 90 photomultiplier tubes. The bases of the photomultiplier tubes can be seen behind the acrylic display case.

of example oscilloscope traces from the experiment are shown in Fig. 3.6. In 1956 the Savannah River experiment reported convincing evidence of the neutrino. For his work in detecting the neutrino, Reines received the 1995 Nobel prize in physics. Unfortunately, Cowan did not survive to share the prize.

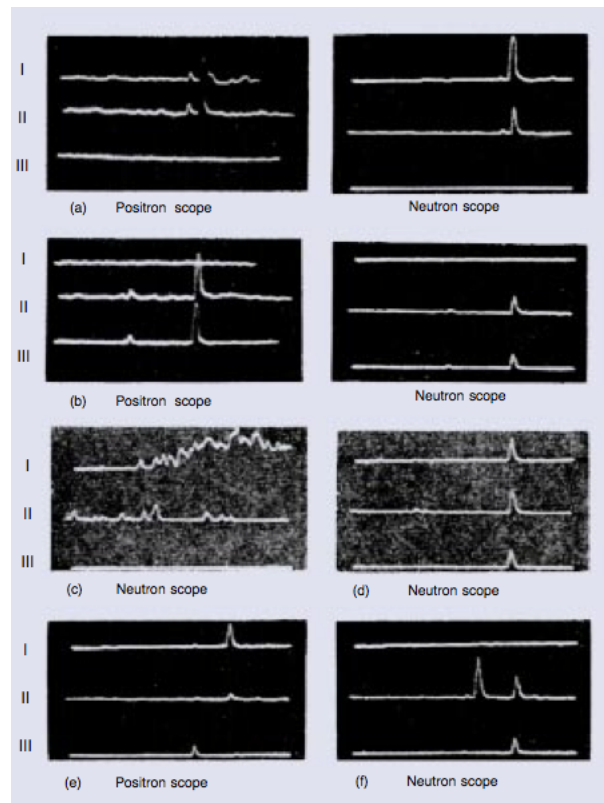


Figure 3.6: The Savannah River experiment used the spatial topology of the data within a segmented detector to identify antineutrinos. Two water target volumes were sandwiched between three scintillator detectors (I,II,III). The photomultiplier tube signals from the scintillators are shown in the figure. Panels (a) and (b) show antineutrino interactions in the upper and lower water targets respectively. Both the prompt positron annihilation and the delayed neutron capture generate a signal in the two neighboring scintillators. The times between the prompt and delayed signals are consistent with the expected neutron capture time. The remaining panels show rejected signals: electronic noise (c), cosmic rays (d,e), and a likely cosmic ray (f). Figure from Ref. [77].

3.2.4 Institut Laue-Langevin (ILL)

Given the solar neutrino deficit, the ILL (Institut Laue-Langevin) reactor neutrino experiment set out to test whether there was a related deficit of reactor neutrinos [66]. A “57 MW”-thermal-power reactor at ILL in Grenoble, France was used as the $\bar{\nu}_e$ source. The detector consisted of a sandwich of 5 planes of liquid scintillator contained in acrylic and four ^3He wire counter planes for neutron detection. The total scintillator target volume of 377 l corresponded to 2.39×10^{28} target protons. The detector was placed 8.76 m from the reactor core, with an expected $\bar{\nu}_e$ flux of $9.8 \times 10^{11} \text{ cm}^{-2} \text{ s}^{-1}$ at the detector. A total of 4890 ± 180 antineutrino events were detected at a rate of 1.58 h^{-1} . A ratio of detected to expected events was measured which was consistent with the predicted flux,

$$R = \frac{n}{n_{exp}} = 0.955 \pm 0.035(\text{stat.}) \pm 0.110(\text{syst.}). \quad (3.14)$$

Subsequent to this experiment, an approximately 10% error in the power level of the ILL reactor was discovered. The result has not yet been corrected.

3.2.5 Gösgen

Following the completion of the ILL experiment, the detector was upgraded and moved to the Gösgen nuclear power reactor in Switzerland [87]. With a significantly bigger thermal power of 2800 MW, the total antineutrino flux was approximately $5 \times 10^{20} \bar{\nu}_e \text{ s}^{-1}$. The detector was placed at three distances from the reactor core, 37.9, 45.9, and 64.7 m, and approximately $10^4 \bar{\nu}_e$ events were measured at each location between 1981 and 1985. The number of antineutrino events at each location divided by the expected number assuming

no oscillation were,

$$R_{37.9} = 1.018 \pm 0.019(\text{stat.}) \pm 0.015(\text{uncor.syst.}) \pm 0.060(\text{cor.syst.}), \quad (3.15)$$

$$R_{45.9} = 1.045 \pm 0.019(\text{stat.}) \pm 0.015(\text{uncor.syst.}) \pm 0.060(\text{cor.syst.}), \quad (3.16)$$

$$R_{64.7} = 0.975 \pm 0.036(\text{stat.}) \pm 0.030(\text{uncor.syst.}) \pm 0.060(\text{cor.syst.}). \quad (3.17)$$

3.2.6 Rovno

The $\bar{\nu}_e$ flux was measured at the Rovno nuclear plant in Russia in 1987 [6]. The detector, composed of 238 l of gadolinium loaded scintillator, was initially placed at 18 m from the reactor core. It was later moved to 25 m. Approximately 32,000 $\bar{\nu}_e$ interactions were detected, split evenly between each detector location. The results from the two distances were reported as a single measurement. The measured rate was consistent with the rate expected assuming no neutrino oscillation, with a ratio of,

$$R = 0.964 \pm 0.068. \quad (3.18)$$

In 1992 an additional experiment was performed at the Rovno facility [62]. Two separate detectors were positioned at 12 m and 18 m from the reactor core. By simultaneously measuring the $\bar{\nu}_e$ signal at two locations, uncertainties associated with the reactor antineutrino source were reduced. Roughly 1000 $\bar{\nu}_e$ interactions were detected at each location. The relative interaction rates at the two locations are consistent with no neutrino oscillation from 12 m to 18 m,

$$\frac{R_{12}}{R_{18}} = 0.976 \pm 0.020(\text{stat.}) \pm 0.015(\text{syst.}). \quad (3.19)$$

3.2.7 Bugey

Comparable to the Gösgen experiment, the Bugey experiment measured the antineutrino flux from a 2800 MW thermal power reactor [40]. Early results from this experiment showed evidence of neutrino oscillation which was inconsistent with other experiments [34]. To further control systematic uncertainties, an improved experiment used three identical detectors; one at 15 m directly beneath the core of the reactor, the other two at 40 m. During a period when the reactor was off, the near detector was used to measure the $\bar{\nu}_e$ flux from a second operating reactor core 95 m away. Each detector consisted of 600 l of liquid scintillator loaded with 0.15% of ^6Li by mass, and divided into 98 segments. The delayed neutron was detected using the reaction,



Approximately ~ 120000 total inverse beta decay events were detected. At each location, the number of detected events was consistent with the expected number of events and no oscillation,

$$R_{15} = 0.988 \pm 0.004(\text{stat.}) \pm 0.05(\text{syst.}), \quad (3.21)$$

$$R_{40} = 0.994 \pm 0.010(\text{stat.}) \pm 0.05(\text{syst.}), \quad (3.22)$$

$$R_{95} = 0.915 \pm 0.132(\text{stat.}) \pm 0.05(\text{syst.}). \quad (3.23)$$

3.2.8 Krasnoyarsk

In 1999, an experiment at the Krasnoyarsk nuclear facility in Russia reported results of measuring reactor antineutrino interactions using heavy water (D_2O) [65]. In the

test phase of their experiment, the detector was filled with 513 *l* of normal water (H₂O). The measurement using the water target may be compared with other inverse beta decay experiments. The delayed neutron was detected using 169 ³He proportional counters arrayed through the detector. At 34 *m* from the reactor, the expected flux was approximately $10^{12} \bar{\nu}_e \text{ cm}^{-2} \text{ s}^{-1}$. The ratio of the detected to expected rate was consistent with no neutrino oscillation,

$$R = 1.00 \pm 0.04. \quad (3.24)$$

3.2.9 CHOOZ

In an attempt to reach even greater sensitivity to long oscillation lengths, the CHOOZ experiment measured the electron antineutrino flux 1 *km* from two reactor cores [17, 18]. The two reactors, located near the village of Chooz in the Ardennes region of France, had a total thermal power of 8.5 *GW*. Since even without oscillation the $\bar{\nu}_e$ flux decreases with the squared distance from the reactor, the detector target size was increased to compensate. The CHOOZ detector consisted of a monolithic 5 *ton* target of liquid scintillator, loaded with 0.09% of gadolinium. Neutron capture on Gd produces a set of gamma rays with a total energy of $\sim 8 \text{ MeV}$. With a lower $\bar{\nu}_e$ flux and larger target volume than previous experiments, backgrounds were a greater problem. To reduce the contribution of cosmic ray induced backgrounds, the detector was placed underground, providing shielding equivalent to 300 meters of water.

The experiment collected data from April 97 until July 98, detecting a total of 2991 coincidence events (reactor signal plus background). The background was measured during time when the reactor was not running. Once again, the total number of detected

$\bar{\nu}_e$ interactions was consistent with the expected number and no oscillation,

$$R = 1.01 \pm 0.028(\text{stat.}) \pm 0.027(\text{syst.}) \quad (3.25)$$

3.2.10 Palo Verde

From 1998 until 2000, an experiment measured the antineutrino flux at the Palo Verde Nuclear Generating Station in Arizona [30]. The facility consisted of three cores with a total thermal power of 11.63 *GW*. The single detector was placed 750 *m* from one core and 890 *m* from the other two, and beneath a cosmic ray shielding equivalent to 32 meters of water. The detector consisted of 11.34 *tons* of liquid scintillator divided into 66 optically isolated segments. The scintillator was loaded with 0.1% of gadolinium, resulting in a 27 μ *s* mean neutron capture time. The measured inverse beta decay event rate relative to the expected rate was,

$$R = 1.01 \pm 0.024(\text{stat.}) \pm 0.053(\text{syst.}). \quad (3.26)$$

3.2.11 Reactor Experiment Summary

Fig. 3.7 summarizes the $\bar{\nu}_e$ flux measurements based on the distance from the nuclear reactor. All values are normalized by the expected flux assuming no neutrino oscillation. Neutrino oscillation would be revealed as a modulation of the flux versus the distance from the reactor. All the experiments shown, with distances up to 1 *km* from the reactor, measured a flux consistent with no oscillation. The shaded region identifies the distances that are probed by the KamLAND experiment. This region corresponds to the LMA solution of the solar neutrino problem.

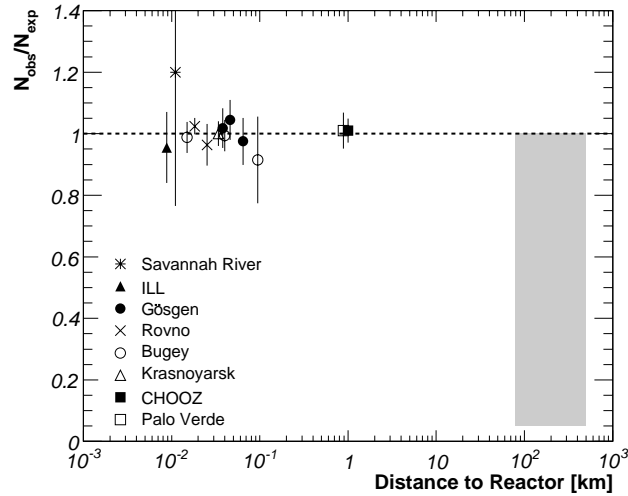


Figure 3.7: $\bar{\nu}_e$ flux measurements based on the distance from the nuclear reactor. All values are normalized by the expected flux assuming no neutrino oscillation. The shaded region identifies the distances that are probed by the KamLAND experiment.

3.2.12 Spectral Distortion

All of the reactor antineutrino experiments described here, except for the Hanford and Savannah River experiments, also measured the positron energy spectrum. As previously noted, the e^+ spectrum is kinematically related to the antineutrino spectrum. For certain ranges of the neutrino oscillation parameters, oscillation will produce an energy dependent distortion of the antineutrino spectrum according to Eq. 2.7. None of the experiments found a significant distortion of the spectrum, thereby constraining the oscillation parameters. With multiple identical detectors, the Bugey and Rovno experiments were able to make simultaneous relative measurements of the antineutrino flux, independent of the uncertainties in the reactor properties and inverse beta decay cross section. These results were also consistent with no neutrino oscillation.

Chapter 4

The Kamioka Liquid Scintillator Anti-Neutrino Detector

The KamLAND experiment was devised to investigate the Large Mixing Angle (LMA) solution of the solar neutrino problem. By using the well-characterized flux of antineutrinos from nuclear reactors, this allows for a measurement of neutrino properties independent of solar models. To reach sensitivity to Δm_{12}^2 in the LMA region ($\Delta m_{12}^2 \sim 10^{-5} eV^2$) with reactor antineutrinos ($E \sim 4 MeV$), the antineutrinos must propagate a distance $L_{osc} \sim 100 km$ (Eq. 2.10). Given that the antineutrino flux from nuclear reactors is isotropic, without oscillation it decreases as the square of the reactor-to-detector distance. To be sensitive to the reduced flux at these large distances, the target volume is increased relative to previous experiments to nearly a kiloton.

4.1 Site Description

Japan produces more than 10% of the world's total nuclear power over a land area less than that of California ($\sim 400,000 \text{ km}^2$). The large number of reactor facilities at distances on the order of 100 km makes Japan an ideal location for a reactor antineutrino experiment probing the LMA region. The antineutrinos from many reactor sites can be combined to increase the total flux.

The KamLAND experiment is situated in a preexisting underground facility near Kamioka city in the Gifu prefecture. The mine is the same that housed the Kamiokande experiment and currently houses the Super-Kamiokande experiment. KamLAND uses the original Kamiokande underground cavity. The experimental site is accessible by horizontal tunnel, simplifying the construction and operation of the detector.

4.2 Detector Overview

The KamLAND detector is a 1 kton low-background monolithic scintillating detector. The light produced by ionization in the scintillator is detected by 1879 large-diameter photomultiplier tubes (PMTs) with approximately 34% coverage. The voltage traces in time from each photomultiplier are digitized, grouped into events¹, and archived. These collections of PMT signals are later processed to determine the position of the interaction in the detector and the energy produced by the interaction (Chap. 6). Offline analysis consists of identifying antineutrino events and discriminating them from backgrounds (Chap. 8).

¹An *event* is the collection of photomultiplier signals associated with a single interaction in the detector.

4.2.1 Physical Detector Design

The KamLAND detector occupies the refurbished underground cavity used for Kamiokande. A cross-section of the detector is shown in Fig. 4.1. The detector volume is 1 kton of liquid scintillator (LS). This is contained within a 13 m diameter transparent balloon supported by kevlar ropes. This balloon is suspended within a 18 m diameter steel sphere with the intermediate space filled with mineral oil. The PMTs are mounted on the steel sphere facing the geometric center of the detector. This internal region is collectively referred to as the Inner Detector (ID). The space between the steel support sphere and the cylindrical rock cavity is the outer water Čerenkov detector (OD) which is used to identify cosmic ray muons as well as to attenuate fast neutrons and gamma rays originating in the rock. The dome area above the detector allows access for calibration and monitoring. The following sections describe these detector components in more detail.

4.2.2 Detection Principle

Particle interactions produce optical photons in the scintillating volume of the detector. These photons travel to and produce signals in the PMTs. Roughly 200 PMTs are hit for 1 MeV of energy deposited in the LS.

4.2.3 The Scintillator

The KamLAND scintillator is a mixture of dodecane (80.2%), pseudocumene (19.8%), and PPO (1.52 g l^{-1}). These are all organic compounds with the following chemical compositions: dodecane ($\text{H}_{26}\text{C}_{12}$), pseudocumene (H_{12}C_9), and PPO ($\text{H}_{11}\text{C}_{15}\text{NO}$). The density of this mixture is 0.780 g cm^{-3} at 11.5°C , closely matched (0.04%) to that of the

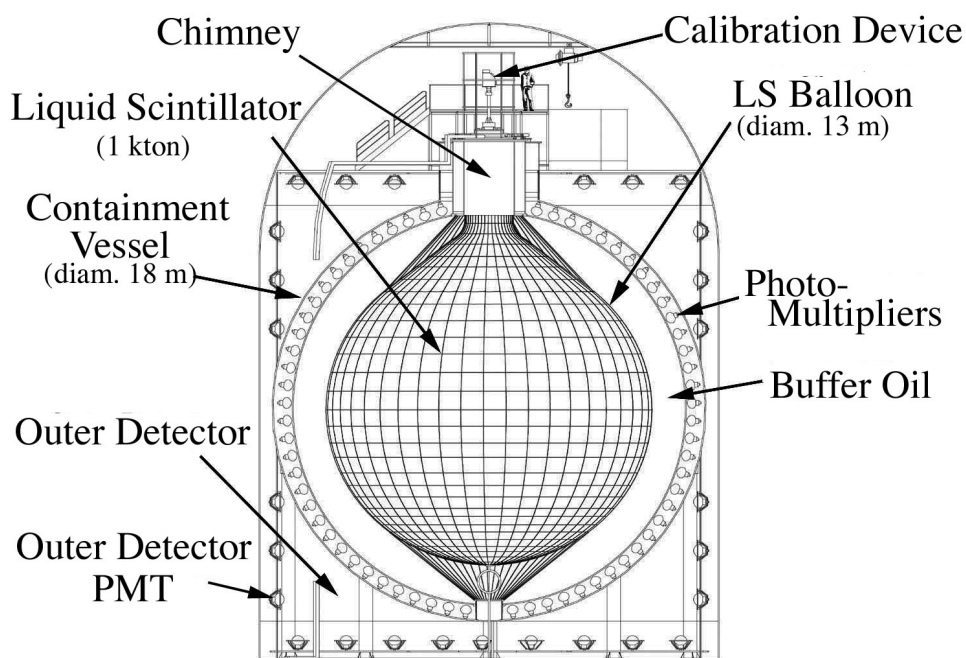


Figure 4.1: Cross section of the KamLAND detector. The detector volume is 1 *kton* of liquid scintillator (LS) contained within a 13 *m* diameter transparent balloon supported by kevlar ropes. An 18 *m* diameter steel sphere contains the balloon, with the intermediate space filled with mineral oil. 1879 large diameter photomultiplier tubes (PMTs) are mounted on the steel sphere and provide 34% coverage. The dome area above the detector allows access for calibration and monitoring.

Table 4.1: Scintillator composition by isotope from a mixture of dodecane (80.2%), pseudocumene (19.8%), and PPO (1.52 g l^{-1}). Natural abundances and the density of 0.780 g cm^{-3} at 11.5° C are assumed.

Isotope	Natural Abundance	LS Abund. [atoms cm^{-3}]
^1H	99.985%	6.6×10^{22}
^2H	0.015%	9.9×10^{18}
^{12}C	98.93%	3.3×10^{22}
^{13}C	1.07%	3.7×10^{20}
^{14}N	99.632%	4.1×10^{18}
^{15}N	0.368%	1.5×10^{16}
^{16}O	99.757%	4.1×10^{18}
^{17}O	0.038%	1.6×10^{15}
^{18}O	0.205%	8.3×10^{15}

mineral oil (dodecane) outside the balloon. Table 4.1 outlines the relative nuclear densities based on natural abundances. Upon ionization, pseudocumene emits scintillation light. PPO is a wavelength-shifting compound; it absorbs the scintillation light and re-emits this light with wavelengths more closely matched to the PMT response.

4.2.4 The Balloon

The scintillator is contained within a $135 \mu\text{m}$ thick, transparent balloon. The balloon material has three layers: EVOH-nylon-EVOH. The nylon provides structural strength. EVOH is an organic material designed to reduce diffusion²; in this case it is used to reduce the diffusion of radon into the scintillating volume. EVOH is also chemically compatible with the scintillator.

The scintillator is maintained at a slightly higher pressure than the mineral oil buffer by adjusting the relative liquid levels. This prevents the balloon from collapsing;

²EVOH was developed for high-altitude helium-filled balloons.

care is taken to keep the stress on the balloon to a minimum.

4.2.5 The Buffer Region

A *buffer region* lies between the balloon and the steel support sphere. Filled with mineral oil (dodecane), it shields radioactivity from the PMTs and provides additional attenuation of gamma rays and neutrons originating from outside the detector. Black acrylic sheets optically separate the region of the PMT mounts from the detection volume and reduce reflection. These acrylic sheets encircle the PMTs exposing only the front sensitive faces to the sensitive inner detector region. Clear acrylic panels are placed on a 16.7 m-diameter sphere between the PMT faces and the rest of the buffer region. This barrier suppresses radioactive contamination (especially radon) from diffusing toward the sensitive region of the detector.

4.2.6 Photomultipliers

Hamamatsu R7250 20"-diameter photomultiplier tubes make up 1325 of the total number of photon detectors. The R7250 was developed especially for KamLAND in which good timing is essential. To maintain timing the PMT photocathodes were masked down to 17". Focused dynode structures, common for fast timing applications, are employed. The changes dramatically improve the timing and single photoelectron peak amplitude, at the cost of a reduced photocathode area.

554 20"-diameters Kamiokande PMTs, Hamamatsu R3600, were reused to increase the total inner detector photocathode coverage to 34%. 240 of the same PMTs instrument the outer detector.

4.2.7 Magnetic Compensation Coils

The performance of the large PMTs is degraded by external magnetic fields. A set of cables which encircle the inner detector provide a magnetic field that compensates for the Earth's field.

4.2.8 Outer Detector

The KamLAND outer detector (OD) is a water Čerenkov detector which fills the space between the walls of the rock cavity and the inner detector steel support sphere. It serves as a cosmic ray veto and attenuates external fast neutrons and gamma rays. 240 refurbished Kamiokande 20" PMTs collect the light in this region. The OD is lined with white Tyvek sheets to increase the total light collection through reflection. Additional Tyvek sheets optically separate the outer detector into four horizontal regions: Top, Upper, Lower, and Bottom. Circulation of purified water in the OD regulates the detector temperature.

4.2.9 Chimney and Glove Box

During normal operation, the inner detector is sealed to prevent contamination. For periodic calibration the scintillating volume can be accessed through the chimney region. A glove box at the top of the chimney allows for the assembly and deployment of calibration devices. The glove box and the chimney region are connected with a vertical port containing two gate valves with 6" and 16" diameters respectively. The valves are only opened during calibration deployments.

Table 4.2: Calibration sources

Source	Type	Half-life	Energy [MeV]
^{203}Hg	γ	46.594 days	0.279
^{68}Ge	γ	270.95 days	1.022 ^a
^{65}Zn	γ	244.06 days	1.116 ^b
^{60}Co	γ	1925.28 days	2.505 ^c
^{241}Am - ^9Be	γ ,neutron	432.2 years	2.223 ^d

^aPositron annihilation plus 3% contribution from 1.077 MeV γ -ray

^b3% contribution from positron annihilation

^cTwo γ : 1.173 + 1.332 MeV

^dNeutron capture gamma. Also produces proton recoils and ^{12}C excitation γ rays (4.439, 7.654, 9.641 MeV)

4.2.10 Radioactive Calibration Sources

A number of radioactive sources are deployed into the scintillating volume of KamLAND characterizing the detector response. These sources are listed in Table 4.2.

4.2.11 Z-Axis Calibration System

During the first four years of KamLAND operation (Jan. 2002–Dec. 2005) calibration was done using the z-axis calibration system. This system consisted of a radioactive source or LED suspended from a Teflon-coated stainless steel cable. The source was lowered from the glove box through the chimney region into the scintillating detector volume (Fig. 4.2). Using this approach, positions along the detector central vertical axis (z-axis) are accessible.

4.2.12 4π Calibration System

In Dec. 2005 the 4π calibration system was installed. This system was designed to allow for calibration of positions in the detector away from the central axis (Fig. 4.3).

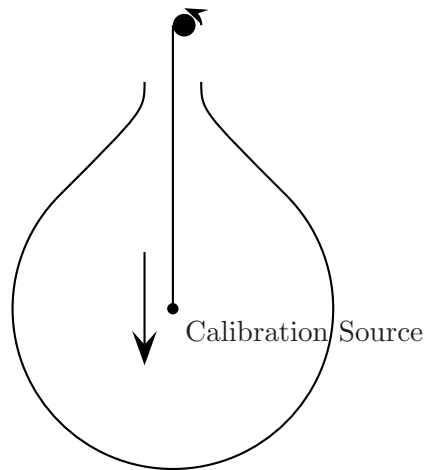


Figure 4.2: Z-axis calibration deployment.

The body of the 4π consists of seven segments of titanium tube, each 0.9 m in length. Up to seven of these segments may be joined and lowered vertically into the detector, with a calibration source attached to the lower end of the pole. Two woven stainless steel and nylon straps control the pole position. One strap is attached to the pole 1.5 m from the calibration source. The other strap is attached to the opposite pole end. Once the pole has been lowered into the scintillating volume, the pole may be moved away from the vertical by adjusting the relative lengths of the straps. The *pivot block* is a small attachment which keeps the straps in a vertical orientation through the chimney region. It is fixed to one strap and allows the second strap to slide relative to the first. Motion of the second strap relative to the first strap determines the inclination of the pole. Calibration sources can be placed at most points in the scintillating volume. The addition of a weighted pole segment shifts the center of mass to reach further off-axis positions. The reconstruction of events

due to a set of ^{60}Co sources embedded in the pole and pivot block allow for a cross-check of the pole position independent of the strap lengths.

4.3 Data Acquisition System

The KamLAND detector produces a number of PMT signals when energy is deposited in the scintillator. A set of coincident PMT signals are identified as an event, and usually correspond to a charged particle moving in the detector. The Data Acquisition System (DAQ) is a combination of electronic systems (hardware and software) responsible for choosing when to group and record the PMT signals. The DAQ collects, orders, and archives the data. It consists of four major components, performing the following tasks:

1. The **front-end electronics** record the signals from the individual photomultiplier tubes as digitized traces of anode current versus time.
2. The **trigger** decides whether or not a collection of PMT signals constitute an event worth recording, and notifies the front-end electronics to digitize the analog traces.
3. The **data read-out system** reads these digital signals out of the front-end electronics and archives them to computer storage. The read-out is done asynchronously, partially shuffling in time the digital traces. Therefore, signals from multiple events are mixed into one unified stream of data.
4. The **event builder** reads in this asynchronous data and groups the digital traces according to individual events (i.e. unshuffling the digital traces), re-archiving the time-ordered data to computer disk.

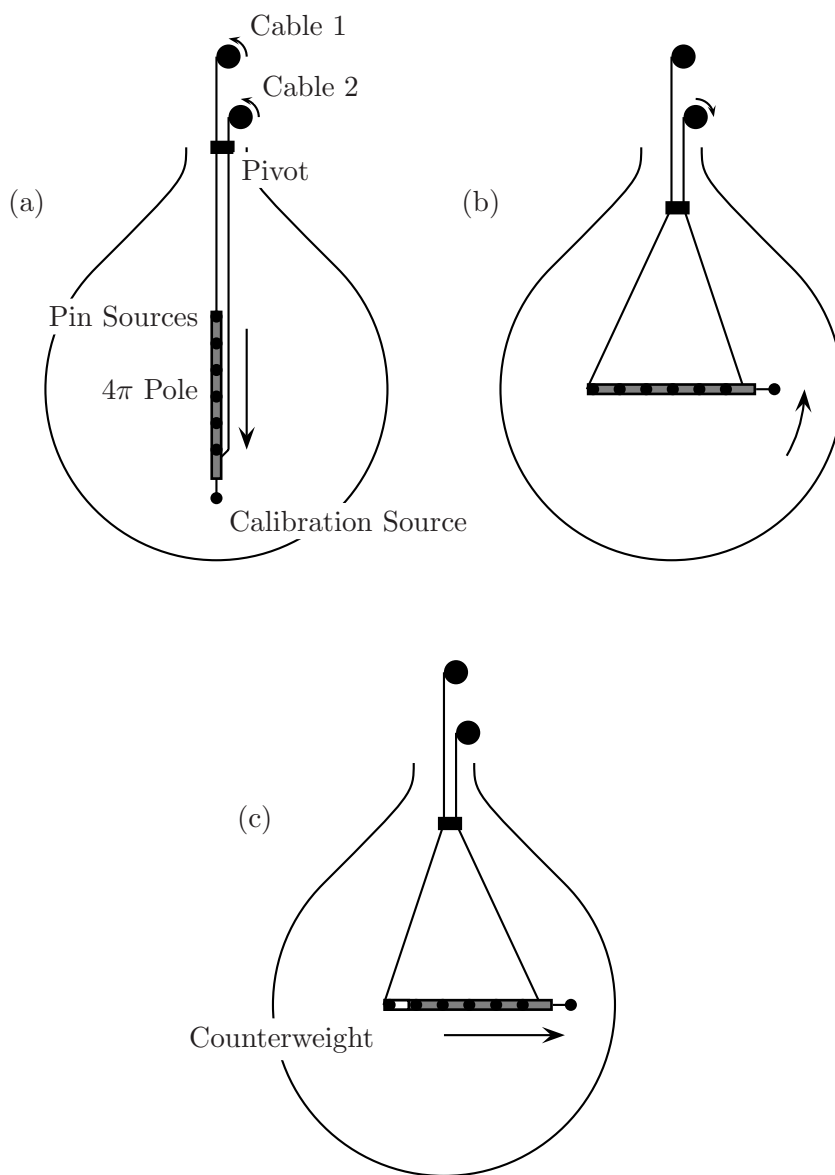


Figure 4.3: 4π calibration deployment. The pole is assembled and deployed vertically (a). Retracting cable 2 draws the pole away from vertical. The pivot block keeps the cables vertical through the detector chimney (b). A counterweighted pole segment increases the horizontal reach of the system to a maximum of 4.6 m (c).

Figure 4.4 presents a simplified picture of KamLAND data acquisition.

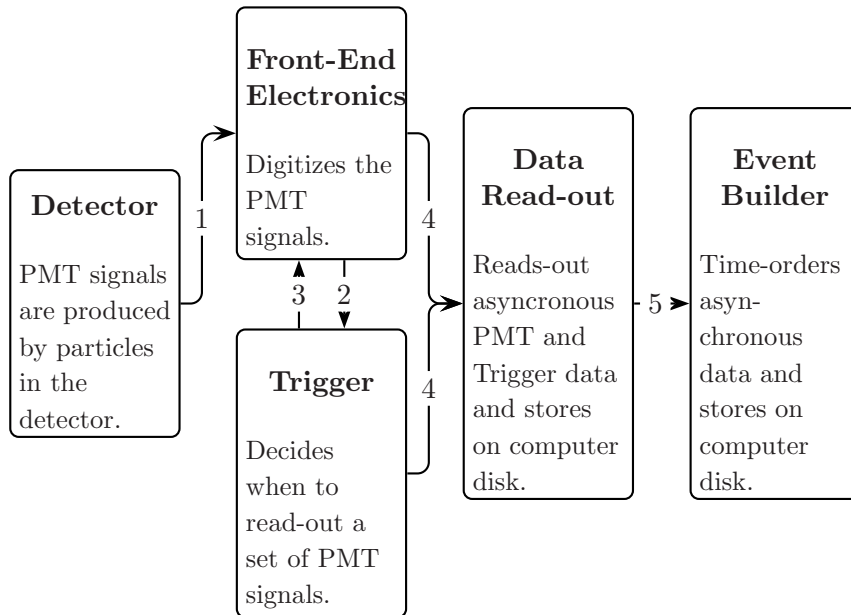


Figure 4.4: KamLAND data acquisition. Analog PMT signals are recorded by the front-end electronics (1). The trigger calculates the number of PMT signals obtained in the past 125 ns (2). Based on the number of hit PMTs, the trigger decides whether to save the data. If triggered (3), the front-end electronics digitize the PMT signals. The digitized PMT and trigger data are read-out and saved to computer disk (4). The data is not time-ordered during read-out. The event builder time-orders the data and re-saves it to computer disk (5).

4.3.1 The Front-End Electronics: Pass 1

The front-end electronics are a set of ~ 200 custom 9U VME electronics boards that handle the detection and analog-to-digital conversion of the PMT signals. An example board is shown in Fig. 4.5. Each board has 12 BNC connectors; a single PMT is attached to each. In the initial analog circuitry, the PMT signal is split: the first signal is sent to a discriminator, while a copy is sent into a delay line. The discriminator threshold is

set to approximately 0.5 mV , which is sufficient to capture single photoelectron signals. If the discriminator identifies a pulse, then the signal traveling down the delay line is recorded by one of the two Analog Transient Waveform Digitizers (ATWDs) attached to the channel. The ATWD functions by attaching the analog input to a series of 128 capacitors for approximately 1.5 ns each, thereby storing the pulse profile. The logic of this process is managed by a Field-Programmable Gate Array (FPGA) attached to the channel. The board runs at 40 MHz ; each clock tick is 25 ns . The number of channels on the board that received a signal in an individual clock tick is summed and sent to the trigger (board *nsum*).

4.3.2 The Trigger

The trigger is a custom board which accepts the individual board *nsum* signals and makes a decision on whether to record the event. At the beginning of a run, the trigger configuration is fixed according to the desired run conditions. From the individual board *nsum* signals, the trigger assembles the total number of 17" PMT channels which received a signal in the past 5 clock-ticks (125 ns). This count is referred to as the *nsum*. During normal data taking, the trigger issues a message to record the event if the *nsum* is greater than 200. After Apr. 2004, this threshold was lowered to 180 to be more efficient for detecting low energy neutrino interactions. This *nsum* level roughly corresponds to an energy threshold of 0.8 MeV (*nsum* 200) or 0.7 MeV (*nsum* 180). For 1 ms after an event is recorded, the trigger threshold is reduced to an *nsum* of 120 (0.4 MeV) to capture lower energy time correlated events. Under normal running conditions, the trigger rate is roughly 30 Hz . The maximum value of the *nsum* during an event, called the *nsummax*, is recorded

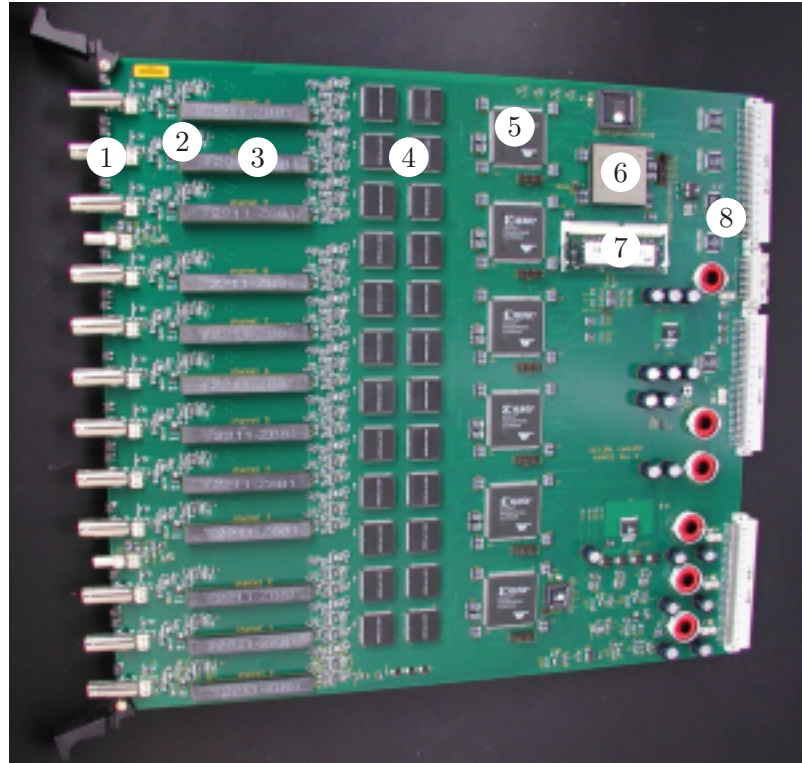


Figure 4.5: A KamLAND front-end electronics VME board. A single PMT is attached to each channel (1); a single board supports 12 PMTs. The analog signal is split. One copy is sent to a discriminator circuit (2); the other is sent to a delay line (3). If the discriminator threshold is crossed, one of the two ATWD chips (4) records a $\sim 200\text{ ns}$ analog trace of the signal from the delay line. If the trigger orders, the signal is digitized and read into a buffer on one of the six channel FPGAs (5). The board FPGA (6) reads the data from the channel FPGAs and buffers it to 32 MB of on-board memory (7). The data is read out of the board through the VME bus (8).

and used as a proxy of the total energy of the event. A detailed discussion of the trigger is found in [82].

4.3.3 The Front-End Electronics: Pass 2

When the front-end electronics receive a message from the trigger to record the event, the signal in the ATWD is digitized and written to a memory buffer on the board.

4.3.4 Data Read-out

The data acquisition system asynchronously reads the signals from memory buffers on each board through the VME bus. The signals are then converted and sent over optical fiber from the VME crate to the data acquisition computer system. Each VME crate has a dedicated read-out computer. Another computer manages the read-out computers, aggregates the signals from each, and records the data to a raid disk. The data format for this asynchronous data is referred to as KDF format.

4.3.5 The Event Builder

The event builder is a computer program which is responsible for reading in the asynchronous data (KDF) and unshuffling it into the format of individual detected events (SF). This program may be run at the time of data collection, or at a later date on data stored in KDF format. The major challenge of this program is to keep up with the large amount of data flowing from the detector.

4.3.6 KiNOKO

KiNOKO is a data acquisition system software package written for use with the KamLAND detector. In KamLAND it is responsible for managing all the components of data acquisition: starting up the various systems, initializing run conditions, and transporting and archiving data.

4.3.7 Data Volume and Lossless Data Compression

In one day under normal running conditions, the KamLAND detector produces roughly 100 GB of data in compressed SF format. Due to the difficulties of transporting, archiving, and analyzing the large volume of data produced in the experiment, compression of the data is very valuable. Standard compression tools performed poorly on the data in SF format, reducing the data by only 20%. Using detailed knowledge of the physical nature of the data and ideas from information theory, a specialized compression algorithm was written under the constraint that no information is lost in the compression (the details are discussed in Appendix A). This lossless compression reduces data in KDF format to $\sim 25\%$ and SF format to $\sim 30\%$ of their original size.

Chapter 5

Determining the Antineutrino Flux from the Reactors

This chapter describes the process of determining the reactor antineutrino flux at the KamLAND site. The unoscillated flux is determined and then the effects of oscillation are considered and compared to the KamLAND measurement.

The estimation of the $\bar{\nu}_e$ flux is summarized as follows. The fission rates of the reactor fuel isotopes are obtained for each of the nuclear power reactor cores in Japan. The antineutrino spectra for each decay chain are used to convert the fission rates into the antineutrino flux and energy spectrum by reactor core. The flux at the KamLAND site is estimated by taking account of the distance and the effect of neutrino oscillation. Finally, the positron energy spectrum is calculated using the inverse beta decay cross section.

The total antineutrino rate for a standard 3GW (thermal) power reactor can be roughly estimated. From the neutron to proton ratio in the nuclei of the spent fuel, relative

to the original fuel abundances, there are about $6\bar{\nu}_e$ emitted per fission. The masses of the spent fuel isotopes determine an energy release of approximately 200 MeV per fission. A 3 GW reactor produces $\sim 6 \times 10^{20}$ antineutrinos per second. A more rigorous calculation of the antineutrino flux at KamLAND now follows.

5.1 Reactor Power and Fission Rates

The thermal power and refueling data for each power reactor core in Japan is provided to the KamLAND collaboration through agreements with all of the Japanese reactor companies. The data is converted into a table of isotope fission rates computed at daily intervals [70]. The reactor cores included in the analysis are listed in Table 5.1. Distances range from 87 km to 830 km from the detector. Japanese reactor types are mostly boiling water reactors (BWR) and pressurized water reactors (PWR). Included are two lower-power test reactors: an advanced thermal reactor (ATR) and a fast breeder reactor (FBR). Reactors outside of Japan are included approximated using a single reactor at one distance for each country. The total flux for each country is computed from the reported electrical power. Reactors outside of Japan contribute roughly 1% of the unoscillated neutrino flux at KamLAND. Figure 5.1 shows the total unoscillated reactor antineutrino flux, in units of the number of inverse beta decays per target proton per day above the $\sim 2.6\text{ MeV}$ analysis threshold. The vertical dashed line shows the end of the data period used in the previous KamLAND results; the current analysis includes the full range and is approximately twice the exposure.

Table 5.1: Japanese reactor sites included in the KamLAND flux determination. The thermal and electrical power ratings indicate the nominal power of each core.

Site	Location	Core	Type	Distance [km]	Thermal [MW]	Electrical [MW]
Hamaoka	Chubu	1	BWR	214	1593	540
		2	BWR	214	2436	840
		3	BWR	214	3293	1100
		4	BWR	214	3293	1137
		5	BWR	215	3926	1380
Shimane	Chugoku	1	BWR	401	1380	460
		2	BWR	401	2436	820
Tokai2	Genden	1	BWR	295	3293	1100
Tsuruga	Genden	1	BWR	138	1064	357
		2	PWR	138	3423	1160
Tomari	Hokkaido	1	PWR	783	1650	579
		2	PWR	783	1650	579
Shika	Hokuriku	1	BWR	88	1593	540
		2	BWR	88	3926	1358
Japan Nuclear Cycle	Fugen	1	ATR	139	557	165
Japan Nuclear Cycle	Monju	1	FBR	142	714	280
Mihama	Kansai	1	PWR	146	1031	340
		2	PWR	146	1456	500
		3	PWR	146	2440	826
Ohi	Kansai	1	PWR	179	3423	1175
		2	PWR	179	3423	1175
		3	PWR	179	3423	1180
		4	PWR	179	3423	1180
Takahama	Kansai	1	PWR	191	2440	826
		2	PWR	191	2440	826
		3	PWR	192	2660	870
		4	PWR	192	2660	870
Genkai	Kyusyu	1	PWR	754	1650	559
		2	PWR	755	1650	559
		3	PWR	755	3423	1180
		4	PWR	755	3423	1180
Sendai	Kyusyu	1	PWR	830	2660	890
		2	PWR	830	2660	890
Ikata	Shikoku	1	PWR	561	1650	566
		2	PWR	561	1650	566
		3	PWR	561	2660	890
Onagawa	Tohoku	1	BWR	430	1593	524
		2	BWR	431	2436	825

		3	BWR	431	2436	825
Fukushima1	Tokyo	1	BWR	349	1380	460
		2	BWR	349	2381	784
		3	BWR	349	2381	784
		4	BWR	349	2381	784
		5	BWR	350	2381	784
		6	BWR	350	3293	1100
Fukushima2	Tokyo	1	BWR	345	3293	1100
		2	BWR	345	3293	1100
		3	BWR	345	3293	1100
		4	BWR	345	3293	1100
Kashiwazaki Kariwa	Tokyo	1	BWR	159	3293	1100
		2	BWR	159	3293	1100
		3	BWR	159	3293	1100
		4	BWR	160	3293	1100
		5	BWR	161	3293	1100
		6	BWR	161	3926	1356
		7	BWR	160	3926	1356
Higashidori	Tohoku	1	BWR	636	3293	1100

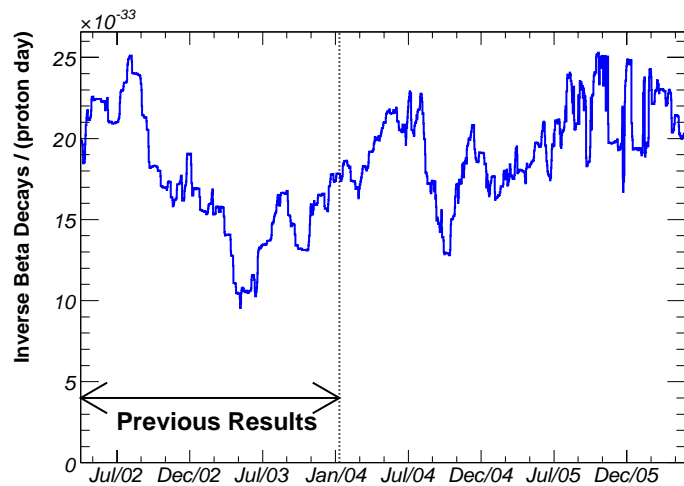


Figure 5.1: The estimated reactor antineutrino flux, in units of the number of inverse beta decays per proton per day above a ~ 2.6 MeV analysis threshold. The flux is calculated assuming no oscillation.

5.2 Antineutrino Flux By Isotope Fission

Figure 5.2 shows the antineutrino energy spectra due to the key isotopes in reactor fuel. The spectra from the fission of ^{235}U , ^{239}Pu , and ^{241}Pu are from fits to the measured beta decay spectra of the fission fragments [78, 54]. The spectrum for ^{238}U is a theoretical estimate [84] based on the known fission fragments and beta decay strength functions. The beta decay of long-lived isotopes is a small contribution. Long-lived isotopes will emit low energy antineutrinos, mostly below the inverse beta decay threshold. ^{106}Ru ($\tau_{1/2} = 373.6 \text{ days}$) and ^{144}Ce ($\tau_{1/2} = 284.9 \text{ days}$) decay to the short-lived daughter nuclei ^{106}Rh ($\tau_{1/2} = 29.8 \text{ s}$) and ^{144}Pr ($\tau = 17.3 \text{ m}$) respectively, and the daughter decays produce antineutrinos above the 1.8 MeV inverse beta decay threshold. Above the interaction threshold, the relative production of $\bar{\nu}_e$ from ^{235}U , ^{238}U , ^{239}Pu , and ^{241}Pu for a standard reactor is 0.61, 0.13, 0.20, and 0.06 respectively [70].

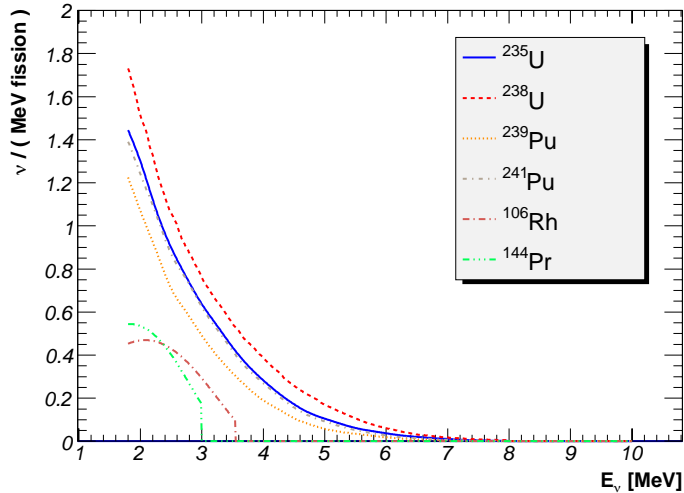


Figure 5.2: The antineutrino energy spectra from the key fissioning isotopes in reactor fuel.

5.3 Inverse Beta Decay Cross Section

Translating the antineutrino flux into the expected positron spectrum in KamLAND requires an estimate of the inverse beta decay cross section. The rate of interactions is given by,

$$R = f\sigma. \quad (5.1)$$

where σ (cm^2) is the cross section and f ($neutrinos\ cm^{-2}\ s^{-1}$) is the antineutrino flux. By crossing symmetry, the cross section for inverse beta decay is related to neutron beta decay. To zeroth order in inverse powers of the nucleon mass, $1/M$, the cross-section is written [83],

$$\sigma^0 = \frac{2\pi^2}{f_{p.s.}^R \tau_n m_e^5} E_e^{(0)} p_e^{(0)}, \quad (5.2)$$

where τ_n is the lifetime of the neutron, m_e is the mass of the electron, and E_e and p_e are the positron energy and momentum respectively. The phase space factor $f_{p.s.}^R$ is calculated to be 1.7152 [83]. For protons at rest in the laboratory, the $\bar{\nu}_e$ threshold is,

$$E_{thr} = \frac{(M_n + m_e)^2 - M_p^2}{2M_p} = 1.806\text{MeV}. \quad (5.3)$$

Including corrections of order $1/M$, the total cross section is calculated numerically and shown in Fig. 5.3.

5.4 Positron Energy

In inverse beta decay, the positron carries away most of the kinetic energy. Positron annihilation adds 1.022MeV of detectable energy. Accounting for masses and annihilation, the visible energy from the positron is $E_p \simeq E_\nu - 0.8\text{MeV}$. The neutron recoils with

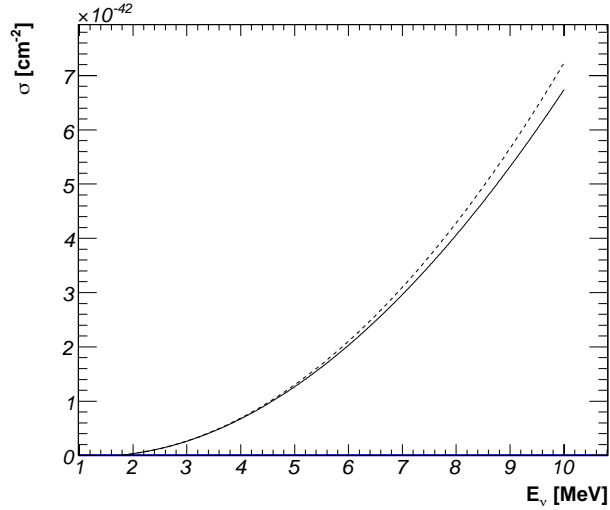


Figure 5.3: The inverse beta decay cross section as a function of antineutrino energy E_ν to zeroth order (dashed) and first order (solid) in $1/M$. The zeroth order cross section is calculated from Eq. 5.2. The first order cross section is from [83].

only tens of keV of energy because of its large relative mass. The exact energy depends on the direction of recoil. A refinement comes from including recoil energy loss from the $\beta\text{-}\bar{\nu}_e$ angular correlation. In the present analysis, the positron is taken to be emitted at the mean angle for a particular energy¹. This assumption is necessary because we do not measure the angle in KamLAND but it has a negligible effect on the analysis. The positron visible energy spectrum, including the annihilation gamma rays and assuming no neutrino oscillation, is displayed in Fig. 5.4.

¹The energy width due to the angular distribution is much smaller than the energy resolution of the detector.

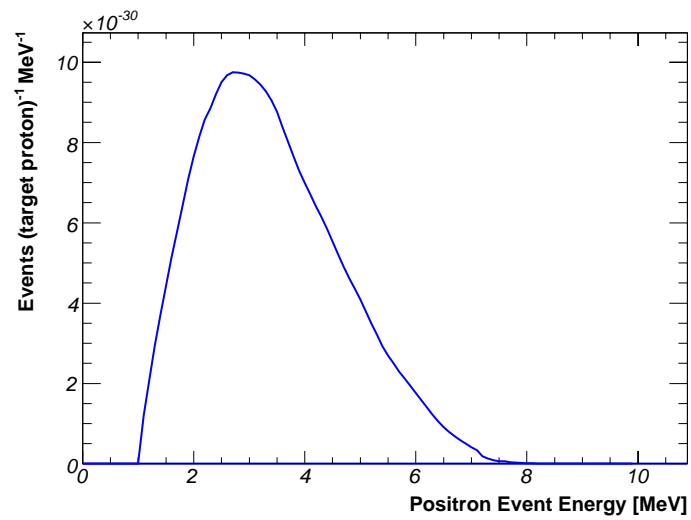


Figure 5.4: The estimated positron energy spectrum assuming no oscillations. The energy is the sum of the positron kinetic energy and 1.022 MeV annihilation gamma rays. The curve is normalized per proton in the target volume.

Chapter 6

Event Reconstruction

Each trigger signal leads to a number of digitized photomultiplier signals that are recorded for offline analysis. All of the signals associated by time with a single interaction is an *event*. The process of using the signals contained in an event to estimate the position and energy of a charged particle interaction is *event reconstruction*.

The first step in this process is to precisely determine the total signal size (the *collected charge*) and time of each PMT signal. Once the times and charges for each PMT signal are determined, the event is classified by the distributions of the times and charges. Finally, refined estimates of the position and energy of the particle interaction which caused the event are determined from the time and charge distributions using a model of scintillation and light propagation developed for the KamLAND detector.

6.1 PMT Signal Processing

The signal from each PMT is a sequence of 128 samples reflecting the anode current as a function of time, as shown in Fig. 6.1. The samples are $\sim 1.5\text{ ns}$ apart, so the entire waveform corresponds to almost 200 ns . The digital value of each sample ranges from 0 to 1023 (10 bits). A PMT signal appears as peaked distributions in the waveform; the position of the peak reflects the time t of the signal and the area represents the accumulated charge Q . Times and charges are the basic data used in the analyses. Much effort went into developing the algorithms for determining times and charges. Figure 6.3 displays the method of PMT signal processing.

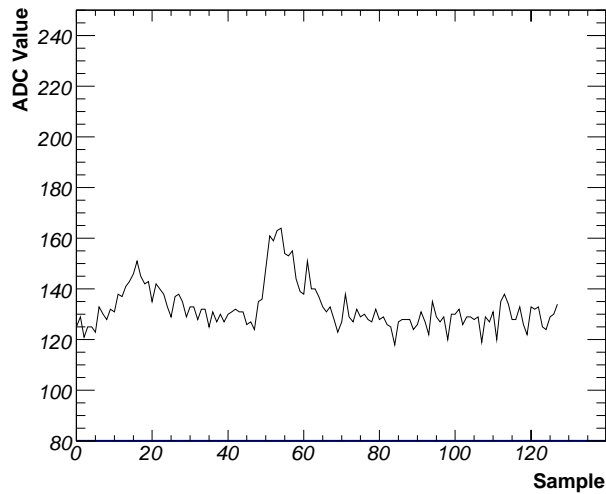


Figure 6.1: An example of a raw digitized waveform representing a current trace of a PMT signal versus time. The two peaks are from single photoelectron level signals. The 128 samples correspond to a 192 ns window.

6.1.1 *Gain Filtering*

KamLAND was designed to have a large dynamic range; from MeV -level neutrino interactions to the GeV -level cosmic ray muons. The PMTs and bases used in KamLAND were shown to be linear over a dynamic range of $\sim 10^4$. In the electronics, the dynamic range is preserved by using three separate amplifiers for each PMT. The nominal amplifications correspond to $20\times$, $4\times$, and $0.5\times$. The $20\times$ amplification captures signals with amplitudes less than a millivolt, below the signals from single photoelectrons. The $0.5\times$ amplification captures pulses with amplitudes greater than a volt, which are due to the multi-photoelectrons usually from high-energy particle interactions.

Normally, only the waveform from the $20\times$ gain needs to be recorded. Although the digital range of each gain extends from 0 to 1023, the response is non-linear above an ADC value of 900. If the signal is above ADC value 896 in the $20\times$ gain, then the waveform from the $4\times$ gain is also collected. If this signal is above 896 ADC value in the $4\times$ gain, then the $0.5\times$ gain is collected as well. There may be three collected waveforms corresponding to a single PMT signal, as shown in Figure 6.2. For the usual MeV -level events, only the $20\times$ gain is used in the analysis and other gain waveforms are discarded. For GeV -level events, the timing is extracted from the leading edge of the $20\times$ gain waveform, while the charge comes from the lowest gain channel. The procedure of using the $20\times$ gain for timing data provides consistent results over a wide range of signal amplitudes when the high gain channel is saturated.

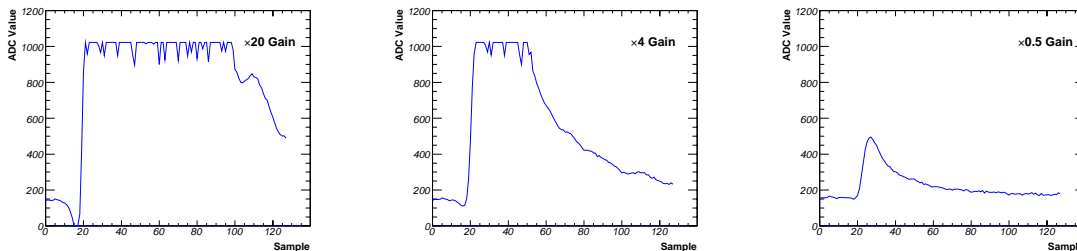


Figure 6.2: A waveform caused by a large PMT signal ($\sim 10^3$ photoelectrons) recorded in all three gains. The front-end electronics can capture signals from single to 10^3 photoelectrons.

6.1.2 Pedestal Subtraction

The first stage in signal processing is the removal of digital offsets in the ATWD. Each of the 128 samples collected by an ATWD has a different offset. At the beginning of each *run*¹, 50 waveforms are collected from each ATWD with a random trigger. The sample-to-sample variations in these *pedestal* waveforms are characteristic of the ATWD and are stable in time. The average of 50 pedestal waveforms is taken as a measure of the offsets. To reject the cases where a real signal arrived while these waveforms were collected, outliers are rejected from the sample. The average pedestal waveform is subtracted from each successive waveform collected from each ATWD.

6.1.3 Waveform Smoothing

After pedestal subtraction, the waveforms often display small ADC value fluctuations from pickup associated with digital processes in the electronics. This and other high-frequency noise can cause error in the analysis of the waveform. A smoothing filter applied to each waveform reduces the impact of high-frequency noise. It is obviously important

¹A *run* is an individual period of data collection, usually one day in length.

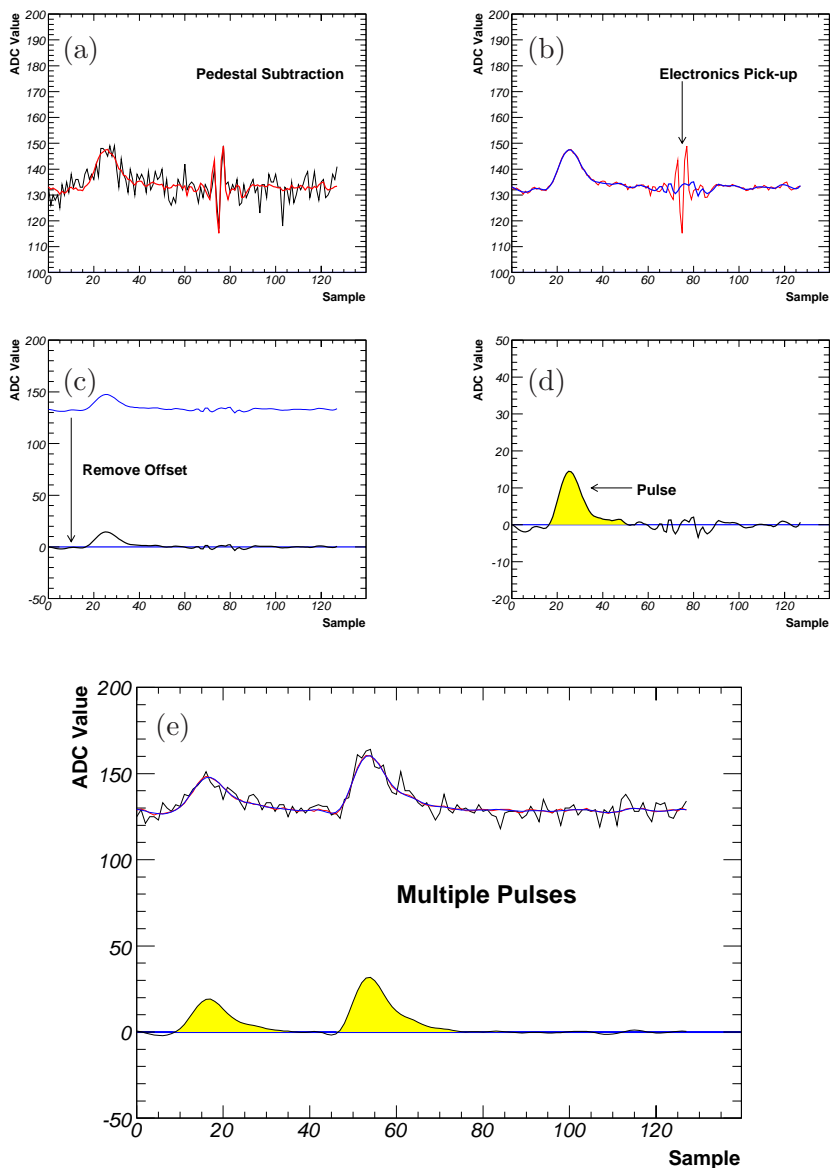


Figure 6.3: Determining PMT single-photoelectron pulse arrival time and charge from digitized signals. (a) Pedestal subtraction removes the fine variations which are an artifact of the ATWD. (b) Savitzky-Golay filtering removes electronics-induced noise. (c) The ADC offset is removed so that an ADC value of zero represents no signal from the PMT. (d) PMT pulses are identified by contiguous regions of positive area. (e) Multiple photoelectrons can be individually identified.

that the smoothing filter does not significantly distort the PMT signal. A Savitzky-Golay filter [73] was found to effectively reduce the noise for simulated pulses. The filter smoothes a function using a polynomial approximation within a limited window. The order of the polynomial and the size of the smoothing window must be chosen. For waveform smoothing, a fourth-order polynomial fit over a window of 15 waveform samples determines the ADC value at the center of the window. For each of the 128 ADC values in a waveform, the window is reset and the polynomial approximation of the smoothed ADC value is determined.

6.1.4 Determining the ADC Offset

It is necessary to determine the ADC offset which corresponds to no PMT signal. The waveform signal is offset so that negative signal fluctuations or low frequency variations do not shift the ADC values below the digital scale (0 to 1023). This offset is not the same for each electronics channel, and because of drifts it must be determined for each waveform.

For waveforms with small signal peaks, the highest-valued ADC samples are iteratively discarded from the waveform until the distribution of ADC values above and below the mean ADC value in a waveform is symmetrized. This preferentially removes the ADC samples corresponding to PMT pulses, which are positive. The mean of the remaining ADC values is interpreted as the ADC value obtained for a signal of zero voltage. This value is subtracted from each sample in the waveform and regions of positive area are interpreted as PMT signals.

For very large PMT pulses, from cosmic ray muons for example, the pulse tail may extend for the full length of the waveform (~ 200 ns). In this case, the best approximation for the ADC offset is the mean of the few samples which precede the arrival of the PMT

pulse. The mean of the first 10 waveform samples is interpreted as the ADC value of no signal.

6.1.5 Pulse Finding

After pedestal subtraction, the next step is to determine the time and charge of each pulse. A different method is used for small and large pulses.

Single photoelectron level signals are selected by finding regions of positive ADC values. Fig. 6.4 shows the pulse area spectra for 17" and 20" PMTs. To reject noise in the waveform from being misidentified as PMT pulses, any pulse with less than 15% of the total positive area of the waveform is discarded. The arrival time of the pulse is determined from a second-order polynomial fit to the waveform peak.

For large pulses, the waveform is treated as containing only a single pulse. A constant threshold (50 ADC counts) was found to provide the optimal pulse time. The charge is determined by summing up the area of the waveform.

6.2 Event Classification

After the time and charge of each of the PMT signals has been determined, the event is classified using a combination of the PMT and trigger data. The following section discusses this categorization procedure.

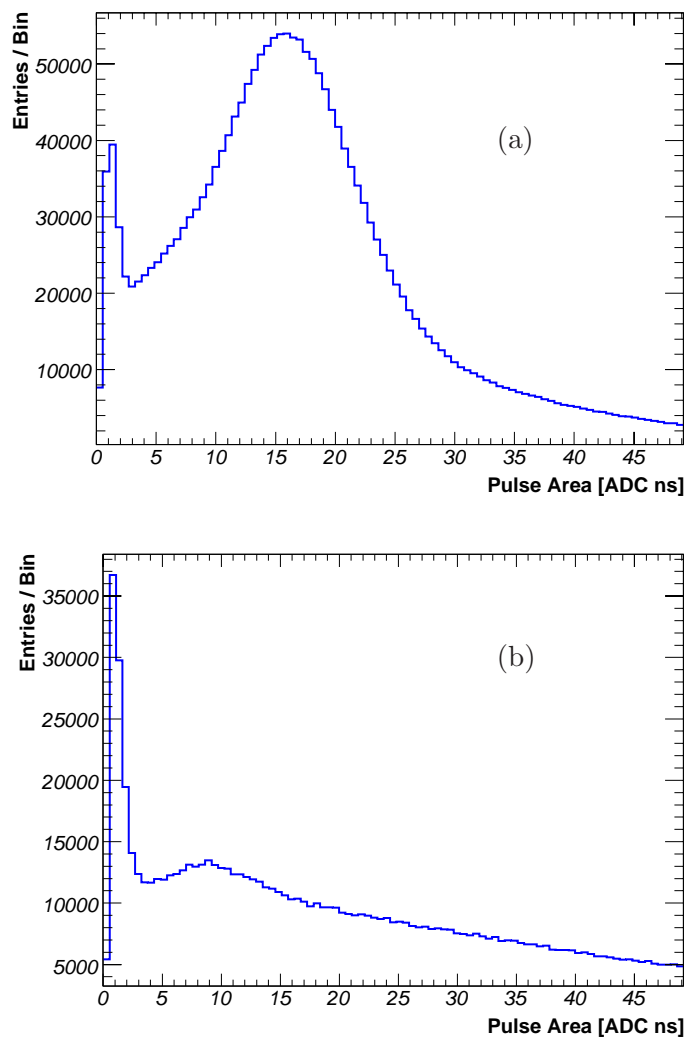


Figure 6.4: The pulse area spectra for single photoelectron signals in the 17" PMTs (a). The smaller peak is from noise. The sensitivity to single photoelectron signals for 17" PMTs is significantly improved relative to the 20" PMTs (b). The spectra were obtained by looking at the pulse areas obtained during data taking; the majority of signals are due to single photoelectrons.

6.2.1 Low-level Event Classification

Reconstructed quantities such as energy and position might be used in event classification, but the classification would then depend on the reconstruction algorithm and reconstruction efficiencies. In particular, for inner detector muon events the identification efficiency should be as high as possible to reliably eliminate muon induced radioactivity. The event time according to the trigger and the inner and outer detector *nsummax* are independent of reconstruction and used for event categorization. The categories are also identified using low-level measures of time and charge. Two specific quantities are defined for this purpose: N_t , which corresponds to the total light collected in the event, and σ_n , which is the dispersion of this light across the PMTs.

The total number of photoelectrons is defined in terms of the analog sum of the PMT outputs,

$$N_t = \sum_{17''} g_i Q_i, \quad (6.1)$$

$$= \sum_{17''} N_i \quad (6.2)$$

which is the sum of the charge Q_i collected by the 17'' PMTs in the inner detector, each with a gain correction factor g_i related to the charge deposited by a single photoelectron. Note that N_t is not necessarily an integer. The PMT-to-PMT variation of N_i is σ_n ,

$$\sigma_n = \sum_{17''} \sqrt{\frac{(N_i - \langle N \rangle)^2}{N_t}}. \quad (6.3)$$

This is the RMS of the PMT-by-PMT photoelectron distribution in a single event, normalized to the total number of photoelectrons. (This form is motivated by the familiar $\sigma_n/\sqrt{n} \approx 1$ from Poisson statistics.)

Fig 6.5 shows how these two low-level quantities separate different categories of events. All events for a sample period of roughly one day of livetime are included in this figure except for those occurring within $50 \mu s$ after a LS muon.

Identification of muons in the outer detector is more difficult. Figure 6.6 displays the correlation of the number of PMT signals in the outer detector relative to the light in the inner detector for the same data period above. A significant fraction of events from muons passing through the outer detector do not produce enough light to be discriminated from the noise.

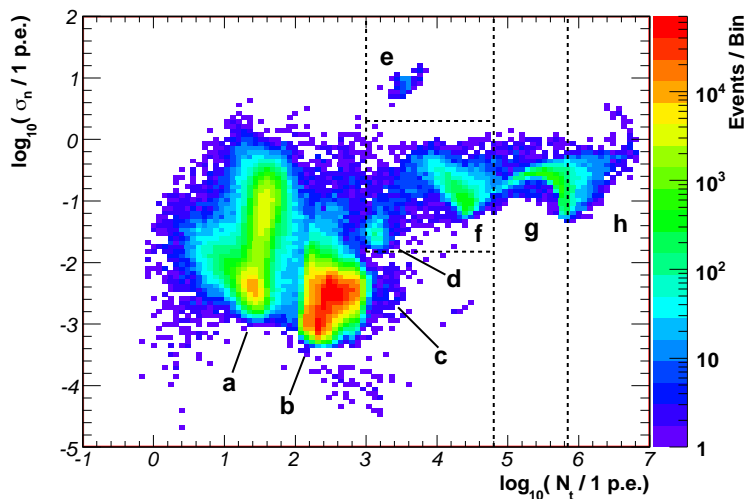


Figure 6.5: Distribution of events in the inner detector for a subset of the data (run 5155). (Events occurring within $50 \mu s$ following a LS muon are not included.) The two quantities N_t and σ_n discriminate between classes of events: (a) background light in the inner detector, (b) low-energy candidate events, (c) higher-energy events, mostly ^{12}B decays, (d) residual post-muon noise, (e) PMT flasher events, (f) muons depositing energy in the buffer oil, (g) muons depositing energy in the liquid scintillator, (h) showering muons. The dotted lines are the cuts used to select the e, f, g, and h categories of events. The cuts were chosen after examining and classifying the reconstructed events.

Finally, the OD-ID correlated noise can be identified by examining the OD and

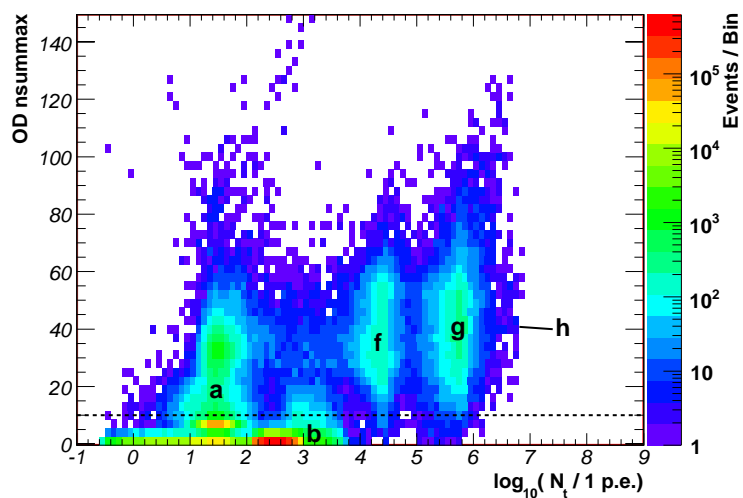


Figure 6.6: The signal from the outer detector relative to the inner detector for an example run (5155). Events with OD $nsummax \geq 10$ (dotted line) are identified as muons in the outer detector. The OD signal does not clearly separate muon events and noise. The regions f and g are due to muon events in the inner detector. The tails of each of these regions extend below the OD threshold, showing an inefficiency of the outer detector. The letters identify the same event regions as Fig. 6.5.

ID n_{summax} distribution for events (Fig. 6.7). The noise produces the anomalous bands of events with a roughly linearly related OD and ID n_{summax} values. These events occur intermittently, and are evident in a few segments of data. The noise has been found to be correlated to electrical interference coming from outside the detector. The noise is evidently from insufficient electrical isolation.

6.2.2 Event Types

Reactor antineutrino events produce signals in the range of 0.1 to 10 MeV . Interactions and radioactive backgrounds in this energy range are therefore the most important. Aside from these low energy interactions, a wide range of other signal events are collected by the KamLAND detector. Events are categorized based on timing, trigger data, and detector light distributions. The reconstructed energy and position are not used for event classification since these are reconstruction algorithm dependent. The categories are denoted by the most common events found in each. The event categories are:

Candidates (area b): Low energy (0.1 to 10 MeV) particle interactions. These events are candidates for the prompt or delayed component of an inverse-beta decay.

Outer Detector (OD) Muons: Cosmic ray muon events in which the muon produced a signal in the outer veto detector ($OD\ n_{summax} \geq 10$). This classification is independent of the inner detector.

Inner Detector (ID) Muons (areas f,g,h): Cosmic ray muon events in which the muon appears to have deposited a significant amount of energy in the inner detector.

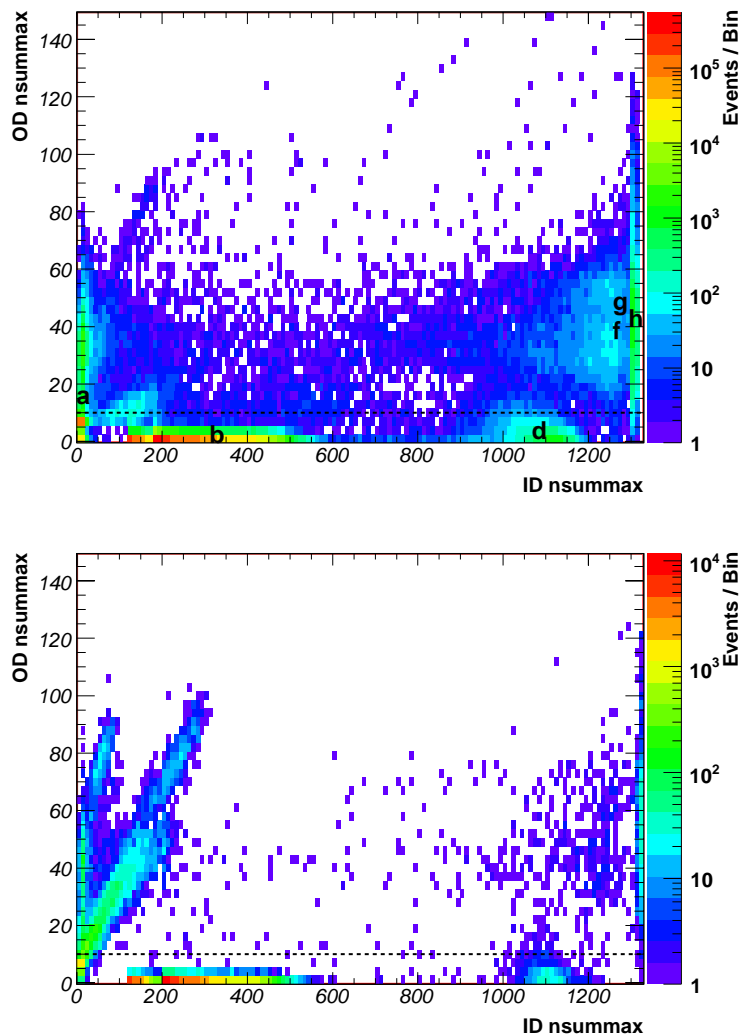


Figure 6.7: The two panels both show the inner and outer detector $nsummax$ signals. The upper panel shows a typical period of data (run 5155), while the lower shows a short period (run 2019) with a high rate of OD-ID correlated events due to electronic noise. Events occurring above the dotted line are classified as muon events by the outer detector. The letters identify the same event regions as Fig. 6.5.

Liquid Scintillator (LS) Muons (areas g,h): Cosmic ray muons which deposit a significant amount of energy in the scintillating volume of the inner detector. (This category is a totally-contained subset of all Inner Detector muons.)

Mineral Oil Muons (area f): Cosmic ray muons which deposit a significant amount of energy in the mineral oil buffer volume of the inner detector. (Effectively, the ID muon events which are not also LS muon events.)

Muon Showers (area h): Showers expected to be generated by muons in which a significant amount of energy goes into the ID, beyond the energy of a minimum-ionizing muon. (This category is a totally-contained subset of all Liquid Scintillator muons.)

Post-Muon Noise: Detector noise generated events due to afterpulsing in the PMTs occurring in the first $50 \mu s$ after LS muon events.

Short-Lived Spallation: Short-lived cosmic ray muon-induced radioactivity of the detector occurring in the $50 \mu s$ to $2 ms$ period after the ID muon event (e.g. spallation neutrons captures).

Medium-Lived Spallation: Cosmic ray muon-induced radioactivity with decay times occurring in the $2 ms$ to $200 ms$ period after an ID muon event (e.g. ^{12}B , ^{12}N decay).

Long-Lived Spallation: Long-lived cosmic ray muon-induced radioactivity of the detector whose decays occur in the $200 ms$ to $2 s$ period after an ID muon event (e.g. 9Li , 8He).

OD-ID Noise: Detector noise generated events which display a correlation between the

signals seen in the Inner and Outer detectors. (Also named Nikolai Noise for Nikolai Tolich who was the first to interpret these events.)

PMT Flasher (area e): Events associated with a very large signals collected in a single PMT. PMT “flashing” events are caused by light emitted from particular PMTs.

6.3 Vertex Reconstruction

The vertex fitting algorithm uses PMT hit times to estimate the event location. Starting with an initial estimate based on the charge-weighted mean position, the vertex position is moved in three dimensions to sample the deviation of the PMT hit times relative to the expected hit times. The expected hit times are estimated using direct light paths from the vertex to the hit PMTs, using two speeds of light for the scintillator (196.1 mm ns^{-1}) and mineral oil buffer region (220 mm ns^{-1}). The speeds of light were determined using calibration data. To avoid the effects of scattered or reflected light or accidental PMT signals, only those pulses in a window between -10 ns to $+5 \text{ ns}$ around the direct light peak are included.

The mean time of the prompt light $\langle t \rangle$ is calculated using the mean of the PMT hit time distribution, and then refined iteratively by rejecting pulses with deviations greater than 10 ns from the mean. This process is repeated until the shift in the mean for the step is less than 0.1 ns , or 100 iterations have been made. During this stage, the estimated vertex is fixed.

Next, the vertex position is moved at each step according to the differences in predicted and actual PMT hit times for pulses in the prompt light peak. The shift is given

by,

$$\vec{x} = \frac{1}{N_{peak}} \sum_i \vec{R}_i \left(1 - \frac{t_i - \langle t \rangle}{\Delta t_i} \right), \quad (6.4)$$

at each step of the process. N_{peak} is the number of pulses in the $-10 ns$ to $+5 ns$ window around the peak time. The sum is taken over the PMTs pulses within the time window. \vec{R}_i is the vector from the current vertex position to the hit PMT. $t_i - \langle t \rangle$ is the deviation of the hit time relative to the peak time of prompt light. Δt_i is the expected time for light to travel directly from the vertex to the hit PMT. The fitting algorithm is based on the signal timing of direct light. The factor in parentheses enhances the role of the direct light and nearby tubes since these signals should have the highest correlation with the event position. Distant tubes are enhanced by \vec{R}_i .

This process of shifting the vertex is repeated until the resulting shift in position is less than $1 mm$, or until 100 shifts have been done. If the vertex failed to converge in the 100 steps, or if the vertex reconstructs at an unphysical position outside the detector, another attempt is made to converge using another 100 iterations.

Based on the fit results, the final vertex is marked according to the criteria listed in Table 6.1. All reconstructed vertices marked with anything other than the Valid flag are not used in the analysis. The reconstruction efficiency decreases to account for these events.

6.3.1 Position Calibration

The data from KamLAND is accompanied by calibrations that characterize the detector. This is often accomplished by examining the data produced by well-understood interactions in the detector. There are three categories of calibration events: radioactive

Table 6.1: Vertex Reconstruction Status

Status	Description
Valid	Fit was successful
Unknown	Less than 4 pulses in event
Not Valid	Fit reconstructed unphysically ($r > 10 m$)
Bad Fit	Fit did not converge
Bad RMS	Residual timing distribution has an unphysical RMS ^a
Bad Pulse Ratio	Unphysical fraction of pulses in the peak ^b
Bad Peak RMS	Peak of residual timing distribution has an unphysical RMS ^c

^a < 35 ns or > 90 ns

^b < 22% or > 55%

^c < 1.7 ns or > 4 ns

sources inserted into the detector, naturally occurring radioactive contamination, and muon activation. The energy and position reconstruction of such interactions is a measure of detector performance, providing a test of the detector model that underlies the reconstruction algorithms.

Most calibrations are accomplished with sources deployed along the vertical axis (z-axis) of the detector (Sec. 4.2.11). A charge-dependent correction to PMT timing was parameterized using all of the gamma ray lines from calibration sources. The speeds of light in the liquid scintillator and mineral oil were adjusted to improve the position reconstruction along the z-axis. The calibration source positions, shown in Fig. 6.8, fit well to a single Gaussian peak and a flat background, except for the ²⁴¹Am-⁹Be source. (Penetrating neutrons and higher-energy gamma rays give non-Gaussian tails to the distribution.) The deviation of the reconstructed position of calibration sources placed along the z-axis is shown in Fig. 6.9. The reconstructed position is within a few centimeters of the known position, except for the low energy ²⁰³Hg source which shows a strong shift toward the center of the detector. The reconstruction performance in the horizontal plane is found to have a

similar behavior.

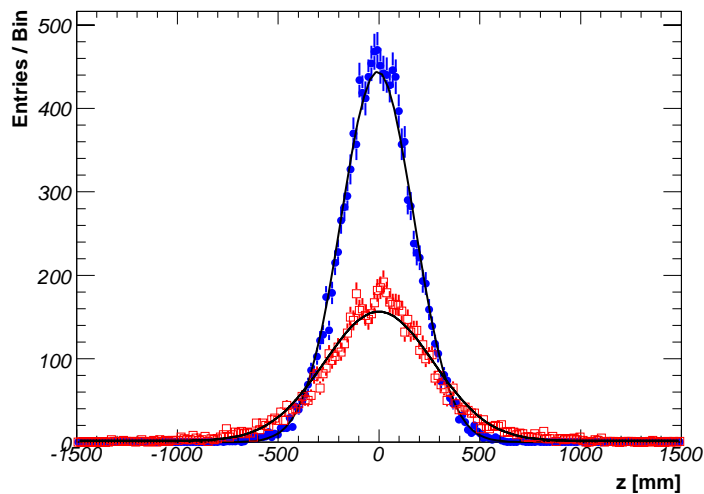


Figure 6.8: The reconstructed z -position for ^{60}Co gamma rays (blue circles) and ^{241}Am - ^9Be 2.2 MeV neutron capture gamma rays (red squares). The sources were placed at the detector center.

The spread in the reconstructed calibration source positions varies between sources, as evident in Fig. 6.10. The low energy ^{203}Hg events have lower photon statistics and a higher relative contribution of uncorrelated PMT signals (also called *dark noise*). The detector position resolution shows little variation with the vertical positioning of the source within the detector. The position resolution in the horizontal plane (for sources along the z -axis) is similar.

6.4 Energy Reconstruction

The energy reconstruction algorithm estimates the visible energy of an event in the KamLAND scintillator. The true particle energy should be related to the visible energy

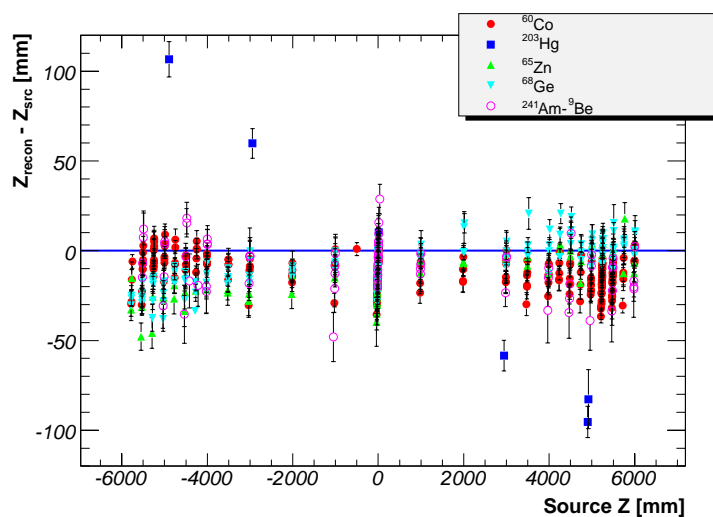


Figure 6.9: The deviation of the reconstructed position of calibration sources placed along the vertical axis (z -axis) of the detector. The low energy events from ^{203}Hg show a significant deviation.

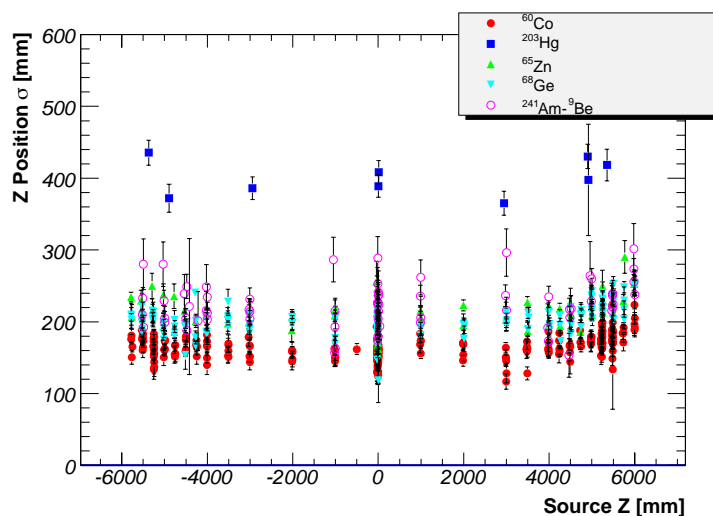


Figure 6.10: The mean squared deviation of reconstructed calibration source positions along the vertical axis (z -axis) of the detector. The low energy ^{203}Hg events have lower photon statistics and a wider distribution. The resolution shows little variation with source position.

via a quenching correction which depends on the charge to mass ratio and a correction for Čerenkov radiation. When working with mixed-species data where the species is not known a priori, it is convenient to analyze events in terms of their *visible energy* E_v . The visible energy unit is defined so that the 2.5 MeV sum of the two gamma rays from ^{60}Co has the same value in real and reconstructed energy.

6.4.1 Charge Probability Distribution

The key component of the energy reconstruction is a model for the probability P_i for the i -th PMT to produce a signal N_i from the collection of a fraction of the visible energy E_v at vertex position \vec{r}_v . N_i is the PMT gain-corrected charge, in units roughly corresponding to number of photoelectrons. Five effects are included in the model:

1. An exponential attenuation $1/l_a$ of the light from the vertex to the PMT.
2. A background rate α_i of uncorrelated photoelectrons.
3. The solid angle subtended by active photocathode Ω_i .
4. A Poisson probability $P(n_e|\langle n_e \rangle)$ to detect n_e photoelectrons given a mean $\langle n_e \rangle$ photoelectrons.
5. A probability $P_i(N_i|n_e)$ of n_e photoelectrons to generate a signal N_i , including electronics threshold effects.

Combining these components,

$$P_i(N_i|E_v) = \sum_{n_e=0}^{\infty} P_i(N_i|n_e)P(n_e|\langle n_e \rangle_i(E_v)), \quad (6.5)$$

is obtained, where the mean number of photoelectrons depends on the attenuation, solid angle and quantum efficiency,

$$\langle n_e \rangle_i(E_v) = \langle n_e \rangle_0 \Omega_i e^{-\frac{|\vec{r}_v - \vec{r}_i|}{l_a}} E_v + \alpha_i. \quad (6.6)$$

The coefficient $\langle n_e \rangle_0$ is the number of photoelectrons per unit of visible energy for each PMT, determined using calibration data. The dark rate α_i is the number of uncorrelated photoelectrons in PMT i in an average event. The attenuation length l_a is considered uniform across both the scintillator and mineral oil; attempts to include separate attenuation lengths did not improve the reconstructed energy of calibration sources. The model parameters are determined from calibration sources. The probability $P_i(N_i|n_e)$ of n_e photoelectrons to produce a signal N_i is obtained from a fit of a sum of Gaussian functions to the gain-corrected pulse area distribution.

6.4.2 The Energy Likelihood Function

The energy likelihood function is the product of the probabilities for the 17" PMTs in the inner detector,

$$L(\vec{N}|E_v) = \prod_{\text{PMT } i} P_i(N_i|E_v). \quad (6.7)$$

The sum excludes PMTs channels which are dead or busy processing previous events. A list of active PMTs is constructed for each event. The effective χ^2 ($\equiv -2 \log(L)$) is minimized in one dimension using a Newton-Raphson algorithm [73]. The energy reconstruction process returns one of the conditions listed in Table 6.2. For any status other than *Valid*, the event is excluded.

Table 6.2: Energy Reconstruction Status

Status	Description
Valid	Fit was successful
Unknown	Event lacks PMT signal data
Not Valid	Minimization failed

6.4.3 Energy Calibration

Understanding the detector energy response is essential for determining the antineutrino spectrum. The energy of calibration events are obtained with the algorithm in Sec. 6.4. The parameters in the energy reconstruction model are determined from the ^{60}Co source at the detector center. The energy spectrum is fit in the range of interest with a Gaussian distribution on top of a second-order polynomial background, as shown in Fig. 6.11. The reconstructed energy for source deployments at the detector center are shown in Fig. 6.12. An additional 0.13% systematic uncertainty is added, determined from the observed detector energy reconstruction drift in time.

The variation of the energy reconstruction with position along the z-axis is shown in Fig. 6.13, normalized to the center source position. A systematic source position bias is evident. The same bias is in Fig. 6.14, displaying calibrations from the full-volume 4π system as well as from neutron capture events ($n + p \rightarrow d + \gamma$) expected to be uniformly distributed within the detector volume.

6.4.4 Energy Response Model

A simple energy response model accounts for the normal saturation effects observed in scintillation detectors, along with the effects of finite photon statistics. The visible energy

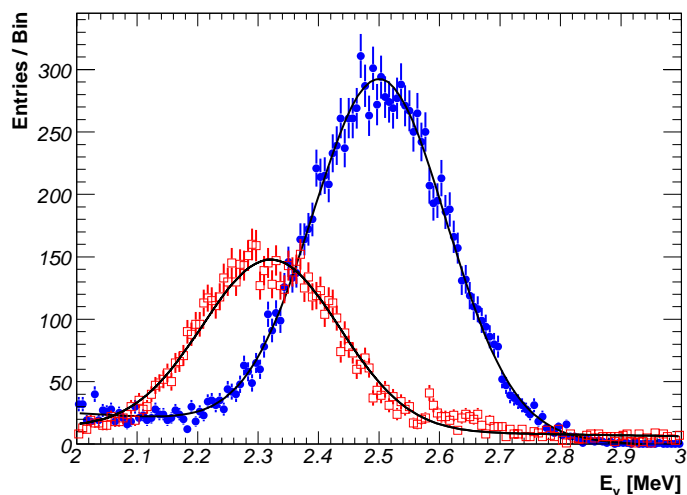


Figure 6.11: The reconstructed energy of ^{60}Co gamma rays (blue circles) and ^{241}Am - ^9Be 2.2 MeV neutron capture gamma rays (red squares). The sources were at the center of the detector.

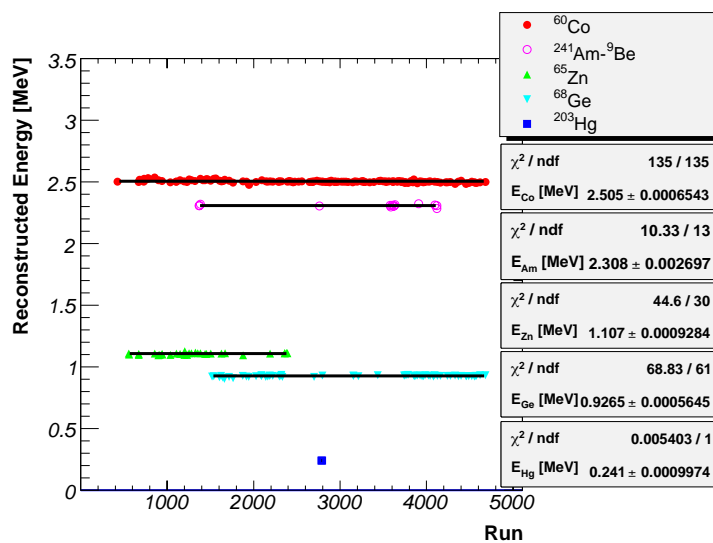


Figure 6.12: The reconstructed energy of all calibration source deployments to the detector center for the current data. An additional 0.13% systematic uncertainty is included to account for observed drifts in the calibration parameters.

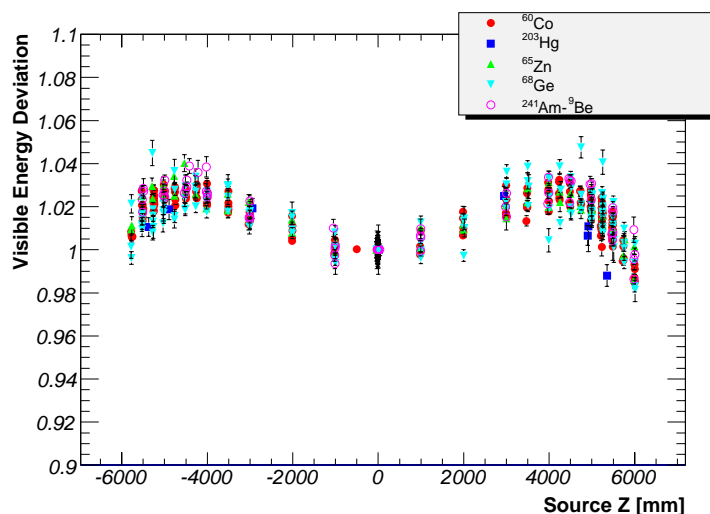


Figure 6.13: The energy for calibration sources along the z-axis, divided by the reconstructed energy at the detector center. A systematic bias with position is evident for all sources.

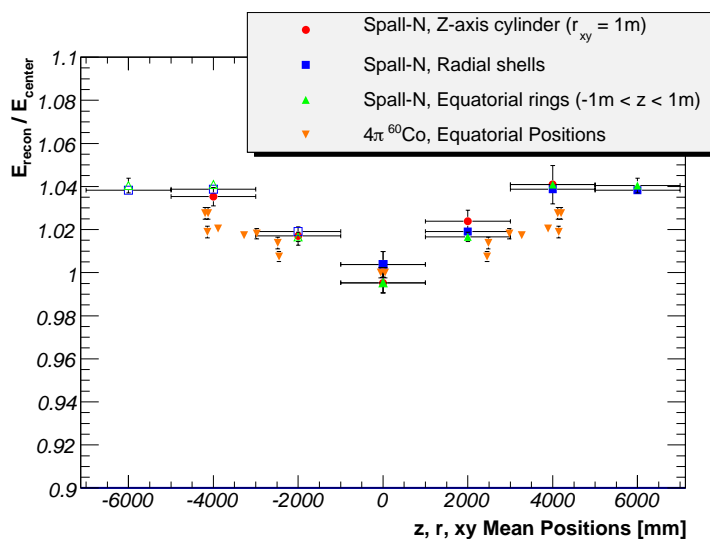


Figure 6.14: The reconstructed energy from 4π source deployments away from the central vertical axis of the detector. The energy for spallation neutrons within specific geometric regions also shown. The reconstructed energies are normalized at the detector center. The open symbols are reflected copies of the closed symbols. The observed bias of the reconstructed energy is similar to the bias in z-axis positions shown in Fig. 6.13.

E_v for a single stopping particle is predominantly direct ionization and scintillation E_q , but there is an additional component from absorption and reemission of Čerenkov light E_c ,

$$E_v = E_q + k_c E_c. \quad (6.8)$$

The parameter k_c represents the fraction of the Čerenkov light converted to visible photons in the scintillator. The direct ionization and scintillation is corrected for quenching; this is done using a standard Birk's empirical correction law of the form,

$$\frac{dE_q}{dx} = \frac{\frac{dE}{dx}}{1 + k_b \frac{dE}{dx}}. \quad (6.9)$$

The total “quenched” energy is,

$$E_q = \int_0^E \frac{1}{1 + k_b \frac{dE}{dx}} dE. \quad (6.10)$$

The quenching correction for each particle type in the KamLAND scintillator is separately approximated. Tables of the particle energy loss were computed from the Electron Gamma Shower (EGS: e^- , e^+ , γ) and Stopping and Range of Ions in Matter (SRIM: p , α) software packages [1, 2]. A correction accounts for a systematic effect caused by a finite threshold for low energy particles in the simulation. The parameter k_0 is introduced, representing the fraction of the energy below the tracking threshold E_{lost} converted to visible energy. The parameter a_0 accounts for the overall normalization of the visible energy units, so that $E_v = E_{real}$ for ^{60}Co events. The visible energy is,

$$E_v = a_0 (E_q(k_b) + k_0 E_{lost} + k_c E_c). \quad (6.11)$$

The four parameters in the expression above are estimated using calibration sources at the detector center, spallation neutron capture events, and high energy α -particle events from

contaminants. The energy of the distributed sources are corrected for the observed position dependent energy biases. The α -particle events provide a strong constraint on the Birk's constant k_b , while the high energy γ events constrain the Čerenkov contribution. The fit is shown in Fig. 6.15, and the results are summarized in Table 6.3. The poor reduced χ^2 of the fit (~ 2) is due to a discrepancy between the ^{60}Co and ^{65}Zn mean energies. ^{60}Co decays produce two $\sim 1\text{ MeV}$ gamma rays; each should be quenched like the single gamma ray from ^{65}Zn which has similar energy (see Tab. 4.2). The entry for ^{60}Co appears on Fig. 6.15 at a real energy of roughly 1 MeV . The reconstructed energy of ^{60}Co is 0.5% lower than expected from the quenching of ^{65}Zn . Inflating the uncertainty in the ^{60}Co mean energy gives a good χ^2 (~ 1); best fit parameters shift less than 0.5σ .

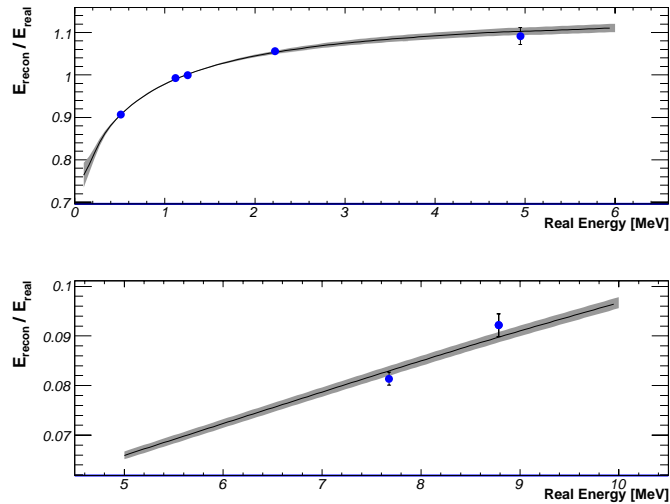


Figure 6.15: Fit to calibration source deployments at the center, spallation neutrons, and high energy α -particle events are used to determine the detector energy response. The model includes a quenching correction and Čerenkov light.

A Gaussian smearing is introduced in the visible energy model to obtain the expected reconstructed energies. The width of the Gaussian, σ_e , has two components: a

Table 6.3: The determined parameters in the detector energy response model. k_b is the Birk's constant. k_0 is the fraction of energy below the EGS simulation threshold which is converted to visible light. k_c is the fraction of Čerenkov light that is converted to visible light. a_0 is a normalization constant defined such that $E_v = E_{real}$ for ^{60}Co events.

Parameter	Estimate
a_0	1.08 ± 0.02
k_b	$0.00985 \pm 0.00021 \text{ g cm}^{-1} \text{ MeV}^{-1}$
k_0	0.737 ± 0.084
k_c	0.372 ± 0.083

constant contribution due to dark noise (σ_0), and an energy-dependent portion due to photon statistics ($\sigma_1\sqrt{E/1\text{MeV}}$),

$$\sigma_e^2 = \sigma_0^2 + \sigma_1^2 \frac{E}{1 \text{ MeV}}. \quad (6.12)$$

Fig. 6.16 displays the fit to the energy resolution versus energy. At low energies the resolution deviates from the model.

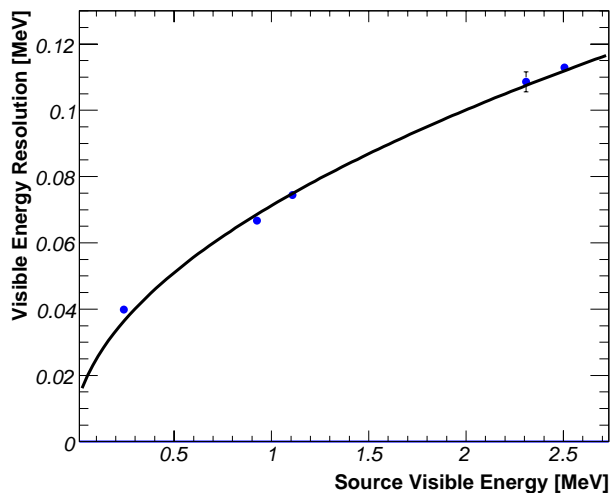


Figure 6.16: The reconstructed energy resolution for calibration sources.

6.5 Muon Track Reconstruction

Cosmic ray muons normally do not stop in the detector. Light is emitted along the track. The muon trajectory is estimated by the distribution of PMT signals in the detector.

6.5.1 The “Fastest-Light” Model

Given a muon trajectory, the “fastest-light” model estimates the PMT hit times. The very high light levels ensure that a PMT hit is caused by the earliest photon emitted (Fig. 6.17). The validity of this assumption is sound since there are ~ 200 detected photoelectrons per MeV of deposited energy, and a minimum-ionizing particle deposits about $2 \text{ MeV g}^{-1} \text{ cm}^2$. While the large number of photons produced by the scintillator insure that these assumptions are valid for muon in the LS, it is less certain for events in the buffer oil. Nonetheless, the fastest-light fitter also does well with these tracks.

The estimated shortest photon arrival time to any PMT is obtained by assuming c for the muon speed, and (c/n) speed of photons radiated from the track. The common feature is that the light path from the muon track to the PMT is at a constant angle relative to the muon track. This angle turns out to be the same as the Čerenkov angle, although the light is assumed to radiate isotropically. A single speed of light (c/n with $n = 1.45$) is used in the fitter. The value of n is taken from independent measurements of these compounds. The neglected differences of the index of refraction between scintillator and mineral oil as well as the variation with wavelength only effect the results at the percent level.

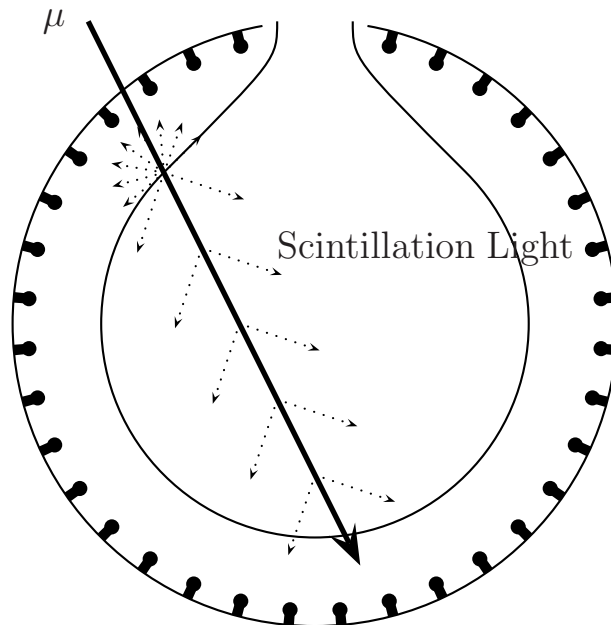


Figure 6.17: The “fastest-light” model for muon fitting. Taking the muon speed as c and the number of scintillation photons as very large, the PMT hit time is given only by the muon trajectory and the speed of light within the scintillator.

6.5.2 “Fastest-Light” Likelihood and Minimization

The likelihood function for the fastest-light fitter is,

$$L(\vec{x}) = \sum_{17''} P(t_i - t_{fastest}(\vec{x})). \quad (6.13)$$

where the probability distribution $P(\Delta t)$ has the form of a Gaussian with an exponential tail (Fig. 6.18). A 1% broad component accounts for uncorrelated signals. The parameters of $P(\Delta t)$ are empirically estimated.

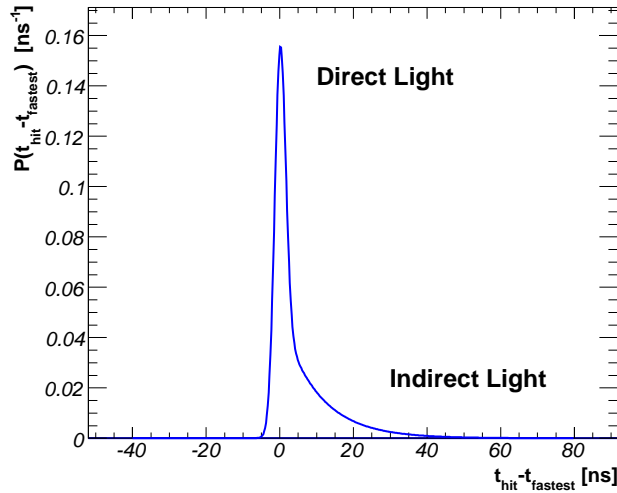


Figure 6.18: The PMT hit time probability distribution for muon events. The peak is from PMTs which are hit by light following the fastest trajectory. The tail is from PMTs which fire on “late” light. The shape is roughly a Gaussian with an exponential tail.

The Minuit minimization utility [59] is used to vary the estimated track position until the effective $\chi^2 = -2\text{Log}(L)$ is minimized. If the final χ^2 of the fit is poor ($\chi^2/\text{dof} \gg 1$), the resulting track is not accepted for use in the analysis.

6.5.3 Performance

The fastest-light fitter successfully fit 30127481 of 30378844 muon events (99%). The distributions of azimuth, zenith and impact parameter for non-showering LS muons are displayed in Fig. 6.19. The *impact parameter* b is defined as the distance of closest approach to the detector center. Overlaid on the histograms are the results of a MUSIC simulation [16] of muons propagating from above ground using a map of the local topography. The angular reconstruction is roughly consistent with the simulation, except for an excess of horizontal and upward muons. The incoming flux of muons should be uniform across any slice of the inner detector, yielding a flat distribution in the square of the impact parameter. The excess of muons at the boundary of the scintillating region, at the detector center, and with $\cos\theta = 0$ are artifacts of the fitting algorithm. The simulation shows the raw muon distribution and will not account for muon fitting effects. Only muons with $\cos\theta > 0.2$ are simulated.

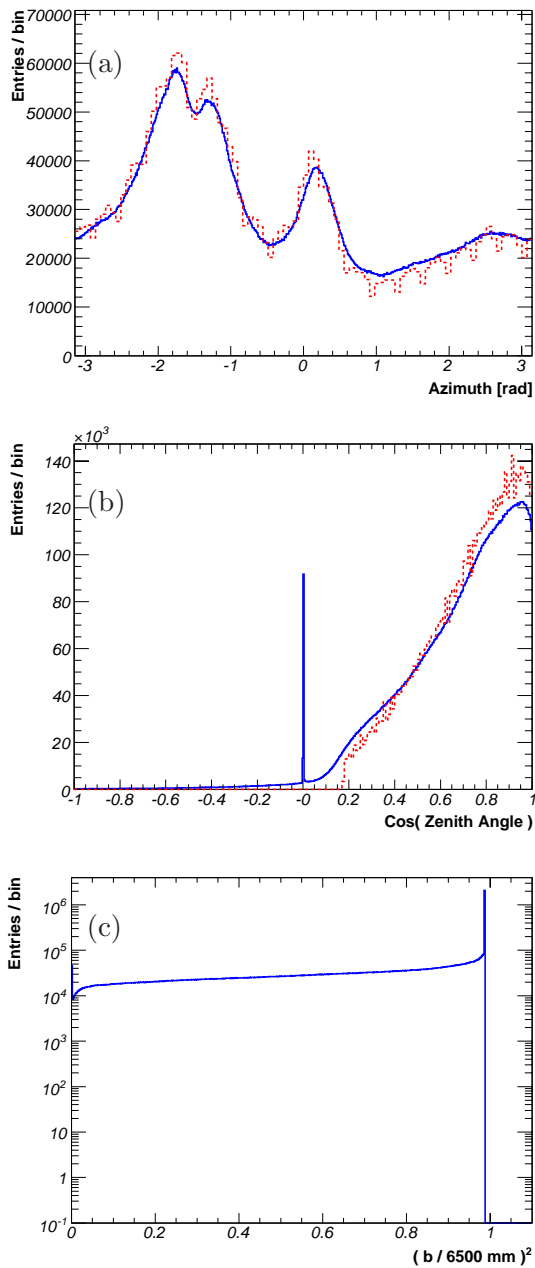


Figure 6.19: The reconstructed azimuth, zenith and impact parameter distributions for non-showering LS muons. A simulation of muon propagation through the mountain is shown with the dashed curves.

Chapter 7

Muon Spallation

Cosmic ray muons produce backgrounds for the reactor antineutrino experiment. Although the muons themselves are easily identified, they often activate the detector material through spallation, producing secondary backgrounds. Spallation products, liberated neutrons and unstable nuclei, produce backgrounds that can sometimes be associated with the muon and rejected. The inefficiency in this procedure must be taken into account.

7.1 Muon Rates

Using the muon categories discussed in Chap. 6, histograms of the time between muon events are constructed. Uncorrelated events should follow simple exponentials characteristic of the muon rate. The fitted rate for each run are shown in Fig. 7.1. Electronics effects frequently produce spurious triggers within $50\mu s$ following muons; the rate is fit excluding this period. Noise in the outer detector produces many events falsely identified as OD muons. 119 OD PMTs have died; the failures are attributed to water shorting the

Table 7.1: Summary of the predicted and detected muon rates with statistical errors.

Muon Type	Predicted Rate [Hz]	Measured Rate [Hz]	χ^2 / d.o.f.
OD Muons	0.73	$0.62 \sim 0.64$	-
Oil Muons	0.15	0.1322 ± 0.0001	1488 / 1447
LS Muons	0.21	0.2046 ± 0.0001	1582 / 1447

cable attachments at the PMT base. The loss of PMTs has reduced the detected rate of OD muons over time. Averaging all the runs provide the rates and statistical errors in Table 7.1, as well as the χ^2 . The predicted rate is estimated from the detector geometry using the muon rate measured by the Kamiokande experiment.

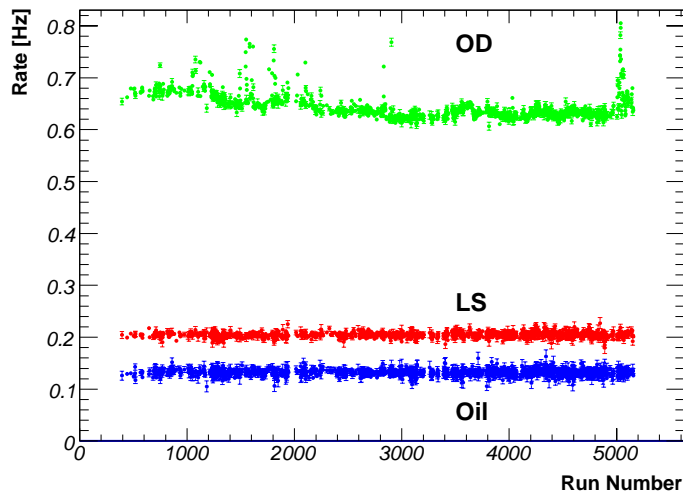


Figure 7.1: The OD, Oil, and LS muon rate for each run.

7.2 Spallation Neutrons

Muons passing through the detector and surrounding rock often generate neutrons which cause radiative captures, (n,p) and (n, α) reactions. Neutron capture is the delayed

Table 7.2: Thermal Neutron Interaction By Isotope

Isotope	$\sigma_{(n,\gamma)}$ [$b\ atom^{-1}$]	σ_{other} [$b\ atom^{-1}$]	Rel. Capture Rate	(n, γ) Q-value [keV]
^1H	0.3326 ± 0.0007		1	2224.57
^2H	$5.19 \pm 0.07 \times 10^{-4}$		2.3×10^{-7}	6257.23
^{12}C	$3.53 \pm 0.05 \times 10^{-3}$		5.3×10^{-3}	4946.31
^{13}C	$1.37 \pm 0.04 \times 10^{-3}$		2.3×10^{-5}	8176.44
^{14}N	$7.98 \pm 0.14 \times 10^{-2}$	1.83 ± 0.03^a	1.4×10^{-5}	10833.3
^{15}N	$2.4 \pm 0.8 \times 10^{-5}$		1.7×10^{-11}	2489.1
^{16}O	$1.90 \pm 0.19 \times 10^{-4}$		3.6×10^{-8}	4143.13
^{17}O	$5.4 \pm 0.7 \times 10^{-4}$	0.235 ± 0.01^b	3.9×10^{-11}	8044.03
^{18}O	$1.6 \pm 0.1 \times 10^{-4}$		6.1×10^{-11}	3954.92

^a $\sigma_{(n,p)}$ ^b $\sigma_{(n,\alpha)}$

coincidence signal in inverse beta decay; spallation neutrons are a source of background. Table 7.2 lists the cross sections for thermal neutrons (velocity $v = 2200\text{ m.s}^{-1}$) [69, 3] and relative capture rates on the nuclei in KamLAND liquid scintillator. The relative capture rates are computed using the isotopic abundances in the liquid scintillator given in Table 4.1. Other trace contaminants, including gases dissolved in the scintillator, are not considered. The Q-values [75] are approximately equal to the total energy of the gamma rays emitted as the daughter nucleus decays to its ground state.

7.2.1 Neutron Energy Spectrum

Figure 7.2 shows the background subtracted visible energy spectrum following muon events. A window selects spallation neutron capture events while avoiding instrumental effects present in the first $50\ \mu\text{s}$. Only the time to the previous muon is histogrammed and only isolated muons are included in the sample. An isolated muon for this analysis is one that is not preceded or followed by another muon within 5.45 m.s . The ^1H capture peak

is found to be at 2.435 MeV visible energy. The ^{12}C capture fits at 5.486 MeV . Energy shifts may result from the poorly modeled shoulders to the left of each peak, as well as the spatial variation of reconstructed energy. The shoulders are a result of electronics effects observed in the first millisecond after a detected muon. A second-order polynomial was used to approximate this background, but it does not properly describe the biased spectrum. Figure 7.2 includes the expected peaks from neutron captures on ^{13}C and ^{14}N , but there are no statistically significant peaks after subtraction of the ^{12}B and ^{12}N beta decay spectra.

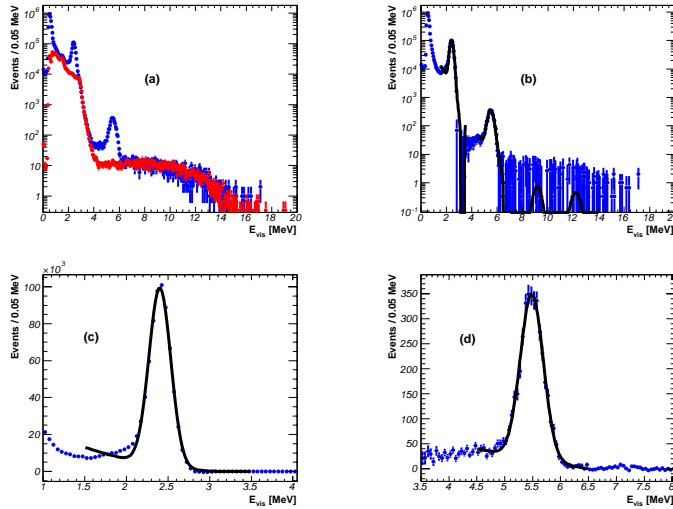


Figure 7.2: Energy spectrum of events between 0.05 ms and 1.4 ms after inner detector muons. A window between 1.4 ms and 5.45 ms is used for background subtraction. (a) Counts in the signal (blue) and background (red) windows. (b) Background-subtracted spectrum and fits, plus the estimated ^{13}C (9 MeV) and ^{14}N (12 MeV) capture peaks. (c) ^1H capture gamma ray peak. (d) ^{12}C capture gamma ray peak.

One method to avoid the post-muon instrumental effects is to consider only those events occurring a long time after muons. A signal window from 1.0 ms to 1.4 ms after the muon event gives the spectra shown in Fig. 7.3. The ^1H capture peak is found at

$2.435 \pm 0.002 \text{ MeV}$ visible energy. The ^{12}C capture is at $5.52 \pm 0.02 \text{ MeV}$. Considering the ratio of the number of captures on ^{12}C to ^1H , $(5.5 \pm 0.8) \times 10^{-3}$ is found, with 5.33×10^{-3} expected (Table 7.2). The electronic effects do not seem to distort the energy fits using the later signal window.

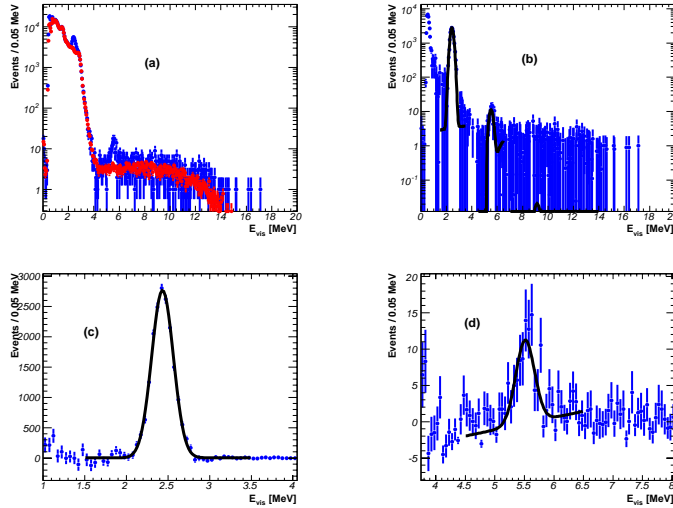


Figure 7.3: Background subtracted energy spectrum in the 1.0 ms to 1.4 ms window after inner detector muon events, with a window from 1.4 ms to 5.45 ms for background subtraction. (a) Counts in the signal (blue) and background (red) windows. (b) Background-subtracted spectrum and fitted curve, plus the estimated ^{13}C and ^{14}N capture peaks. (c) ^1H capture gamma ray peak. (d) Region of the expected ^{12}C capture gamma ray peak.

7.2.2 Neutron Rate

Electronics effects following muons make it difficult to determine the rate and capture time of spallation neutrons. The event delay following muons is shown in Fig. 7.4. Only isolated muons are used, but in this analysis an isolated muon is one which is not preceded or followed by another muon event within 10 ms . The $nsummax$ is required to be greater than 250 for events following muons to avoid backgrounds below the neutron

capture energy region. The shape should be an exponential showing the neutron capture time plus a flat background. The full range of the distribution in Fig. 7.4 is not well-fit with an exponential due to the electronics effects. The duration and size of the electronics effect are explored by varying the lower edge of the fit window from 0.15 ms to 2 ms (see Fig. 7.5). The upper edge of the fit is held constant at 10 ms . The fit quality is poor ($\chi^2/\text{d.o.f} > 1$) when data within 0.8 ms of the muon event is included. Starting the fit from 0.8 ms to 1.5 ms results in valid exponential fits with capture times which are of the right order. Unfortunately, the statistics of the fits become very poor and a consistent capture time is not obtained from fit to fit. For windows starting beyond 1.5 ms from the muon, the statistics are too low to detect capture events.

A rough estimate of the total number of neutron captures is obtained using the fit starting at 1 ms from the muon. An exponential fit gives $3.3 \pm 0.6 \times 10^6$ neutron events following 29721115 muons. With the ID muon rate of 0.33 Hz , a total spallation neutron capture rate of 0.037 Hz is obtained for the liquid scintillating volume.

Instrumental distortions are suppressed by avoiding periods of exceptionally high event rates following muons. The *multiplicity* of a muon event is defined as the number of events triggering the inner detector for 0.15 ms to 10 ms after the muon. The distribution of observed multiplicities is shown in Fig. 7.6. The sample is divided according to ranges of multiplicity, and the capture time is fit for each set in the time window of 0.15 ms to 10 ms following the muon. The muon events with multiplicity of 75 or more (0.2%) produce poor fits as indicated by the χ^2 values in Fig. 7.7. Using the muons with multiplicity less than 75, the capture time is $207.5 \pm 0.3\mu\text{s}$ (χ^2/dof : 188 / 194). This method improves the

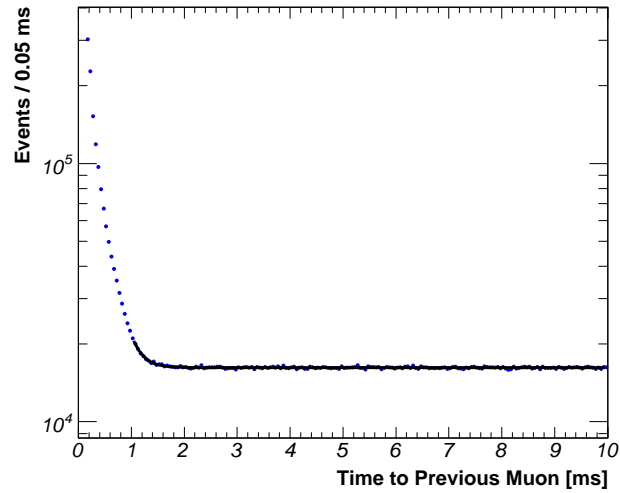


Figure 7.4: A fit to estimate the neutron capture rate using event delay after a detected muon. A fit starting at 1 *ms* after the muon gives a mean capture time of $199 \pm 8 \mu\text{s}$.

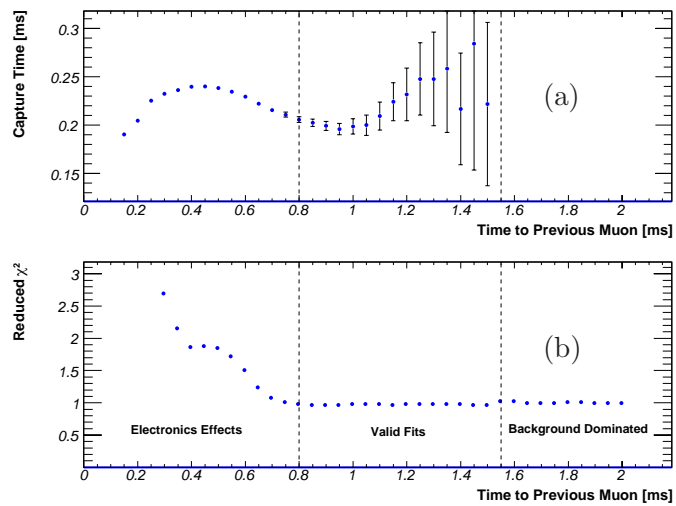


Figure 7.5: (a) The fitted neutron capture time from Fig. 7.4 versus the fit range. (b) The reduced χ^2 of the fit versus fit range.

measurement of the capture time, but it is not used to determine the number of spallation neutron captures. Removing the muon events with high multiplicity distorts the estimate of the number of neutron captures.

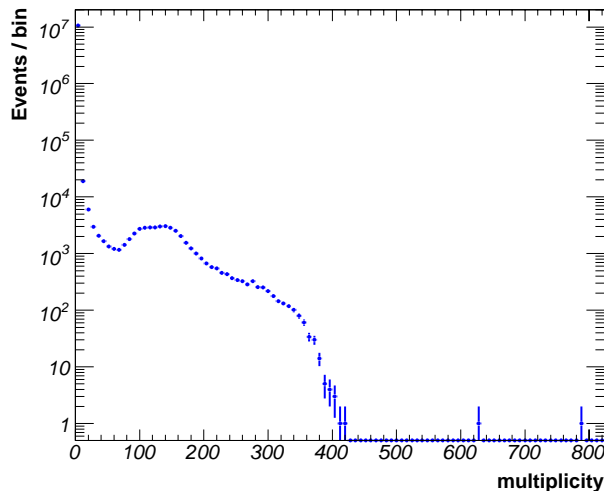


Figure 7.6: Multiplicity distribution for muon events.

7.2.3 Spatial Distribution of Neutron Capture Events

The distribution of neutron capture events is expected to be uniform over the detector volume. The muon flux does not vary over the dimensions of the detector, and the scintillator and buffer oil provide an essentially uniform neutron production target.

Figure 7.8 shows the background subtracted radial distribution of spallation neutron captures. Events are selected with a 1 ms to 1.4 ms window after muons, with a 2 ms to 5 ms window for background subtraction. The distribution is uniform within the active volume used in the reactor experiment ($r < 5.5\text{ m}$).

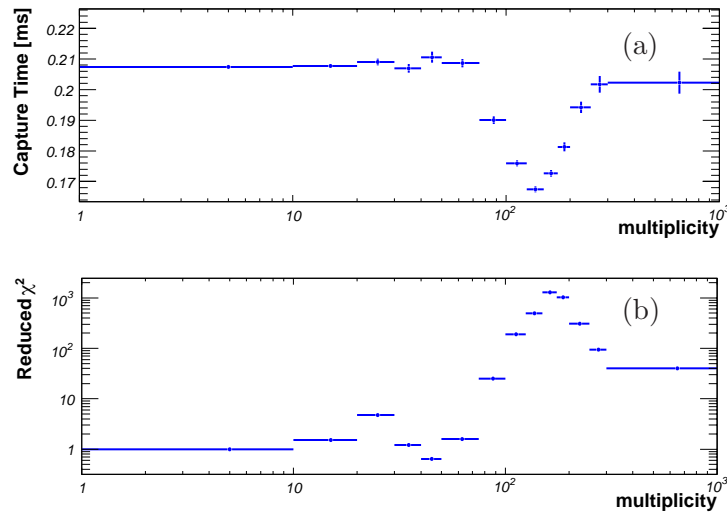


Figure 7.7: Fitted neutron capture time (a) and reduced χ^2 (b) plotted against multiplicity of the previous muon.

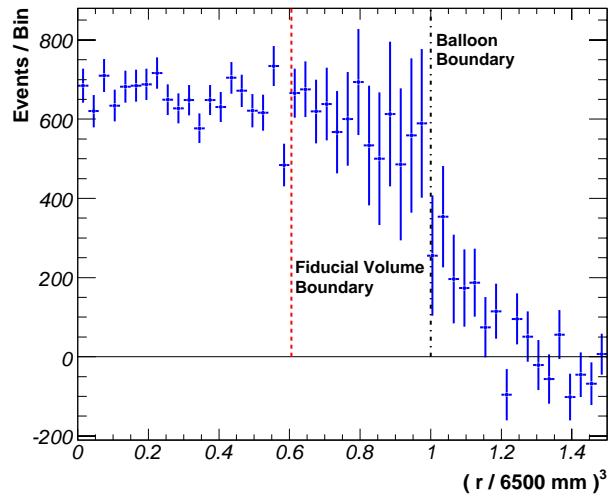


Figure 7.8: The background-subtracted distribution of neutron capture events in the inner detector volume. The solid vertical line roughly represents the balloon radius separating the liquid scintillator from the buffer oil. The dotted vertical line indicates the analysis cut placed to avoid radioactive backgrounds near the balloon surface.

7.3 Boron and Nitrogen

Muon interactions in the detector produce the β -decaying isotopes ^{12}B ($\tau_{1/2} = 20.20\text{ ms}$, $\Delta Q = 13.37\text{ MeV}$) and ^{12}N ($\tau_{1/2} = 11.000\text{ ms}$, $\Delta Q = 17.34\text{ MeV}$). The delayed-coincidence requirement excludes these β -decays as a background for the reactor analysis. They provide a uniformly distributed calibration source for energetic events.

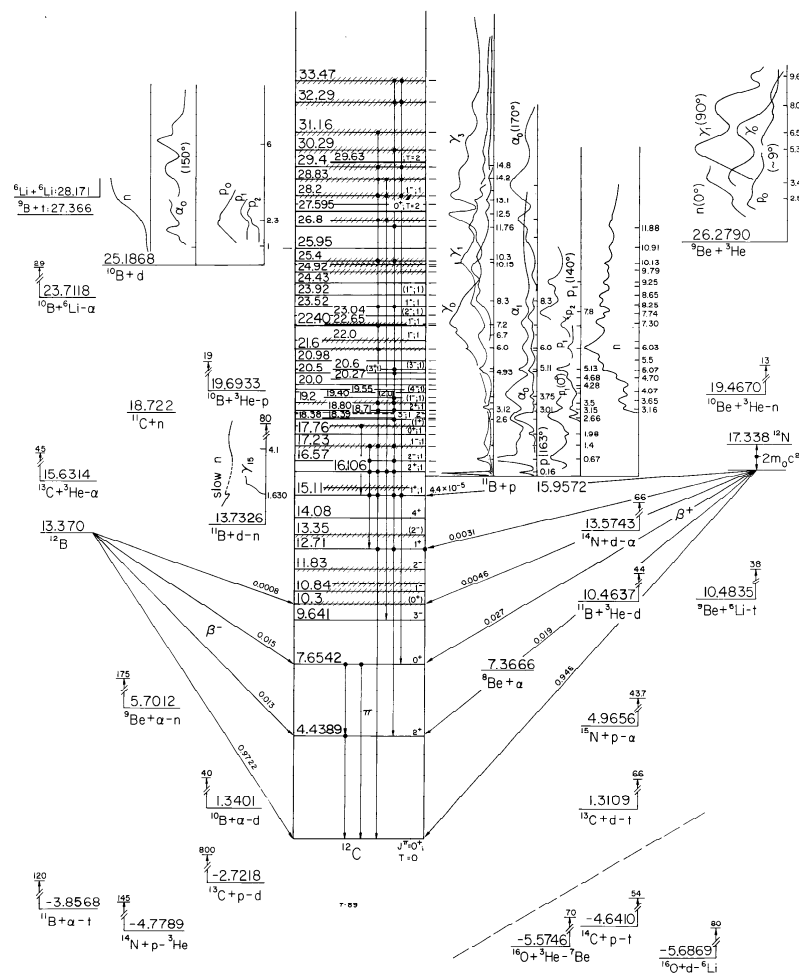


Figure 7.9: Decay scheme for ^{12}B and ^{12}N . [13]

7.3.1 ^{12}B and ^{12}N Energy Spectrum

Boron and Nitrogen decays are selected with a window from 2 ms to 52 ms following inner detector muons; with a 52 ms to 252 ms window for background. Events are also required to be within the analysis volume ($r < 5.5\text{ m}$) and to follow isolated muon events ($\Delta t_{next\mu} > 1\text{ s}$ and $\Delta t_{last\mu} > 1\text{ s}$). In Fig. 7.10, the characteristic beta decay spectrum is evident above 4 MeV ; below this energy the signal is lost in the background. The fit is consistent with solely ^{12}B in the range of 4 MeV to 14 MeV , and allow for a calibration of the detector at high energies. The small number of events between 15 MeV and 18 MeV indicates a small contribution from ^{12}N .

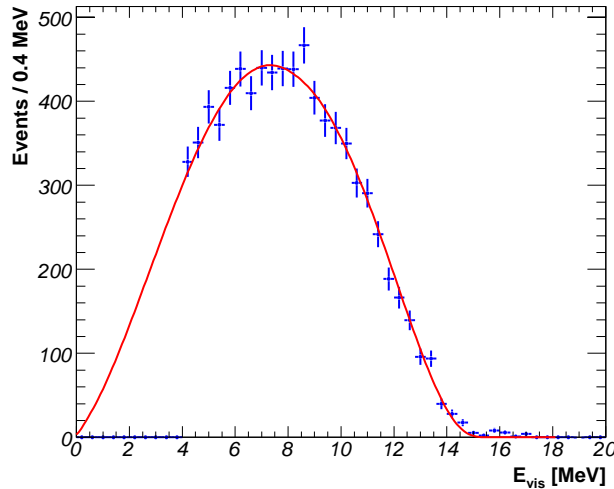


Figure 7.10: The fitted background subtracted visible energy spectrum of events in the ^{12}B and ^{12}N time window following muons.

7.3.2 ^{12}B Decay Rate

The time distribution in Fig.7.11 is from events with visible energy above 5 MeV in the 4 ms to 1 s window following isolated muons. The half-life is $20.0 \pm 0.3\text{ ms}$ (χ^2/dof : $233/245$), consistent with ^{12}B . The fit includes a contribution from ^9Li and a uniform background. Alternate fits including a contribution from ^{12}N result in rates of this isotope consistent with zero. The total number of ^{12}B events above the 5 MeV threshold is $1.73 \pm 0.02 \times 10^4$. With 15148397 isolated muons in this data sample, the ^{12}B rate with visible energy above 5 MeV is $4.19 \pm 0.05 \times 10^{-4}\text{ Hz}$ ($36.1 \pm 0.4\text{ day}^{-1}$) in the scintillating volume.

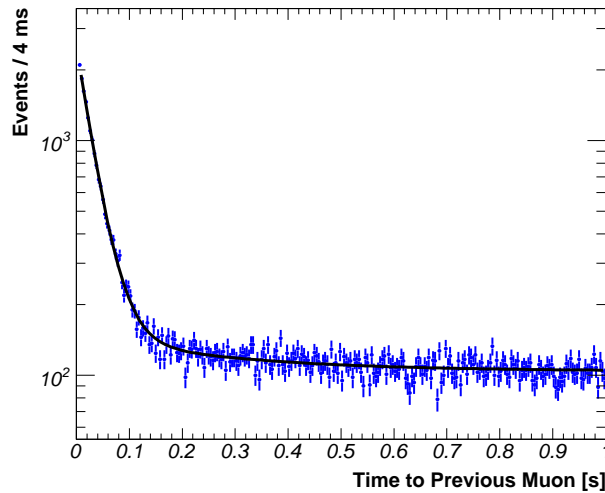


Figure 7.11: Time spectrum of events with $E_{vis} > 5\text{ MeV}$ (2 ms to 1 s after an isolated muon). The fit yields a half-life of $20.0 \pm 0.3\text{ ms}$, consistent with the expected half-life of ^{12}B (20.2 ms). A longer-lived exponential with the half-life of ^9Li is included in the background.

7.3.3 Spatial Distribution of ^{12}B Decay Events

With its longer half-life, ^{12}B decay events are not effected by detection effects seen for spallation neutrons. The spatial distribution should be uniform except near the balloon surface due to the imperfect spherical shape of the scintillating volume and a decrease in efficiency at the very edge of this volume. Remaining distortions away from the balloon edge are attributed to reconstruction systematic error. The normal event selection criteria excluding the radial cut and a wider reconstructed energy cut from 4 MeV to 20 MeV , is used. After background subtraction, the distribution in Fig. 7.12 is obtained.

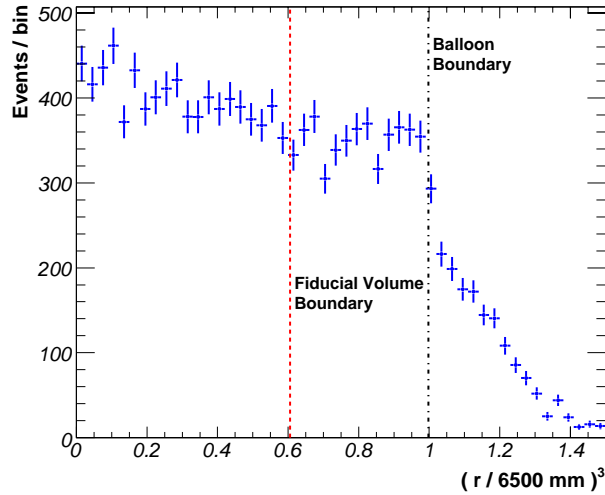


Figure 7.12: The background-subtracted radial distribution of ^{12}B decays in the inner detector.

7.4 Lithium and Helium

Potentially important spallation backgrounds for the reactor experiment come from ^9Li ($\tau_{1/2} = 178.3\text{ ms}$, $\Delta Q = 13.61\text{ MeV}$) and ^8He ($\tau_{1/2} = 119.0\text{ ms}$, $\Delta Q = 10.65\text{ MeV}$)

β -decays. These isotopes sometimes beta decay to neutron unstable daughter states, mimicking the antineutrino delayed-coincidence signal. The decay schemes are displayed in Fig 7.13 and Fig 7.14. The long lifetimes relative to the period between muons makes a simple time-based veto impractical. The long-lived spallation products should appear with the same cuts used to select reactor antineutrinos (see Table 8.1).

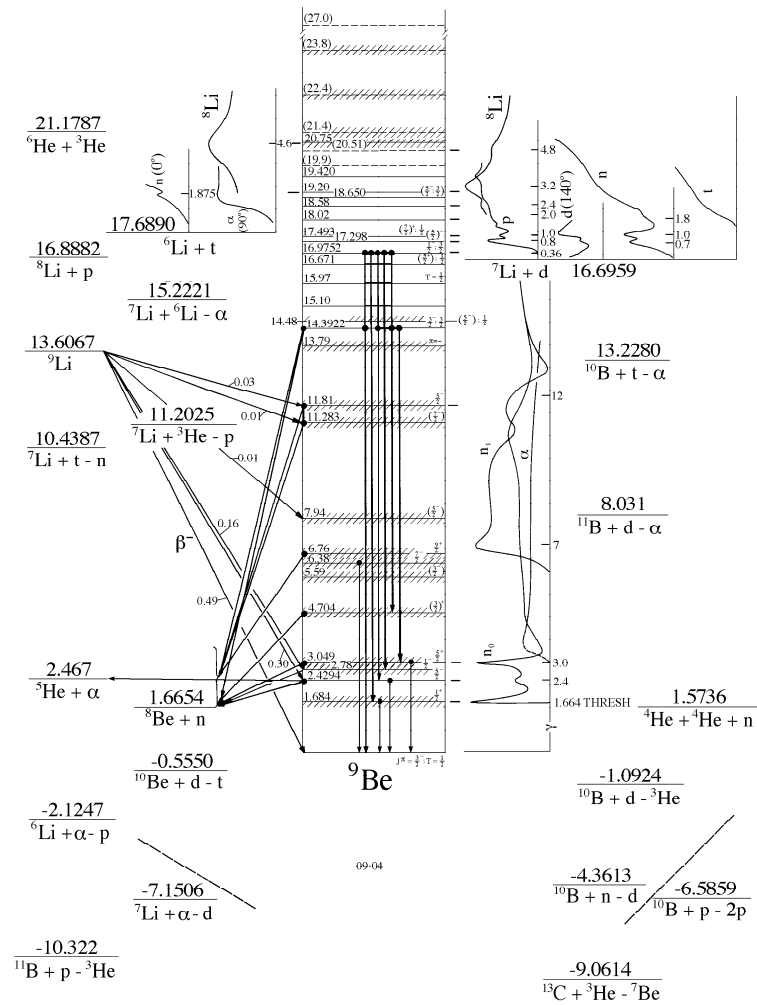


Figure 7.13: Decay scheme for ${}^9\text{Li}$. The branches where the daughter nucleus emits a neutron are sources of delayed-coincidence backgrounds. Figure taken from Ref. [81].

7.4.1 Decay Rate of ${}^9\text{Li}$ and ${}^8\text{He}$

Figure 7.15 shows the time since muons in the scintillator of all the delayed-coincidence events. ${}^9\text{Li}$ and ${}^8\text{He}$ lifetimes are not negligible relative to the muon rate, so it is important to include an entry for all LS muons in the previous 2 s for proper background normalization. Including a possible contribution of ${}^8\text{He}$ in the fit, the result is consistent with no contribution from this isotope. Using the known half-life of ${}^9\text{Li}$, a value of 782 ± 35 total events is obtained (χ^2 / dof : 41.9 / 28).

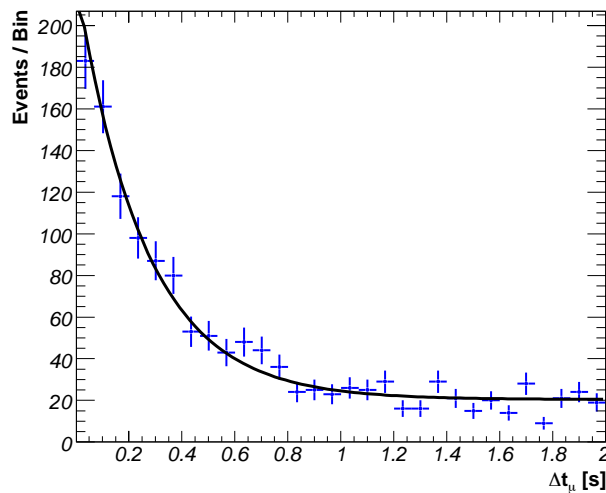


Figure 7.15: The delayed-coincidence event time spectrum 2 s after all muons in the scintillating volume.

7.4.2 Energy Spectrum of ${}^9\text{Li}$

Figure 7.16 shows the background subtracted ${}^9\text{Li}$ prompt event spectrum. The delayed events are selected with the antineutrino cuts in Table 8.1, but without a 2 s muon veto cut. A window from 0.002 s to 1.001 s for the signal and 1.001 s to 2 s for the background

leads to the spectrum in Fig. 7.16. A small effect from the decay of the daughter nucleus into two alpha particles and a neutron is not included [71, 74].

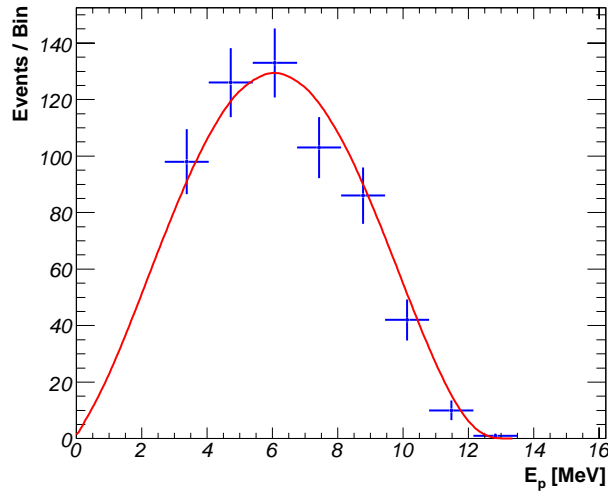


Figure 7.16: The background subtracted ${}^9\text{Li}$ prompt reconstructed energy spectrum and the expected curve. The curve does not include a small effect from the fragmentation of the daughter nucleus into two alpha particles and a neutron [71, 74].

7.4.3 Spatial Distribution of ${}^9\text{Li}$ Events

The mean of the prompt and delayed event positions is taken as the location of the ${}^9\text{Li}$ event. Figure 7.17 shows the spatial distribution of ${}^9\text{Li}$ delayed-coincidence events in the detector. The effect of the 5.5 m radial cut used in the event selection is evident in the figure. The distribution is statistically flat within the 5.5 m radius.

7.5 Showering Muons and Spallation Production

The majority of cosmic ray muons are minimum ionizing, depositing roughly 2 MeV of energy per centimeter of track length. For minimum ionizing events the total

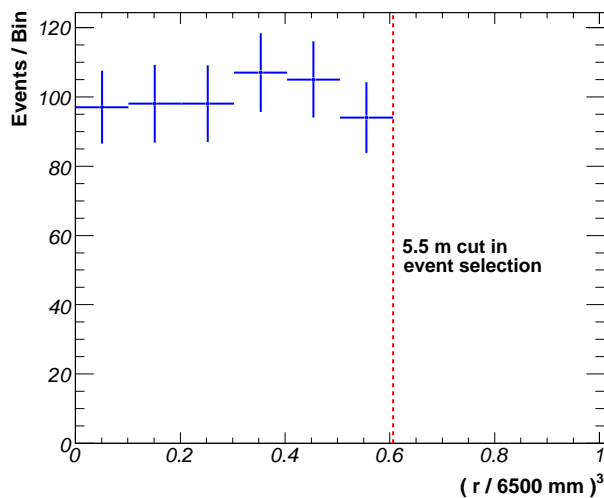


Figure 7.17: Radial distribution of the mean of the ${}^9\text{Li}$ prompt and delayed (neutron capture) events.

detected light is linearly related to track length. A smaller amount of light is produced in the mineral oil buffer region. Some muons produce significantly more light in the inner detector. Electromagnetic and hadronic showers are the cause of this excess light.

The top panel of Fig. 7.18 shows the distribution of light collected L_μ in the inner detector from muon events. The smaller peak is from muons passing through the buffer oil region (Oil muons); the higher-light peak is from LS muon events. The 10.7% of muon events above the dashed line are expected to be dominated by showering muons and the light collected for these events is up to ten times greater than minimum ionizing. The lower two panels indicate the light collected in the muon events preceding ${}^{12}\text{B}$ and ${}^9\text{Li}$ spallation events. It is evident that spallation events are dominated by a showering muons.

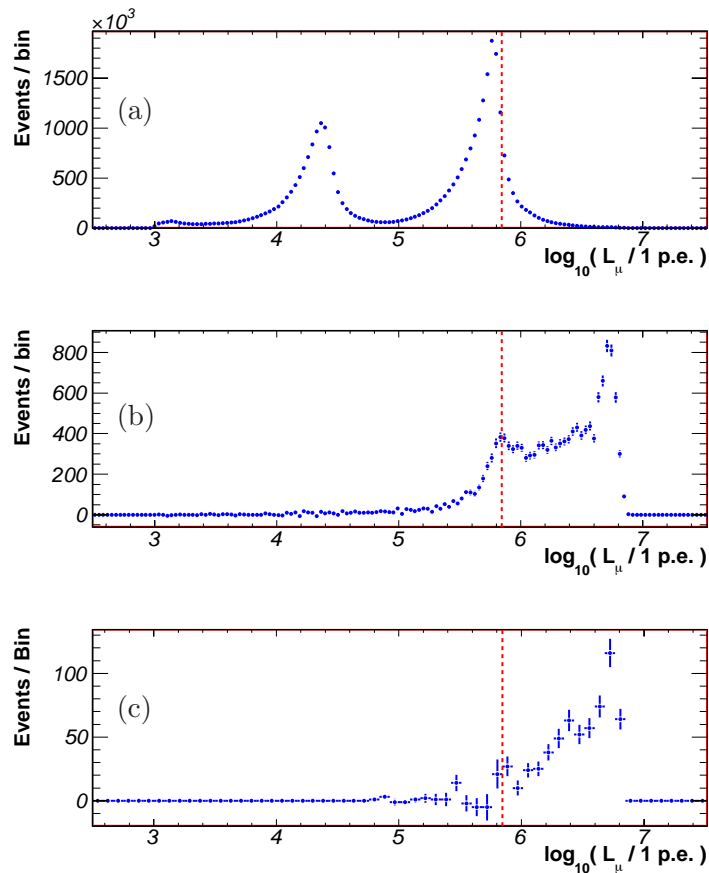


Figure 7.18: (a) The light collected L_{μ} from muons in the inner detector (logarithmic scale). The events in the lower peak are from the buffer oil region. The second peak is from the LS. (b) The light collected from muons preceding ^{12}B spallation events. The peak at the high end of the range is from saturation of the detector. (c) The light level preceding ^9Li events. Muon events to the left of the vertical dashed line are classified as showering muons.

Chapter 8

$\bar{\nu}_e$ Selection

The trigger rate in KamLAND is about 40 per second, but less one a day from inverse beta decay of an antineutrino. This chapter outlines the method of finding $\bar{\nu}_e$ interactions. The first section is a description of the delayed-coincidence signal expected in KamLAND. Then follows a description of the backgrounds, the criteria used to separate signal from background, and the systematic uncertainties. The antineutrino selection reduces the target volume and livetime. The detector exposure is estimated in the final section.

8.1 Reactor Antineutrino Signal

Inverse beta decay on a proton produces a positron and a neutron. The positron produces a prompt scintillation signal with energy $E_p \simeq E_\nu - 0.8 \text{ MeV}$. The neutron recoils, thermalizes, and captures in the detector within centimeters of the production point. The capture delay time follows an exponential with a characteristic capture time of $207 \mu\text{s}$, as measured using spallation neutrons (discussed in Sec. 7.2.2). More than 99% of the captures

involve ${}^1\text{H}$, yielding a 2.2 MeV gamma ray. The gamma ray energy is absorbed within tens of centimeters of the capture position. The reconstructed positions of the prompt and delayed events are uncertain with a $\sim 20\text{ cm}$ resolution, measured with calibration sources. The $\bar{\nu}_e$ flux is uniform within the target volume, so the inverse beta decay signals are also uniform.

The characteristics of an antineutrino interaction are:

- The prompt signal has an energy spectrum characteristic of the $\bar{\nu}_e$ energy spectrum and depends on the inverse beta decay cross section.
- The delayed signal has the energy of the 2.2 MeV capture gamma ray.
- The time between the prompt and delayed signals should follow an exponential with time constant of $207\ \mu\text{s}$ as measured with spallation neutrons.
- The mean distance between the prompt and delayed signals is tens of centimeters.
- The positions of the prompt and delayed signal pairs are uniform within the target volume.

8.2 Backgrounds

The backgrounds for the reactor antineutrino analysis come from either uncorrelated or correlated signal pairs. Uncorrelated signals are mostly eliminated with the delayed-coincidence condition, except for randomly correlated events from the uncorrelated signal. Such signals are called *accidental coincidences*. Correlated backgrounds are from interactions producing both a prompt and a delayed signal, which can be mistaken for

the inverse beta decay signal. Fast neutrons, ${}^9\text{Li}$ decay, and α -induced backgrounds cause correlated signals.

8.2.1 Accidental Coincidences

The rate, position distribution, and energy spectrum of randomly correlated events characterize the uncorrelated signals. The singles rate increases near the balloon radius ($\sim 6.5\text{ m}$), and is high in the chimney region at the top of the scintillator volume as seen in Fig. 8.1. The singles rate is highest at the detector threshold ($\sim 0.8\text{ MeV}$), declining rapidly at higher energies as shown in Fig. 8.2. By ignoring delayed-coincidence pairs which occur at high radius and low energy, the background contribution is reduced.

8.2.2 Muon Spallation

Spallation Neutrons

Cosmic ray muons liberate neutrons by spallation. Neutron capture mimics the delayed signal of an antineutrino interaction. The background is reduced by ignoring events correlated with muon interactions. Since the neutron capture time ($207\ \mu\text{s}$) is short relative to the time between muon interactions ($\sim 3\text{ s}$), this does not significantly reduce the experimental livetime.

${}^9\text{Li}$ Correlated Background

Muon spallation produces ${}^9\text{Li}$ nuclei uniformly in the scintillator volume. 50% of ${}^9\text{Li}$ beta decays ($\Delta Q = 13.61\text{ MeV}$) are associated with neutron emission. Neutron delayed beta decay mimics the prompt positron signal and the neutron capture of antineutrino

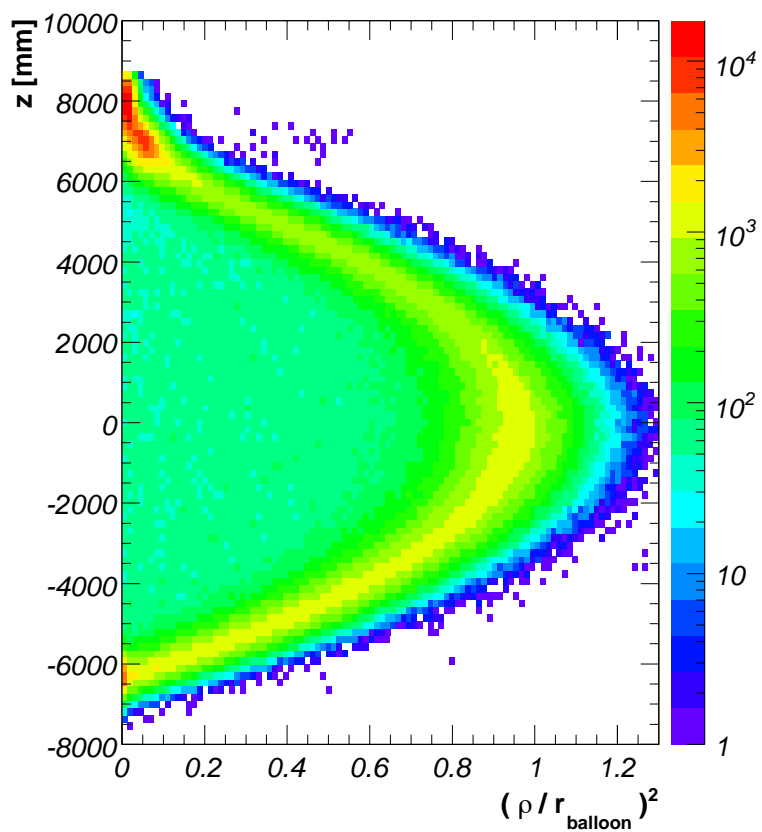


Figure 8.1: The reconstructed position of interactions in the detector for one day of livetime. In this figure, $\rho^2 = x^2 + y^2$. The color indicates the relative rate as shown in the legend on the right. The density of events is highest in the chimney region ($z \sim 8000 \text{ mm}$) and near the balloon surface ($r \sim 6500 \text{ mm}$).

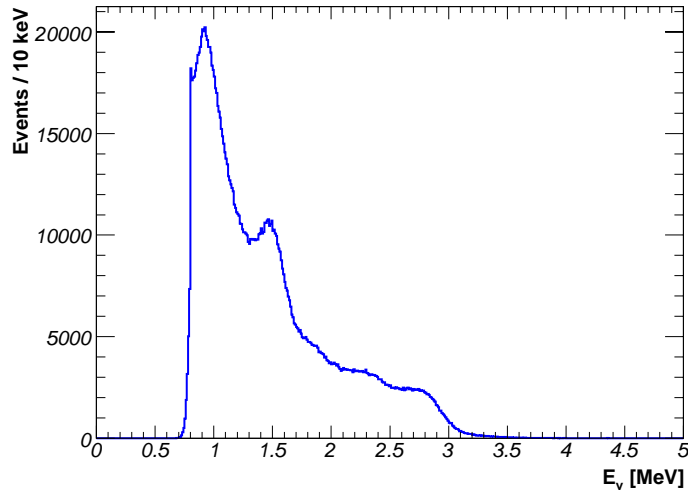


Figure 8.2: The reconstructed energy spectrum of interactions in the detector for roughly one day of livetime. The rate of singles events is highest just above the detector threshold (~ 1 MeV), and declines steeply at higher energies.

interactions. The background is identified by correlating the ${}^9\text{Li}$ decays with a previous muon. The half-life of ${}^9\text{Li}$ (178.3 ms) is significant compared to the ~ 3 s between muons in the inner detector. An adequate veto for the entire detector after muons would drastically reduce the livetime. A more involved rejection process is necessary. ${}^8\text{He}$ is another spallation background which emits neutrons, but as noted (Sec. 7.4) there is no evidence of ${}^8\text{He}$ as a background.

8.2.3 High-Energy Alpha Particle Correlated Background

Correlated background comes from high energy alpha decays of radioactive contaminants. The dominant source of high energy alpha particles in KamLAND is ${}^{210}\text{Po}$, a daughter of the ${}^{210}\text{Pb}$ contamination of the scintillator. ${}^{210}\text{Pb}$, in turn, is a daughter of ${}^{222}\text{Rn}$ found in underground facilities. These decays lead to an effectively irreducible

correlated background. Efforts to reduce the ^{210}Pb contamination by purification of the scintillator in KamLAND are underway.

^{210}Po decays emitting a 5.3 MeV α -particle. The visible energy of the alpha particle is quenched below the energy threshold for positrons. However, there is a finite probability that the alpha interacts exothermically with a ^{13}C nucleus, producing ^{16}O and an energetic neutron. This neutron thermalizes through successive elastic scattering, predominantly with protons. The recoil protons, though also quenched, sometime produce a signal above the prompt event energy threshold. The thermalized neutron subsequently captures on a proton, mimicking the delayed event signal.

There are other contributions to the alpha particle background. There is a small probability that the energetic neutron will inelastically scatter on ^{12}C , with the excited carbon nucleus emitting a 4.4 MeV gamma ray. This produces a 4.4 MeV prompt signal with a delayed neutron. There is also a chance that an ^{16}O nucleus from $(\alpha, n)^{16}\text{O}$ is produced in an excited state. The first two excited states are accessible; $\Delta Q = 6.049\text{ MeV}$, which e^+e^- pair decays to the ground state, and $\Delta Q = 6.130\text{ MeV}$, which emits a gamma ray, mimicking the prompt event.

8.2.4 Fast Neutrons

Spallation neutrons can capture and mimic the delayed antineutrino signal. Neutrons produced by muons in the inner detector are rejected by time-correlation with the muon signal. Energetic neutrons produced in the outer detector or in the rock surrounding the detector can travel into the inner detector. The water of the outer detector and the buffer oil region of the inner detector attenuate these neutrons.

The remaining fast neutrons which enter the scintillator volume can produce correlated backgrounds. The fast neutron slows via nuclear interactions producing a prompt signal. The slowed neutron subsequently captures, producing a delayed signal. Alternately, multiple neutrons can enter the scintillator producing a pair of neutron capture events.

8.2.5 Geoneutrinos

Beta decays in the decay chains of naturally occurring ^{238}U and ^{232}Th emit electron antineutrinos, indistinguishable from reactor $\bar{\nu}_e$. These are called geoneutrinos due to their geological origin. KamLAND is the first experiment to measure geoneutrinos [19]. The maximum geoneutrino energy is 3.3 MeV , corresponding to 2.5 MeV positrons from inverse beta decay. Figure 8.3 shows the positron spectrum for the two decay chains. A 2.6 MeV threshold avoids the geoneutrino background.

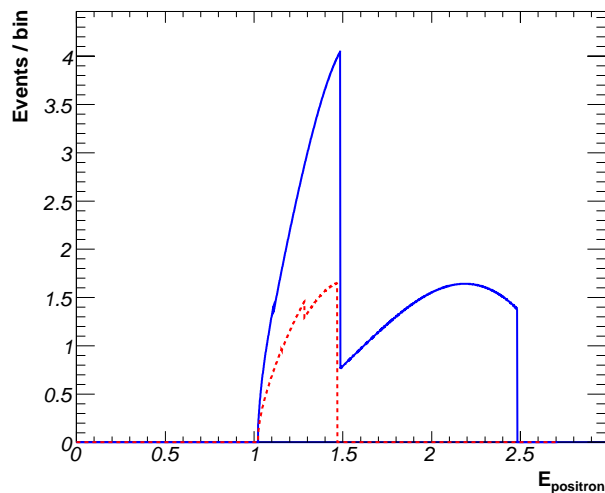


Figure 8.3: The positron spectrum from geoneutrino inverse beta decay: ^{238}U decay chain (solid), ^{232}Th decay chain (dashed).

8.3 Selecting Antineutrino Candidates

The highly efficient signal selection and background rejection necessary in KamLAND are discussed in the following subsections.

8.3.1 Reconstruction Quality

In order to use event positions and energies to identify antineutrinos, the reconstruction must satisfy the validity conditions discussed in Chap. 6. The efficiency is based on the number of events in the *valid* category. Roughly 0.3% of events fail to generate a valid reconstructed position or energy. As shown in Fig. 8.4, the fraction varies with the energy. For $nsummax$ values in the range for antineutrino events ($350 < nsummax < 800$) a reconstruction efficiency of 0.99981 is obtained with negligible statistical error. The efficiency measured using ^{60}Co calibration source data (2.5 MeV) is 0.9996 ± 0.0002 . For ^{68}Ge source data (1.0 MeV) the efficiency is 0.998 ± 0.001 . The cumulative reconstruction efficiency is taken as 0.999 ± 0.001 at all energies in the calculation of the experimental efficiency.

8.3.2 Prompt-Delayed Event Time Separation

The characteristic time between the prompt and delayed event is determined by the neutron capture time in the KamLAND liquid scintillator. The neutron capture time of $207\ \mu\text{s}$ is measured using spallation neutrons. Requiring the delayed event to fall within 0.5 to $660\ \mu\text{s}$ following the prompt event has an efficiency of 0.956 ± 0.001 , where the uncertainty comes from the uncertainty in the capture time.

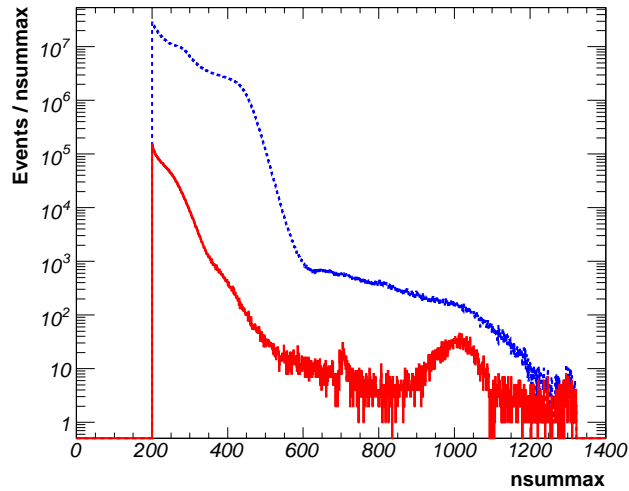


Figure 8.4: The $nsummax$ distribution for all events (dashed) and for events where the position or energy reconstruction failed (solid). Reactor antineutrino events have $nsummax$ values between 350 and 800. The peak of poorly reconstructed events with $nsummax$ values near 1000 is from noise sources external to the detector.

Figure 8.5 shows the antineutrino signal events with all of the selection criteria other than the time cut. Figure 8.5 shows the time separation between prompt and delayed events, fit to the exponential delayed neutron capture and a constant accidental coincidence rate. A capture time of 190 ± 12 ms is obtained. The relative proportions of time correlated and uncorrelated events are consistent with estimates.

8.3.3 Prompt-Delayed Event Spatial Separation

The prompt and delayed interactions for inverse β -decay occur within centimeters of each other. The reconstructed positions should be within tens of centimeters when reconstruction resolution is included. Accidental backgrounds are suppressed with a cut on the separation distance. Calibration source event distributions are used to estimate the

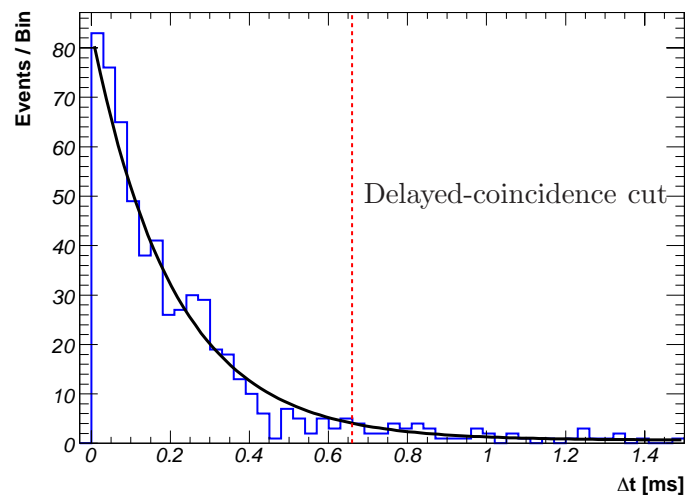


Figure 8.5: The temporal separation between prompt and delayed events are fit to a model of delayed events due to neutron capture (exponential, $\tau = 207 \mu s$) and accidental coincidences (flat background). The antineutrino delayed event cut is within $0.660 \mu s$ of the prompt event.

spatial separation. Events from the ^{68}Ge positron annihilation source are a good indicator of the prompt event distribution since the annihilation gamma rays have the least localized interaction produced by all positrons in the detector.

Neutron captures on ^1H from an ^{241}Am - ^9Be source are used to represent the delayed event distribution. Figure 8.6 shows an estimate of the relative distance between prompt and delayed events from convolving the source distributions, assuming no angular correlation. The requirement that the two events are reconstructed within 1.6 m has an efficiency of 0.991 ± 0.002 . The energetic neutrons from ^{241}Am - ^9Be produce a broader position distribution than that expected from inverse beta decay. A systematic of 0.5% is estimated from the detector position resolution for lower energy gamma sources. Figure 8.7 shows the distance between prompt and delayed interactions for the antineutrino signal. The few events outside of the selected region are consistent with accidental coincidences.

8.3.4 Prompt and Delayed Interaction Energies

To avoid the geoneutrino background, and the increasing number of accidental coincidence events at low energies, a visible energy threshold of 2.7 MeV ($\approx 2.6\text{ MeV}$ positron) is imposed. The uncertainty from the threshold is estimated by varying the detector energy response when estimating the expected reactor antineutrino prompt spectrum.

The delayed neutron capture on ^1H can be identified with high efficiency since it is a mono-energetic signal ($2.2\text{ MeV } \gamma$). Based on the spectrum of spallation neutron capture events within the target volume, a visible energy window from 2.04 MeV to 2.82 MeV selects the delayed events. The efficiency of this selection is 0.997 ± 0.002 . An additional related efficiency is the fraction of neutrons that capture on ^1H . Considering the scintillator

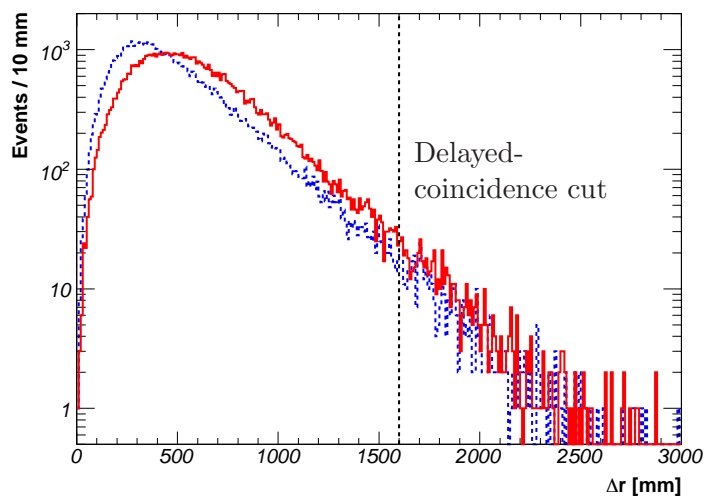


Figure 8.6: The position of neutron captures on ^1H from a ^{241}Am - ^9Be source estimates the delayed event distribution (dashed). This distribution is convolved with the ^{68}Ge positron annihilation distribution to estimate the $\bar{\nu}_e$ prompt and delayed event spatial separation (solid). Events closer than 1.6 m are selected for the antineutrino signal, reducing accidental backgrounds.

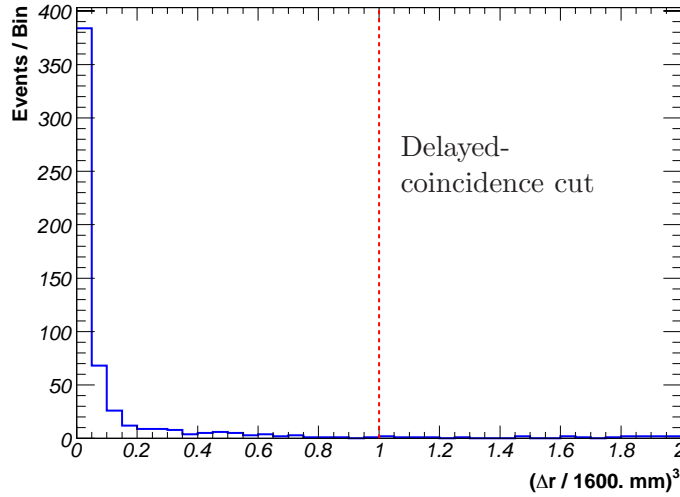


Figure 8.7: Selection cut based on the spatial separation of prompt and delayed events.

molecular composition as described in Sec. 7.2, 0.53% of neutrons capture on ^{12}C . Captures on other nuclei are negligible. The ^1H capture efficiency is 0.995 ± 0.001 .

Figure 8.8 presents the prompt and delayed energies for the interactions in the antineutrino signal. The prompt energies extend out to $\sim 8 \text{ MeV}$ as expected. The delayed energies are located in a narrow band around the 2.2 MeV neutron capture on ^1H gamma energy. The accidental coincidences rate is low above the energy threshold cut.

8.3.5 Target Volume Selection

The accidental coincidence background rises at the edges of the scintillator volume. The probability of the prompt or delayed $\bar{\nu}_e$ interaction energy escaping the scintillator volume grows near the balloon boundary ($r \sim 6.5 \text{ m}$), so the analysis is limited to a 5.5 m

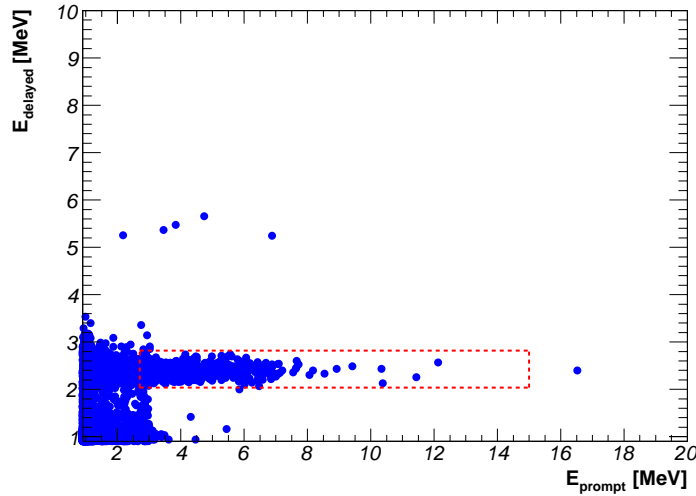


Figure 8.8: Scatter plot of the visible energies of prompt and delayed events of the neutrino candidates. The antineutrino events should lie in the region $2.7 < E_{\text{prompt}} < 15.0 \text{ MeV}$ and $2.04 < E_{\text{delayed}} < 2.82 \text{ MeV}$. Neutron capture on ^{12}C ($4.4 \text{ MeV } \gamma$), 0.53% of the ^1H rate, is consistent with the four events with high E_{delayed} .

diameter spherical volume. Specifically, when the mean reconstructed radius of the prompt and delayed event pair is larger than 5.5 m , the delayed-coincidence event is rejected. This criteria serves to define the target volume for calculating the exposure. The physical target volume measurement introduces the largest systematic uncertainty.

Figure 8.9 displays the mean position of the prompt and delayed event pairs with all the selection criteria applied except for the target volume cut. As expected, the distribution is uniform within the target volume and increasing near the scintillator boundary because of random coincidences.

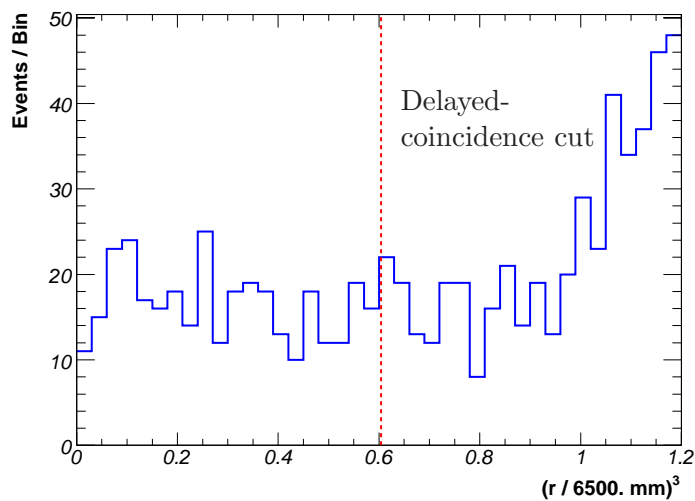


Figure 8.9: Mean position of the prompt and delayed event pairs with all the selection criteria applied except for the target volume cut. Pairs within $r = 5.5 m$ (dashed line) are selected for the $\bar{\nu}_e$ analysis. The distribution is uniform within statistics inside the target volume. The rate increases near the boundary because of accidental coincidences.

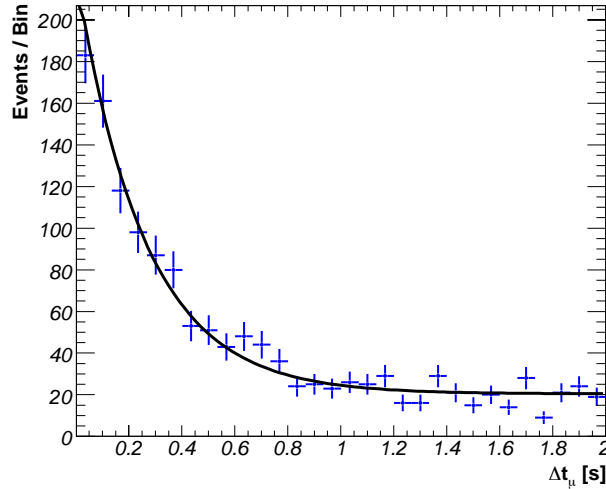


Figure 8.10: The time since muons in the scintillating volume for all of the reactor antineutrino candidates. A fit of the half-life gives 0.20 ± 0.02 s, consistent with ${}^9\text{Li}$. Fixing the half-life to $0.178.3$ s, 782 ± 35 time correlated ${}^9\text{Li}$ decays are fit.

8.3.6 Muon Spallation

The muon-induced radioactivity of the detector is rejected by ignoring the data following muon events. A 2 ms veto following all inner and outer detector muon events reduces the spallation neutron rate by a factor of 6.4×10^{-5} based on the measured capture time of $207 \mu\text{s}$. This removes spallation neutrons as a significant source of background. The loss of livetime due to the veto is negligible. A 2 ms veto following muon events with a rate of 0.64 Hz decreases livetime by only 0.1% .

Figure 8.10 shows the time since muons in the scintillating volume for all of the reactor antineutrino candidates. The contribution correlated with muons is 782 ± 35 events, and has the expected half-life of ${}^9\text{Li}$ (178.3 ms).

${}^9\text{Li}$ decays near the muon track, so the veto is only applied after muon events in the liquid scintillator. A 2 s veto rejects 99.96% of the ${}^9\text{Li}$ background. The rate of muons

in the scintillator is 0.20 Hz (see Table 7.1). A simple 2 s veto applied following each muon would reduce the livetime drastically, so a more complex rejection method is used.

As shown in Sec. 7.5, most ${}^9\text{Li}$ nuclei are associated with showering muons. Figure 8.11(a) shows the time since all showering or poorly-tracked muons for the delayed-coincidence events. Although this sample is only 11.6% of the muon events, these events produce most of the ${}^9\text{Li}$ (756 ± 30 events). The number of ${}^9\text{Li}$ produced following the remaining well-tracked minimum-ionizing muon events is estimated to be 35 ± 15 (see Fig. 8.11(b)).

For the minority of muon events which produce most of the ${}^9\text{Li}$, the entire detector is ignored for 2 s to veto this background. For well-tracked muons, the spatial correlation of the ${}^9\text{Li}$ decay with the muon track is exploited. The ${}^9\text{Li}$ is produced near to the muon trajectory within the detector. The perpendicular distance of ${}^{12}\text{B}$ decays from the reconstructed muon track supports this hypothesis (see Fig. 8.12). 95% of the ${}^{12}\text{B}$ decays have a reconstructed position within 3 m of the muon track. All prompt $\bar{\nu}_e$ events reconstructed within 3 m of the muon track are rejected for 2 s following the muon event. The livetime loss due to the muon veto is discussed in Sec. 8.5.

8.3.7 Antineutrino Candidate Events

A total of 550 antineutrino candidate events are obtained for the entire data set. Table 8.1 is a summary of the efficiency of $\bar{\nu}_e$ selection. The combined efficiency is 0.943 ± 0.006 . The following section discusses estimates of the remaining unsubtracted backgrounds.

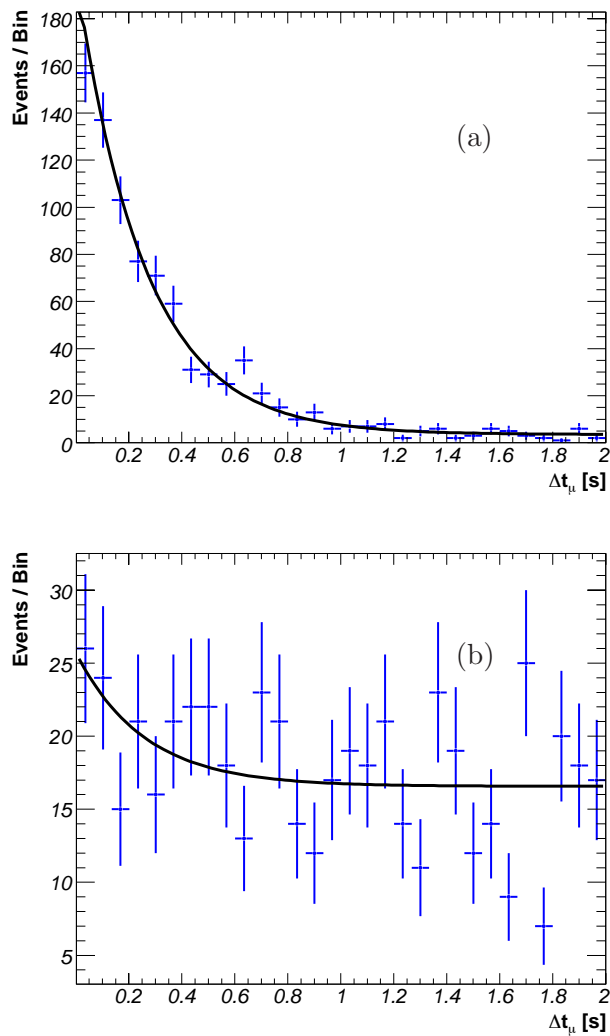


Figure 8.11: The time interval between muons in the scintillator and reactor antineutrino candidates. (a) The time correlation with showering or poorly-tracked muon events (11.6% of muons). (b) Well-tracked muon events (88.4% of muons).

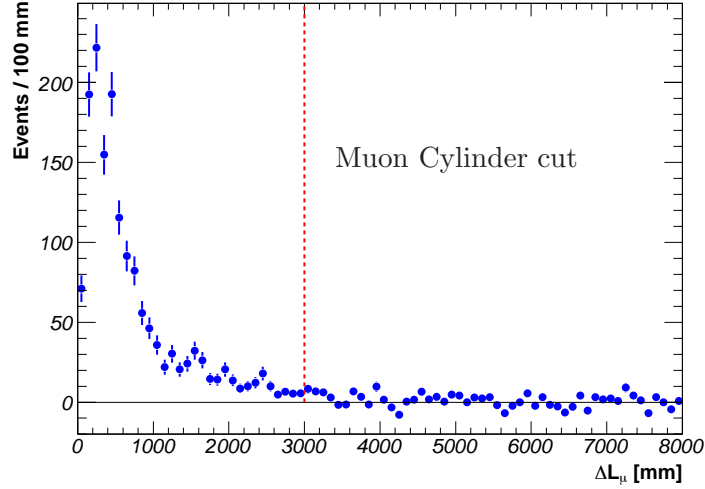


Figure 8.12: The distance between ^{12}B decays and the associated muon track. The width of this distribution reflects the perpendicular distance of the production site of ^{12}B from the muon track, the ^{12}B beta decay position, and the muon track reconstruction resolution.

Table 8.1: Reactor Anti-neutrino Event Selection

Cut	Description	Efficiency
Vertex ΔR	$\Delta R < 1.6 m$	0.995 ± 0.005
Δt	Prompt/Delayed event $0.5 \mu s < \Delta t < 660 \mu s$	0.956 ± 0.001
$^1\text{H}(n,\gamma)^2\text{H}$	Delayed Neutron Capture on Proton Efficiency	0.995 ± 0.001
Good Vertex	Reconstruction Efficiency	0.999 ± 0.001
E_d	Delayed Event Energy	0.997 ± 0.002
Combined		0.943 ± 0.006

8.4 Residual Background Estimation

The event selection procedure eliminates most of the background. Estimates of the remaining background are discussed in this section.

8.4.1 Accidental Coincidences

Characterizing the accidental background has two parts. First, the accidental coincidence rate is determined. Using the event rate, the rate of uncorrelated event pairs within $660 \mu s$ is estimated.

Second, the random coincidence spectrum is constructed. All of the events in a given run are randomly paired, ignoring the actual relative time of the events. An event pair which does not satisfy the antineutrino selection conditions is rejected. The fraction of constructed pairs satisfying the cuts is multiplied by the time-coincident rate. The results is 18 ± 1 expected accidental background events above the $2.7 MeV$ prompt event energy threshold. The prompt energy spectrum of the event pairs satisfying the selection conditions produces the spectrum shown in Fig. 8.13.

8.4.2 ${}^9\text{Li}$ Background

A simple estimate of the number of ${}^9\text{Li}$ events which survive the spallation cuts is obtained from the spectrum of candidate event time to previous muons shown in Fig. 8.14. The number of time-correlated ${}^9\text{Li}$ events is 4 ± 10 .

With other assumptions, a more precise estimate comes from calculating the efficiency of the muon veto. With the known ${}^9\text{Li}$ lifetime, the efficiency of the $2 s$ time cut,

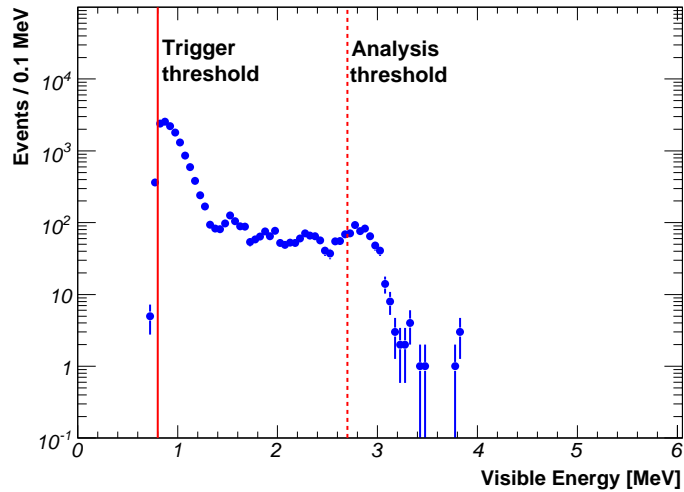


Figure 8.13: The constructed prompt event energy spectrum for accidental coincidence events. The spectrum is determined by randomly pairing singles events, applying the reactor antineutrino selection criteria.

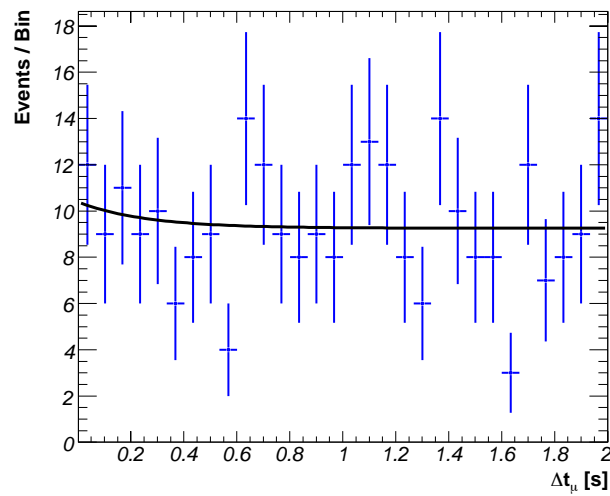


Figure 8.14: Spectrum of the time interval of candidate antineutrino events to previous inner detector muons. The number of ${}^9\text{Li}$ events is 4 ± 10 from the fit.

ϵ_t , is 99.96%. The efficiency of the 3 m veto around the muon track is determined from the perpendicular distance of ^{12}B decays from the associated muon track. 95% of the ^{12}B decays have a reconstructed position within 3 m of the muon track (Fig. 8.12). The ^9Li is produced by different nuclear interactions than ^{12}B , which in principle could lead to a different radial distribution. A conservative 5% systematic uncertainty is obtained by varying the distance of the ^{12}B event from the muon track by ± 1 m. The efficiency of the spatial correlation with the muon track, ϵ_s , is $95 \pm 5\%$. The number of ^9Li events following the showering and poorly-tracked muon events, N_a , is 756 ± 30 , and the number of ^9Li events following the well-tracked muon events, N_b , is 35 ± 15 (Fig. 8.11). The estimate of the number of unrejected ^9Li backgrounds which are not rejected by the muon veto is,

$$N_c = (1 - \epsilon_t)N_a + (1 - \epsilon_t\epsilon_s)N_b, \quad (8.1)$$

$$\simeq 2.1 \pm 1.9, \quad (8.2)$$

consistent with but more precise than the previous estimate. The total ^9Li background in the candidate data is estimated to be 2 ± 2 events.

8.4.3 $^{13}\text{C}(\alpha, n)$ -induced Backgrounds

The rate of the $^{13}\text{C}(\alpha, n)$ background depends on the rate of energetic ^{210}Po α -particles. ^{210}Po , with a half-life of 138.4 days, decays emitting 5.304 MeV α -particles. The rate of ^{210}Po decay is estimated by fitting the quenched α energy peak observed during dedicated low-threshold runs. Normally the threshold is set above the energy of these α particles. Fig. 8.15 shows the spectrum, with a fit yielding 39.5 ± 1.6 ^{210}Po decays per second in the 5.5 m-radius target volume.

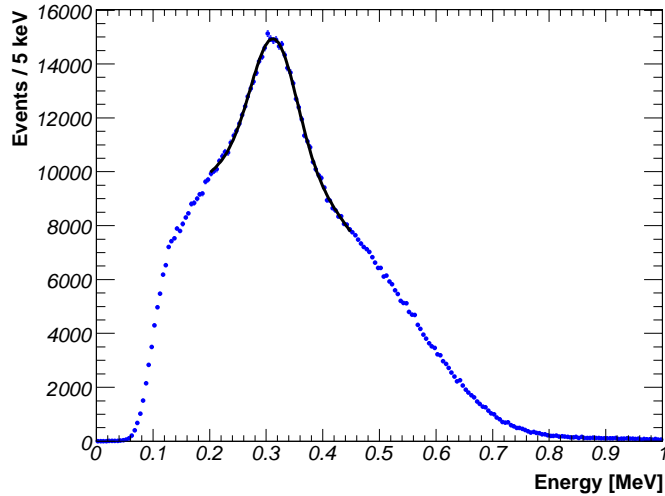


Figure 8.15: The spectrum of α -particles attributed to ^{210}Po decays. The data was obtained with a detector threshold of $\sim 0.1\text{ MeV}$. A 15% uncertainty in the yield is due to the complicated background spectrum below the α peak.

The SRIM (Stopping and Range of Ions in Matter) software package [2] was used to calculate the dE/dx as a function of α kinetic energy shown in Fig. 8.16.

The resulting α particle spectrum was integrated with the evaluated cross-section for $^{13}\text{C}(\alpha, n)^{16}\text{O}$ [79] to obtain the rate and α energies of the interactions. Incorporating the α -neutron angular correlation [85, 61], gives the spectrum of emitted neutrons shown in Fig. 8.17. The fraction of ^{16}O excited state interactions was obtained with the excited state cross-sections [79]. With the calculated rate of ^{210}Po decays in the current data set, the number of expected $^{13}\text{C}(\alpha, n)$ interactions are 194, 17, and 2 to the ground, first excited, and second excited states of ^{16}O respectively.

Constructing the expected spectrum in the KamLAND is the final step in the calculation. A simple Monte Carlo simulated neutron energy loss by multiple elastic scattering from protons and ^{12}C . Inelastic scattering on ^{12}C was included in the simulation. The neu-

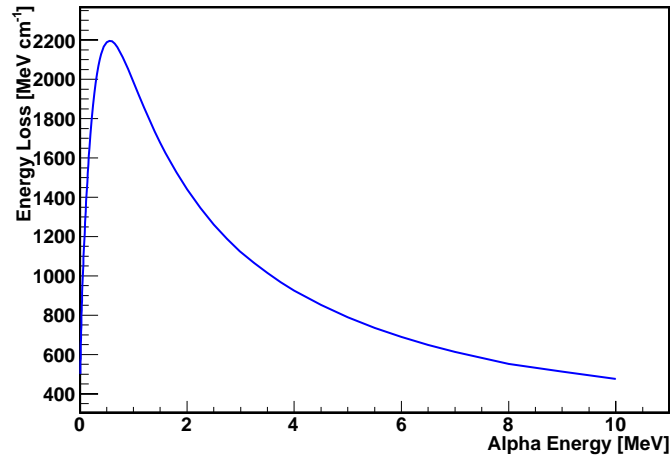


Figure 8.16: The ionization energy loss of α particles in KamLAND liquid scintillator calculated using the SRIM software package.

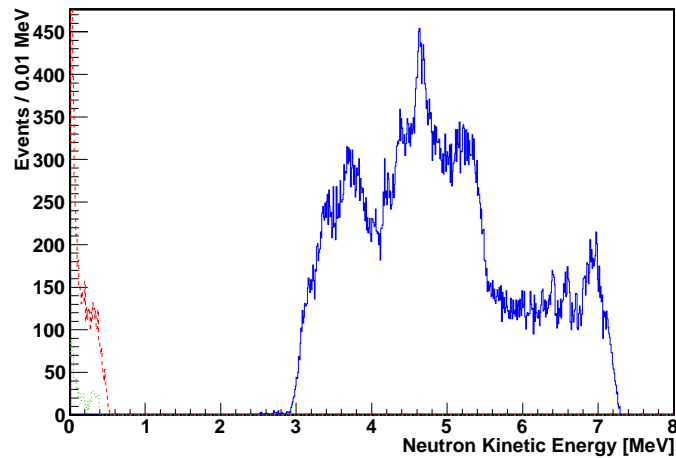


Figure 8.17: The simulated neutron kinetic energy spectrum for $^{13}\text{C}(\alpha,n)$ interactions due to 5.304 MeV α -particles. 100000 (α,n) interactions were simulated. The broad high energy peak (solid) is from the ^{16}O ground state. The low-energy neutron peaks are from the first (dashed) and second (dashed-dotted) excited states of ^{16}O .

neutron interaction cross-sections are taken from [79, 35]. The visible energy produced by each of these interactions was computed using the model of the detector response described in Sec. 6.4.4. The resulting visible energy spectrum is shown in Fig. 8.18.

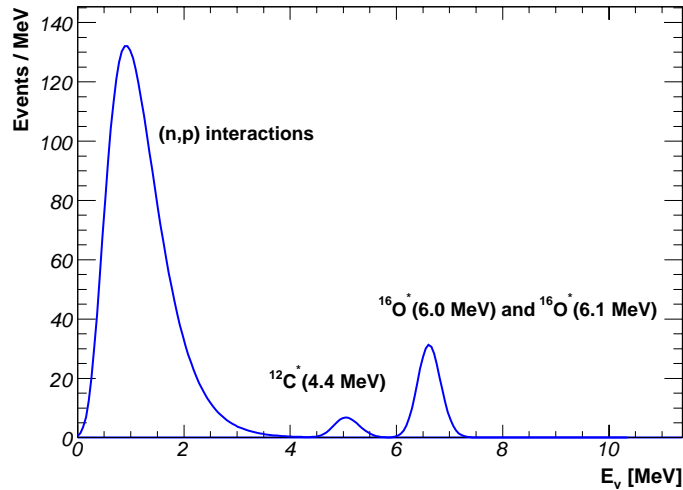


Figure 8.18: The simulated visible energy spectrum from $^{13}\text{C}(\alpha,n)$ interactions due to 5.304 MeV α -particles in KamLAND. The peaks in the spectrum come from neutron induced proton recoils and excited states of ^{12}C and ^{16}O .

8.4.4 Fast Neutrons

Fast neutron events are characterized by examining the events in the inner detector in the 2 ms following events in the outer detector. Events in the outer detector are identified by an OD $n_{summax} \geq 10$. Inner detector muons are excluded from the sample. Figure 8.19 shows the time spectrum of events following OD events. A contribution from neutron captures is not visible above the background.

Fast neutron events can be identified by an energetic (> 1000 photoelectrons)

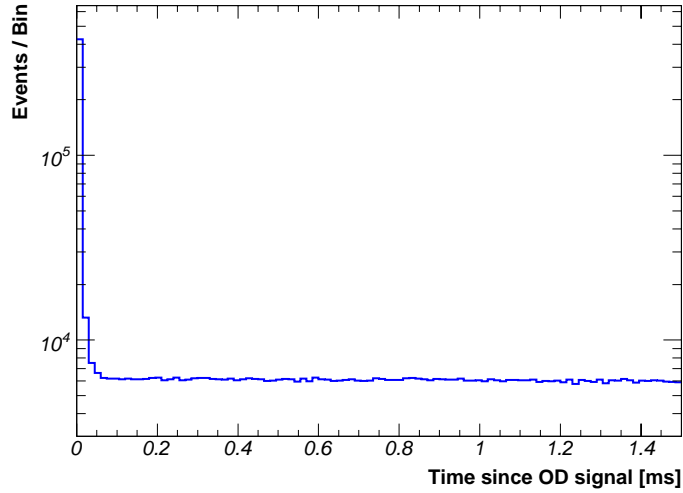


Figure 8.19: Time spectrum of inner detector events following outer detector events. Muons in the inner detector are excluded from the sample.

event in the inner detector simultaneous¹ with the outer detector signal. The time spectrum following such events shows clear evidence of neutron capture (see Fig. 8.20). Events in the following 1.5 ms window are required to have an energy greater than 2 MeV to suppress low energy backgrounds.

To mimic antineutrino events, the neutron capture must be preceded by a prompt event. The initial fast neutron scattering and slowing in the scintillator can produce the prompt signal. Multiple neutrons will also produce prompt-delayed pairs. Fast neutron coincidence pairs which satisfy all of the antineutrino cuts are backgrounds for the reactor analysis. The prompt spectrum of these events is studied by looking at the candidate events removed in the 2 ms following OD muons (see Fig. 8.21). The cuts are loosened to increase the statistics of the sample². The energy spectrum consists of an approximately

¹Simultaneous means captured within the same trigger period of about $\sim 200\text{ ns}$.

²Prompt $r < 6.5\text{ m}$, Delayed $r < 6.5\text{ m}$, $\Delta r < 2\text{ m}$, and $\Delta t < 1000\ \mu\text{s}$

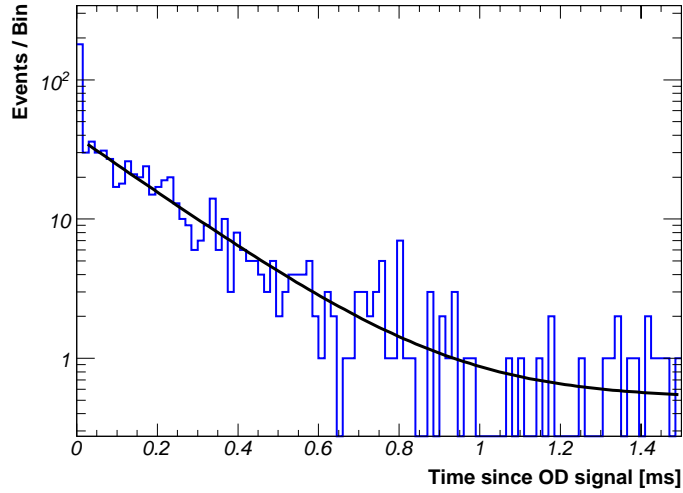


Figure 8.20: Time spectrum of inner detector events following outer detector events with a simultaneous high energy event in the inner detector. The fitted time of $0.214 \pm 0.014 \text{ ms}$ is consistent with the neutron capture time. Muons in the inner detector are excluded from the sample.

flat component, as well as a peak at the energy of the neutron capture γ -ray from ^1H . The flat component of the spectrum is due to the energy deposited by the initially fast neutron slowing in the scintillator. It occurs simultaneously with the OD signal. The peak is due to multiple neutron captures and occurs after the OD signal. This peak is below the prompt energy threshold for the reactor analysis.

The number of fast neutron events in the antineutrino data is estimated by examining the events with prompt energy above the reactor region. The fast neutron spectrum is assumed to be flat. Five candidate events have prompt visible energy between 9 and 15 MeV . Assuming a flat spectrum for fast neutron events, this implies 10 ± 5 fast neutron events with prompt energy between 2.7 and 15 MeV .

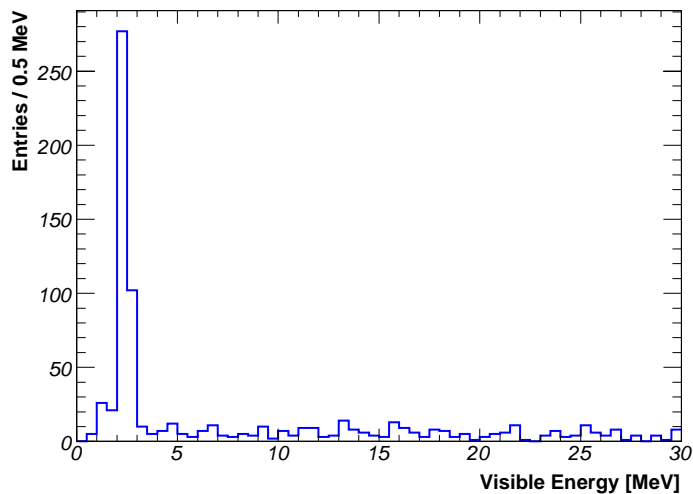


Figure 8.21: Energy spectrum of antineutrino candidates occurring in the 2 ms following OD muons.

Table 8.2: The predicted number of background events above the 2.7 MeV reconstructed energy threshold.

Background	Number of Events
Accidental Coincidences	18 ± 1
${}^9\text{Li}$	2 ± 2
${}^{13}\text{C}(\alpha, n)$	25 ± 17
Geoneutrinos	0
Fast neutrons	10 ± 5
Total	55 ± 18

8.4.5 Background Summary

Table 8.2 is a summary of the expected background events for the KamLAND reactor analysis. The largest contribution is due to the ${}^{13}\text{C}(\alpha, n)$ background.

8.5 Detector Exposure

The predicted number of inverse beta decays scales with the number of ${}^1\text{H}$ target nuclei in the fiducial volume and the total livetime. The product of volume and time, expressed in units of *proton days*, is the detector *exposure*. The exposure multiplied by the oscillated $\bar{\nu}_e$ flux and inverse beta decay cross-section gives the expected number of reactor antineutrino interactions.

8.5.1 Livetime

The data set discussed in this dissertation was collected from Apr. 2002 until May 2006. The KamLAND operating efficiency was greater than 90% during this period³. After eliminating data with poor quality, the total livetime of KamLAND was 1179.3 days, approximately 80% of the maximum possible.

8.5.2 Proton Density

The density of protons is determined by the chemical composition of the liquid scintillator. The ${}^1\text{H}$ density is 6.57×10^{28} per m^3 as given in Table 4.1. Uncertainty in the relative ratio of dodecane and pseudocumene introduce a 0.1% systematic uncertainty in the proton density. The density and temperature variation of the scintillator lead to a 1.3% systematic uncertainty.

³A high percentage of uptime is also useful to detect neutrinos from rare supernova explosions.

8.5.3 Target Volume

Only events within 5.5 m of the detector center are considered in the present analysis. The target volume is 696.9 m^3 of liquid scintillator. Candidate selection is based on the reconstructed position, not necessarily the actual interaction point. A radial bias in the reconstructed positions relative to the actual position will shift events into or out of a 5.5 m -radius target sphere. This effectively changes the size of the target. Two methods of measuring the target volume are described below. One method uses ^{12}B decays from muon spallation. The other uses a specially designed 4π calibration system.

Volume Measurement with ^{12}B

Cosmic rays produce unstable ^{12}B nuclei uniformly throughout the scintillator. The fraction of ^{12}B decays with reconstructed positions inside the 5.5 m volume relative to the total number in the entire liquid scintillator volume provides a measure of the target volume.

A critical assumption is that KamLAND is 100% efficient for detecting a ^{12}B beta decay event within the scintillator volume, and completely inefficient outside. According to simulation, beta particles which partially deposit energy at the boundary of the scintillator region introduce a 0.5% systematic uncertainty.

The volume of liquid scintillator within the KamLAND balloon is $1171 \pm 25\text{ m}^{-3}$, obtained by combining measurements of the total scintillator within the KamLAND system minus the volume of scintillator in the reserve tanks outside the detector. The final determination relies on flow meter measurements taken during filling of the detector [68].

The fraction f is the ratio of ^{12}B spallation events reconstructed inside a 5.5 m fiducial volume relative to the total. The ^{12}B spallation event selection uses a 2 ms to 52 ms time cut following an ID muon. A 4 to 20 MeV cut on visible energy excludes backgrounds. Events in coincidence with events in the outer detector ($\text{OD } n_{\text{summax}} \geq 10$) are excluded, avoiding fast neutrons. A 300 ms to 500 ms window after the muons is used for background subtraction. The volume ratio is,

$$f = \frac{s_{5.5\text{ m}} - \alpha b_{5.5\text{ m}}}{s_{\text{Total}} - \alpha b_{\text{Total}}}, \quad (8.3)$$

where s is the number of events in the signal window, b is the number of events in the background window, and α is the proper scaling of the background window (0.25). A value of 0.558 ± 0.005 is obtained with a statistical uncertainty of 0.9%. The numbers used in the expression above are respectively: 6955, 986, 13738, 6890.

The typical energies of ^{12}B events are higher than those of the reactor neutrino candidates, introducing a systematic uncertainty from a possible energy-dependent radial bias in the reconstructed position. To estimate the systematic, the ratio f is calculated for 1 MeV bins from 4 MeV to 14 MeV as shown in Fig. 8.22. The data is consistent with a constant value within statistics. Assuming that f is dependent on the reconstructed energy E , and neglecting terms quadratic and higher,

$$f(E) = a_0 + a_1 E, \quad (8.4)$$

and the uncertainty at a given visible energy is given by,

$$\sigma_f(E) = \sqrt{\sum_{i,j} \text{Cov}(i,j) \frac{\partial f(E)}{\partial a_i} \frac{\partial f(E)}{\partial a_j}}. \quad (8.5)$$

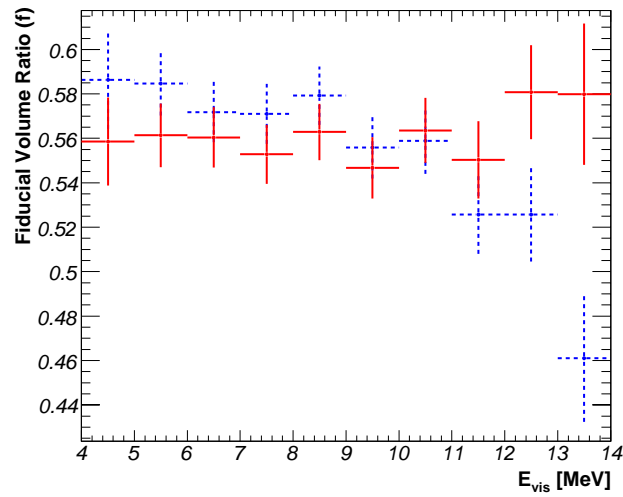


Figure 8.22: Fiducial volume ratio for 1 MeV-wide bins in ^{12}B event visible energy. The solid red points are obtained from the energy reconstruction algorithm used in this work. Shown for comparison, the dashed blue points are from a simpler energy reconstruction method, which treats PMTs as on/off binary detectors, ignoring photon statistics. The energy reconstruction method used here shows no variation with energy, while the simpler algorithm appears to be biased in energy.

A fit in the prompt $\bar{\nu}_r$ energy range of 4 to 9 MeV yields $a_0 = 0.559$ and $a_1 = 0.0000427 \text{ MeV}^{-1}$. The covariance matrix of these variables is represented in Eq. 8.5 as $Cov(i, j)$.

The mean ratio and uncertainty for reactor antineutrino events is obtained by integrating f across the expected unoscillated antineutrino spectrum $S(E)$. Using the best fit oscillated spectrum results in a negligible change in these values.

$$\langle f \rangle = \frac{\int_{E_0}^{E_1} f(E)S(E)dE}{\int_{E_0}^{E_1} S(E)dE} \quad (8.6)$$

$$= a_0 + a_1 \langle E \rangle \quad (8.7)$$

$$\simeq 0.559, \quad (8.8)$$

and

$$\langle \sigma_f \rangle = \frac{\int_{E_0}^{E_1} \sigma_{f(E)}S(E)dE}{\int_{E_0}^{E_1} S(E)dE} \quad (8.9)$$

$$\simeq 0.014. \quad (8.10)$$

This analysis gives an uncertainty of 2.5% for f . The delicate combination of a separate biases in the position and energy reconstruction could effect f without significantly distorting the distribution in Fig. 8.22. Such a balance is considered unlikely.

Multiplying the volume fraction by the total volume of liquid scintillator, a target volume of $655 \pm 22 \text{ m}^3$ is obtained. This volume is 93.9% of the 696.9 m^3 in a 5.5 m-radius sphere, with a 3.3% uncertainty.

4 π Volume Measurement

The antineutrino target volume was also measured using calibration sources. Reconstruction biases of a few mm can be determined using the 4 π calibration system. The

method is illustrated in Figure 8.23. The geometric distances between the sources along the pole are known to better than 1 mm . The known distance is compared with the reconstructed distance.

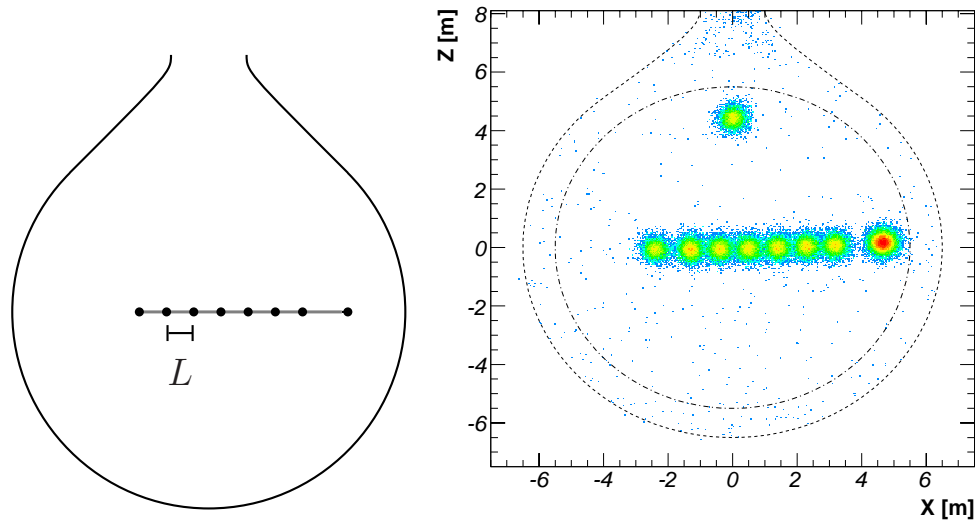


Figure 8.23: Left: Pin-to-pin position measurement. Right: Example ^{60}Co data taken using the 4π . The color represents the number of events reconstructed at each position.

Each source position is fit with a two dimensional Gaussian. Multiple Gaussians simultaneously fit all the sources in the pole and the pivot block. For a typical measurement, the statistical uncertainty of the mean position is roughly 2 mm for each source.

Figure 8.24 shows the reconstructed distance deviations between neighboring ^{60}Co sources. The reconstructed distance is consistent with the known segment length along the z-axis, except in the neck region of the detector. The pole was then oriented radially from the detector center. In these off-axis positions, the distance between neighboring sources is distorted, giving shorter distances at larger radius.

The total radial bias of the reconstruction is measured by comparing the recon-

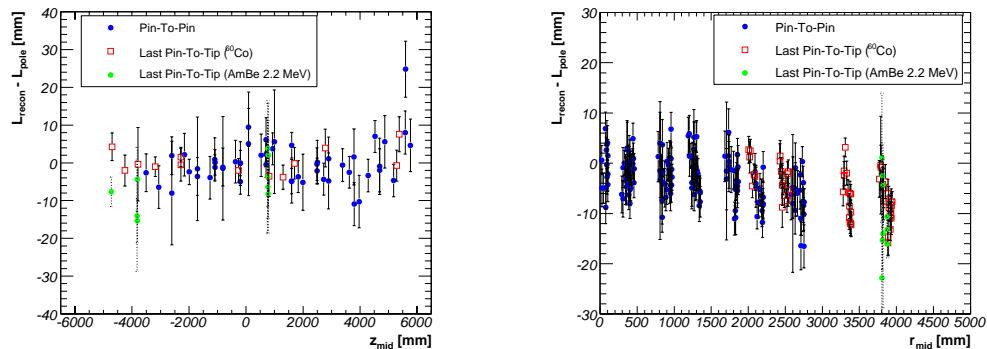


Figure 8.24: Left: The distance between neighboring ^{60}Co sources on-axis show no position bias. Right: Off-axis, neighboring sources reconstruct closer together at higher radii.

structured position of the ^{60}Co source at the end of the 4π pole with a reference pin source near the detector center. Figure 8.25 shows the results of this measurement for different 4π pole lengths. The reconstructed pole is shortened with the greatest discrepancy at roughly $r = 4.6\text{ m}$.

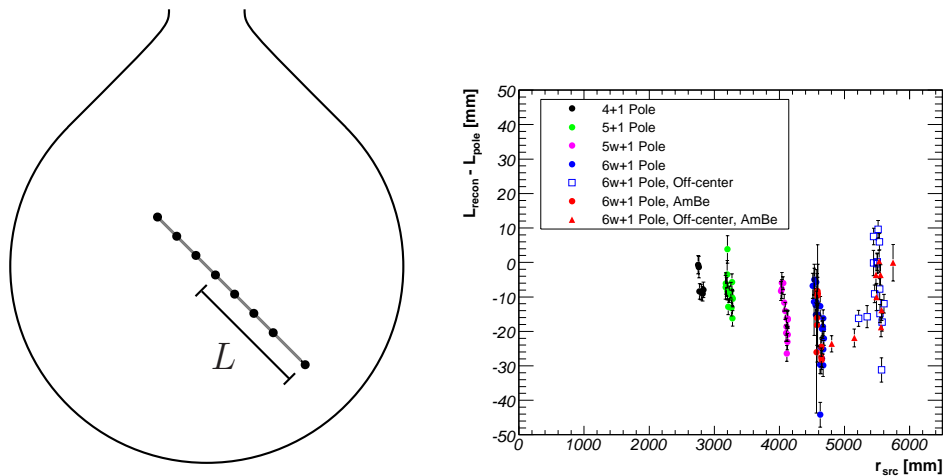


Figure 8.25: Left: Center-to-tip position off-axis measurement. Right: The distance between a reference source near the detector center and the source at the tip of the 4π system.

The maximum horizontal reach of the 4π is 4.6 m . To measure the bias at the

$r = 5.5 m$ fiducial volume boundary, the pole is raised or lowered away from the detector center. The equatorial region of the volume boundary cannot be reached. Figure 8.26 shows the positioning used to measure the radial biases at $r = 4.6 m$ and $r = 5.5 m$. The measurements with $r > 4.6 m$ in Figure 8.25 are taken in a similar manner. The off-center reconstructed pole length measures the radial bias reduced by a factor of $\cos\theta_r$, where θ_r is the angle between the pole and a radial vector.

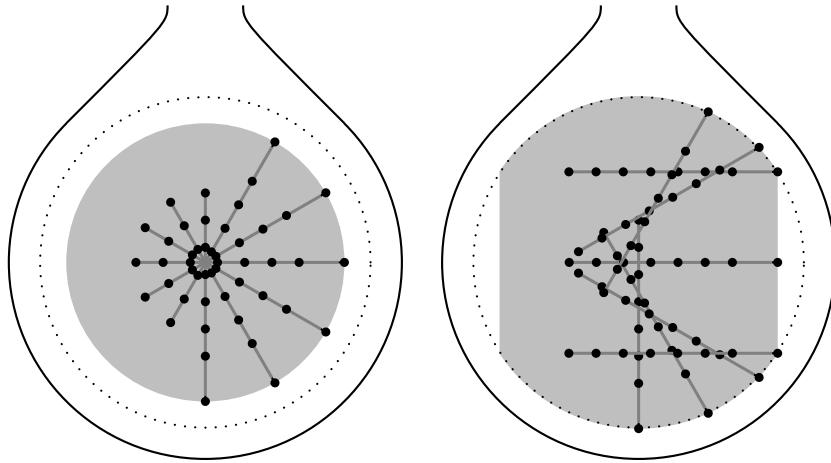


Figure 8.26: The maximum horizontal reach of the 4π system is $4.6 m$ from the central axis of the detector. Oriented radially, the pole measures the radial reconstruction bias at $r = 4.6 m$. To place the pole tip at $r = 5.5 m$ off-axis, the pole cannot be oriented radially through the detector center. The shaded regions display the region accessible by each method.

The radial reconstruction biases show trends with the pole orientation relative to zenith. Figure 8.27 shows the angular variation of the high-radius 4π measurements. The reconstructed pole length is shorter when the pole is oriented at high zenith angles. Although the trend in the radial bias has unexplained structure, all of the measurements are within the range of $10 mm$ to $-20 mm$. Extrapolating from the measurements at $r = 4.6 m$, the inaccessible equatorial region is assumed to be contained within the same range.

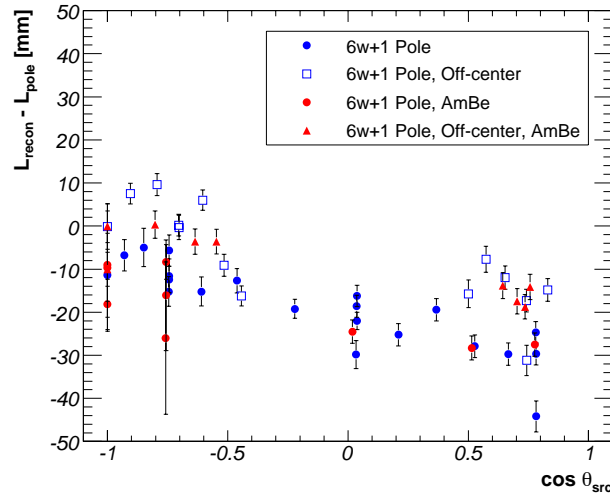


Figure 8.27: The reconstructed pole length depends on the zenith angle of the pole tip relative to the detector center. The inaccessible region at the detector equator is visible by the lack of high-radii points in the center of the figure.

A number of systematic uncertainties impact these measurements. The 2-D Gaussian fit may not correctly determine the source position. Using Monte-Carlo distributions, a 2 mm systematic uncertainty was estimated. A radial reconstruction efficiency might introduce an artificial asymmetry in the event distribution. Using calibration source deployments, no measurable variation in reconstruction efficiency was found. All of the fitting is done in the azimuthal plane defined by the pole. The uncertainty in defining the plane azimuth introduces a 1 mm systematic uncertainty in the projected pole length. The pole is not absolutely straight; it will sag slightly due to gravity. During commissioning, a deviation from straight of a few centimeters was measured for the longest pole arrangement. The sag introduces a 1 mm systematic uncertainty in the known distance between a source at the center and the source at the tip. The reference pin source is not exactly at the detector center. Variation of the radial bias within 1 m of the detector center is less than 2 mm . An

Table 8.3: 4π radial bias systematic uncertainties at $r = 5.5 m$.

	Uncertainty [mm]
Pole Length	1
Pole Bowing	1
Phi Projection	1
Fitted Position	2
Reference Source	2
Time Variation	5
Source Shadowing	5
Total	8

observed time variation of the position bias introduces an additional systematic of $5 mm$, as measured using sources on the z -axis over the lifetime of the detector. Repeated off-axis measurements are also consistent within $5 mm$, but are limited to the final 6 months of data.

Shadowing due to the pole and source container could impact the event distribution. To within $5 mm$, Figure 8.24 shows no evidence for shadowing along the z -axis, unless it is compensated by reconstruction effects. The roughly $1 cm^3$ ^{60}Co source usually produces two simultaneous gamma rays. The ^{241}Am - 9Be source container is roughly $100 cm^3$; energetic neutrons and the $2.2 MeV$ neutron capture gamma result in a broad spatial distribution. Even with the differences in shadowing, the reconstructed positions of the $2.5 MeV$ summed energy ^{60}Co gammas and $2.2 MeV$ capture gammas are consistent within $5 mm$.

Table 8.3 lists the systematic uncertainties for the differential measurement of the radial position reconstruction biases. For the ^{60}Co source at $r = 5.5 m$, the radial bias including the variation with zenith and systematic uncertainties is measured to be $-5 \pm 17 mm$.

Currently, the bias is only measured near the $2.5 MeV$ ^{60}Co energy. Measurements

using 2.2 MeV neutron capture gamma rays from an $^{241}\text{Am-}^9\text{Be}$ source are consistent within 5 mm . The bias at low energies is measured by comparing the reconstructed position of ^{68}Ge decays with ^{60}Co decays from the same source. This differential measurement avoids most systematic uncertainties associated with source positioning. At higher energies, the position of $^{241}\text{Am-}^9\text{Be}$ events with reconstructed energy from 4.5 to 7 MeV are compared to neutron captures. The relative position of 4.4 MeV and 6.1 MeV gamma rays from a $^{210}\text{Po-}^{13}\text{C}$ source were also measured.

Figure 8.28 shows the reconstructed position for ^{68}Ge decays relative to ^{60}Co events on the z -axis. The ^{68}Ge events reconstruct at higher radii, roughly 15 mm further out at $r = 5.5\text{ m}$. Figure 8.29 shows the difference for off-axis measurements. Measurements closer to the equator display a larger bias. The relative bias between the ^{68}Ge and ^{60}Co energies at $r = 5.5\text{ m}$ is taken as the range of values spanned by the measurements: $20 \pm 10\text{ mm}$.

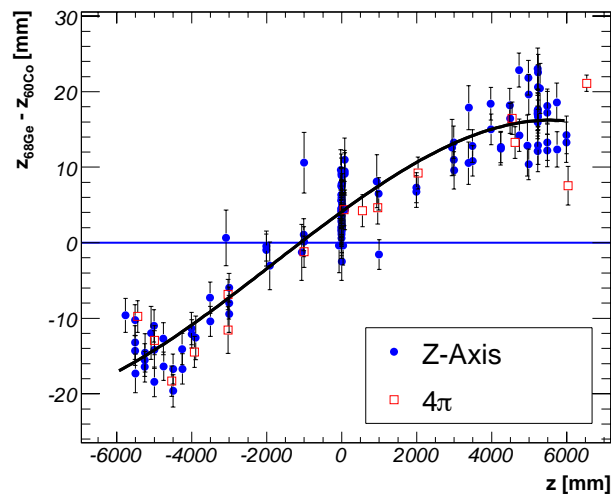


Figure 8.28: The difference in reconstructed vertical position of ^{68}Ge (1.0 MeV) and ^{60}Co (2.2 MeV) events from the same source placed on the z -axis.

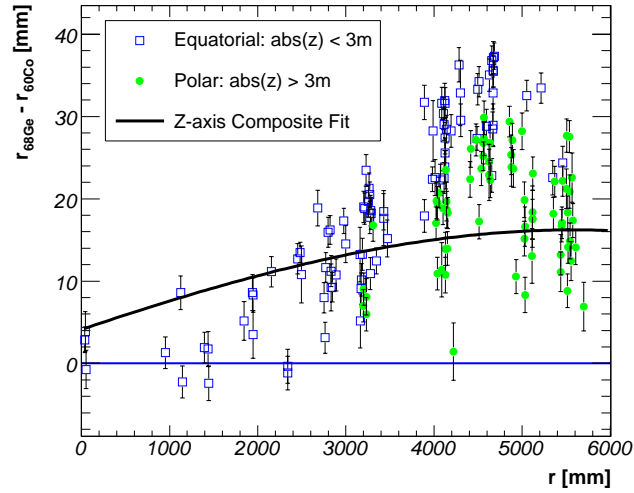


Figure 8.29: The difference in reconstructed radial position of ^{68}Ge (1.0 MeV) and ^{60}Co (2.2 MeV) events from the same source placed off-axis.

The higher energy ^{241}Am - ^9Be events reconstruct at a lower radius relative to 2.2 MeV capture gamma rays within most of the volume. Unlike ^{68}Ge , the bias reaches a maximum at a radius of $r \sim 3\text{ m}$ and is smaller near the target volume boundary (see Fig. 8.30). Off-axis, the transition is stronger as shown in Fig. 8.31. The higher energy events reconstruct at a larger relative radius beyond a radius of 5 m off-axis. The ^{210}Po - ^{13}C source 4.4 and 6.1 MeV gamma rays show a similar trend in Fig. 8.32; the radius of higher energy events is $\sim 8\text{ cm}$ further out for off-axis measurements.

Table 8.4 summarizes the radial position reconstruction bias measurements.

The radial biases determine the target volume and uncertainty. Table 8.5 summarizes the result for each source. The volume is given relative to a 5.5 m radius sphere. Considering the expected prompt antineutrino spectrum, the fiducial volume is reduced by 1% and the uncertainty is 2% in the total volume.

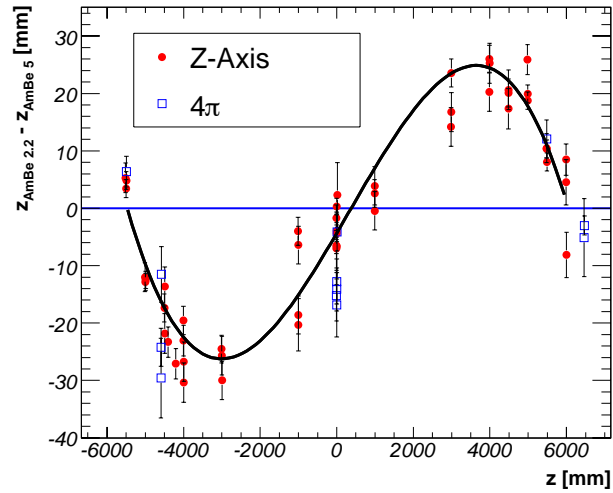


Figure 8.30: The difference in reconstructed vertical position of ^{241}Am - ^9Be neutron capture on ^1H (2.2 MeV) and higher energy (4.5 to 7 MeV) events from the same source placed on the z-axis.

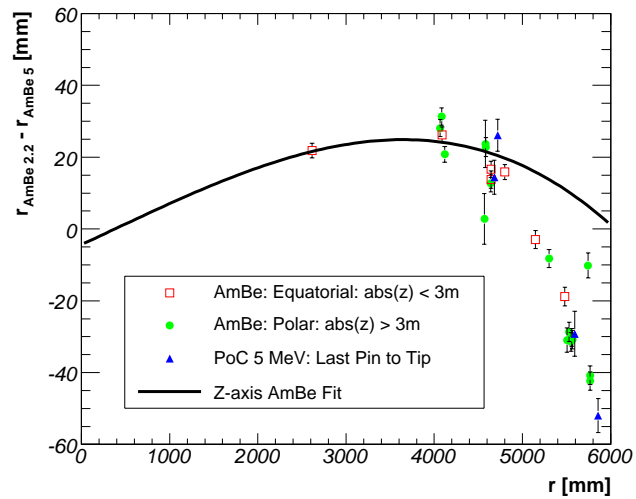


Figure 8.31: The difference in reconstructed radial position of ^{241}Am - ^9Be neutron capture on ^1H (2.2 MeV) and higher energy (4.5 to 7 MeV) events from the same source placed off-axis.

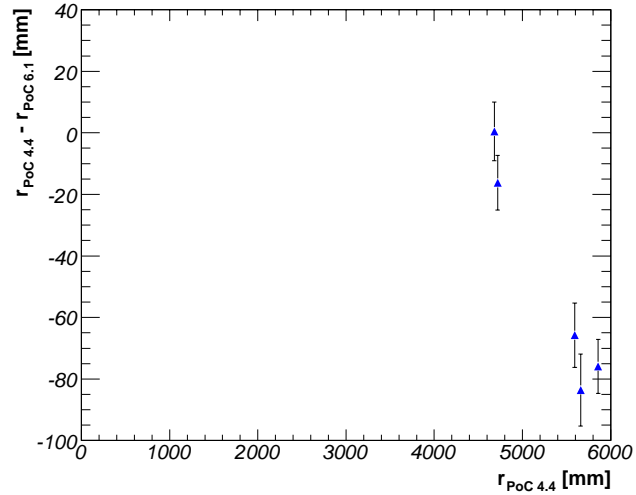


Figure 8.32: The difference in reconstructed radial position of ^{210}Po - ^{13}C 4.4 MeV and higher energy 6.1 MeV gamma rays from the same source placed off-axis.

Table 8.4: 4π radial bias measurements at $r = 5.5\text{ m}$.

Source	Radial Bias [mm]	Reference
^{60}Co , 2.5 MeV	-5 ± 17	Pin source at detector center
^{68}Ge , 1.0 MeV	20 ± 10	^{60}Co activity in same source
^{241}Am - ^9Be , 2.2 MeV	0 ± 5	Similar ^{60}Co deployments
^{241}Am - ^9Be , 4.5 – 7 MeV	30 ± 20	^{241}Am - ^9Be 2.2 MeV activity
^{210}Po - ^{13}C , 4.4 MeV	0 ± 10	Similar ^{241}Am - ^9Be deployments
^{210}Po - ^{13}C , 6.1 MeV	80 ± 20	^{210}Po - ^{13}C 4.4 MeV activity

Table 8.5: 4π Target Volume Measurement

Source	Volume Deviation [%]	Uncertainty [%]
^{60}Co , 2.5 MeV	+0.3	0.9
^{68}Ge , 1.0 MeV	-0.8	1.1
^{241}Am - ^9Be , 2.2 MeV	+0.3	1.0
^{241}Am - ^9Be , 4.5 – 7 MeV	-1.4	1.5
^{210}Po - ^{13}C , 4.4 MeV	-1.4	1.6
^{210}Po - ^{13}C , 6.1 MeV	-5.6	1.9

Table 8.6: The total KamLAND target exposure in proton days. This calculation includes the change of the volume due to radial biases in position reconstruction.

^1H Density	$6.57 \times 10^{28} \text{ protons } m^{-3}$
Target Volume	696.9 m^3
Volume Bias	0.99
Livetime	1179.3 days
Muon Veto	0.881
Exposure	$4.14 \times 10^{34} \text{ proton days}$

8.5.4 Muon Spallation

The loss of detector exposure due to the muon veto is computed using a simple Monte Carlo method. Fake $\bar{\nu}_e$ candidate events are generated uniformly through the target volume and inserted into the data. The muon cuts described above are applied to the Monte Carlo signal, and the fraction of fake $\bar{\nu}_e$ events which remain is equivalent to the remaining fraction of detector exposure. This remaining fraction of the detector exposure for the current data is 0.881 ± 0.001 .

8.5.5 Exposure Summary

Table 8.6 summarizes the total detector exposure, $4.14 \times 10^{34} \text{ proton days}$, for the current data. Table 8.7 lists the systematic uncertainties in determining the total exposure. Table 8.8 lists the uncertainties in the expected rate of inverse beta decays per target proton. The total uncertainty in the expected signal is 3.4%, and the largest contributions are from the reactor $\bar{\nu}_e$ flux (2.1%) and the fuel composition (2.5%).

Table 8.7: The systematic uncertainties in the determination of the detector exposure. The dominant component is the reconstruction bias.

^1H Density	
Scintillator Composition	0.1%
Density Variation	1.3%
Target Volume	
Reconstruction Bias	2.0%
Livetime	
Muon Veto	0.1%
Total	2.4%

Table 8.8: The systematic uncertainties in the determination of the inverse beta decay rate per target proton.

Reactor Power	2.1%
Reactor Fuel Composition	1.0%
$\bar{\nu}_e$ Spectra	2.5%
Inverse Beta Decay σ	0.2%
Total	3.4%

Chapter 9

Antineutrino Oscillation Analysis

The measured set of antineutrino candidate events are interpreted with the inferred reactor antineutrino flux in terms of the theory of neutrino oscillations. The analysis determines physical parameters of the neutrino: the mixing angle θ_{12} and the difference of the squared masses Δm_{12}^2 .

Various aspects of the experimental results constrain neutrino parameters. A *rate and shape* analysis exploits the measured rate and spectral shape to constrain the neutrino oscillation parameters. Including the time of detection of each event in a *rate, shape, and time* analysis provides an additional constraint from the variation of the flux and effective antineutrino source distance from changes in the power of particular nuclear reactors. Finally, results from KamLAND are combined with solar neutrino experiments in a *global* analysis.

9.1 The Likelihood Model

The likelihood function compares the data with the neutrino oscillation model.

The general likelihood L ,

$$L(x_i|\vec{\theta}) = \frac{1}{L_{max}} P_P(\vec{\theta}) \prod_j P_j(x_i|\vec{\theta}). \quad (9.1)$$

is expressed as the product of probability distribution functions for the rate, shape, and time components P_j . *Nuisance parameters*, parameters in the likelihood model constrained by independent measurements, introduce a probability distribution P_P . L_{max} is a normalization determined by maximum likelihood.

The likelihood describes the probability of obtaining the measurements x_i given the model parameter values $\vec{\theta}$; it may be reexpressed as an effective χ^2 , where $\chi_{min}^2 = -2\text{Log}(L_{max})$ provides the proper offset,

$$\chi^2(x_i|\vec{\theta}) = -2\text{Log}(L(x_i|\vec{\theta})), \quad (9.2)$$

$$= -2 \sum_j \text{Log}(P_j) - 2\text{Log}(P_P) + 2\text{Log}(L_{max}), \quad (9.3)$$

$$= \sum_j \chi_j^2 + \chi_P^2 - \chi_{min}^2 \quad (9.4)$$

The elements in this function are listed in Table 9.1. This table is divided into three sections: measured terms, model parameters, and model-dependent terms. Of particular importance are the parameters of the model $\vec{\theta}$. This includes the physical neutrino parameters θ_{12} and Δm_{12}^2 and a number of nuisance parameters.

Table 9.1: Parameters and terms used in the reactor antineutrino analysis.

Measured Terms	Description
N_c	Measured antineutrino candidates plus backgrounds
N_{bg_i}	Measured estimate of background events i in N_c
σ_{bg_i}	Uncertainty of estimate of N_{bg_i}
ϵ_c	Measurement of efficiency for both $\bar{\nu}_e$ and backgrounds
σ_{ϵ_c}	Uncertainty of common efficiency
ϵ_r	Measured reactor antineutrino detection efficiency
σ_{ϵ_r}	Uncertainty of reactor antineutrino efficiency
α_j	Measured detector energy response parameters (4)
$\text{cov}[\alpha_j, \alpha_k]$	Covariance matrix for energy response parameters
Model Parameters: $\vec{\theta}$	
$\hat{\theta}_{12}$	Solar mixing angle
$\widehat{\Delta m_{12}^2}$	Solar difference in squared masses
$\hat{\theta}_{13}$	Neutrino mass eigenstates 1 and 3 mixing angle
$\hat{\alpha}_j$	Detector energy response parameters (4)
\hat{N}_{bg_i}	Number of events of background i
$\hat{\epsilon}_c$	Event detection efficiency for both $\bar{\nu}_e$ and backgrounds
$\hat{\epsilon}_r$	Additional efficiency for reactor antineutrino detection
$\hat{\Phi}_l$	Standard Solar model parameters (3)
Model-Predicted Terms	
$\hat{N}_a(\vec{\theta})$	Number of expected antineutrino events
$\hat{N}(\vec{\theta})$	Total number of expected events ($\hat{N}_a + \hat{N}_{bg_i}$)
$S_a(E_q; \vec{\theta})$	Antineutrino prompt event visible energy spectrum ^a
$S_{bg_i}(E_q; \vec{\theta})$	Visible energy spectrum of background i ^a
$R_a(t; \vec{\theta})$	Instantaneous rate of antineutrino events at time t
$R_{bg_i}(t; \vec{\theta})$	Instantaneous rate of background i events at time t
$R(t; \vec{\theta})$	Instantaneous rate of events at time t ($R_a(t) + R_{bg_i}(t; \vec{\theta})$)
$St_a(E_q, t; \vec{\theta})$	Instantaneous antineutrino visible energy spectrum ^b
$St_{bg_i}(E_q, t; \vec{\theta})$	Instantaneous background visible energy spectrum ^b

^aNormalized to unity over candidate energy range.^bNormalized to unity over candidate energy range and time.

9.1.1 Nuisance Parameter Penalty

The nuisance parameters are allowed to vary within a distribution constrained by the penalty terms. This procedure ensures for proper correlation of uncertainties, as well as propagation of uncertainties to the final neutrino oscillation parameter estimates. This penalty term is constructed,

$$\begin{aligned} \chi_P^2(\vec{\theta}) = & \sum_i \left(\frac{N_{bg_i} - \widehat{N}_{bg_i} \frac{\epsilon_c}{\widehat{\epsilon}_c}}{\sigma_{bg_i}} \right)^2 + \left(\frac{\epsilon_c - \widehat{\epsilon}_c}{\sigma_{\epsilon_c}} \right)^2 + \left(\frac{\epsilon_r - \widehat{\epsilon}_r}{\sigma_{\epsilon_r}} \right)^2 \\ & + \sum_i \sum_j \text{cov}^{-1}[\alpha_i, \alpha_j] (\alpha_i - \widehat{\alpha}_i) (\alpha_j - \widehat{\alpha}_j). \end{aligned} \quad (9.5)$$

The correlation of the common efficiencies, such as the fiducial volume uncertainty, is properly applied to all of the background components via the term ϵ_c . It is important that the individual uncertainties in the numbers of background events σ_{bg_i} do not include these correlated uncertainties.

9.1.2 Rate Term

The probability of detecting N_c events given \widehat{N} expected events is just given by Poisson statistics,

$$P_R(N_c | \vec{\theta}) = \frac{e^{-\widehat{N}(\vec{\theta})} \widehat{N}(\vec{\theta})^{N_c}}{N_c!}. \quad (9.6)$$

The expected number of neutrino events $\widehat{N}(\vec{\theta})$ is just the sum of the estimated antineutrino events and backgrounds computed as,

$$\widehat{N}(\vec{\theta}) = \widehat{N}_a(\vec{\theta}) + \sum_i \widehat{N}_{bg_i}. \quad (9.7)$$

The expected number of reactor neutrino events is computed by multiplying the expected reactor neutrino spectrum by the cross-section for inverse beta decay. The prompt positron

spectrum is convolved with the detector energy response to give a spectrum in visible energy identical to $S_a(E_q; \vec{\theta})$, normalized to events per MeV per target proton. The method of estimating this spectrum was described in Chap. 5. This spectrum is then integrated within the prompt energy cuts used to select the candidate events. The result is multiplied by the number of target protons, and by the common and antineutrino detection efficiencies.

9.1.3 Unbinned Spectral Shape Likelihood

Including the unbinned spectral shape component in the analysis is straightforward; the only subtlety is in the normalization. The individual spectral components must have the proper relative normalization. Furthermore, the total spectrum normalization must be independent of the model parameters $\vec{\theta}$, otherwise it will distort the rate component of the likelihood. The resulting probability distribution can be written as a function of the antineutrino candidate event visible energies E ,

$$P_S(E|\vec{\theta}) = \frac{1}{\widehat{N}(\vec{\theta})} \sum_{a,bg_i} \widehat{N}_{a,bg_i}(\vec{\theta}) S_{a,bg_i}(E|\vec{\theta}). \quad (9.8)$$

9.1.4 Unbinned Spectral Shape and Time Likelihood

Once the spectral shape probability distribution has been constructed, it is simple to extend this to include the time of the event t . The individual spectra S are replaced with the instantaneous spectra St based on the data provided by the Japanese reactor facilities. Furthermore, the relative normalization is determined by the instantaneous rates R instead of the numbers of events \widehat{N}_{a,bg_i} . The probability distribution is then,

$$P_{St}(E, t|\vec{\theta}) = \frac{1}{\widehat{N}} \sum_{a,bg_i} \widehat{R}_{a,bg_i}(t|\vec{\theta}) St_{a,bg_i}(E, t|\vec{\theta}). \quad (9.9)$$

9.2 Analysis Details

9.2.1 Best Fit Parameter Estimation

The reactor analysis effective χ^2 functions are minimized using Minuit to determine the best estimate of the oscillation and nuisance parameters. The uncertainties quoted for these parameters are those returned by the Minuit Migrad procedure.

9.2.2 Goodness-of-fit Determination

The effective χ^2 constructed from an unbinned likelihood function does not determine the statistical goodness-of-fit. Therefore, for the simultaneous Rate and Shape analysis the antineutrino candidate prompt energy spectrum is binned in 20 bins of equal probability. The Baker-Cousins χ^2 [26] for the binned spectrum and rate is calculated using the unbinned best fit parameter values.

9.2.3 Confidence Regions

The neutrino oscillation parameter confidence regions are determined using a $\Delta\chi^2$ approach. The effective χ^2 is calculated over a grid of $\tan^2\theta_{12}$ and Δm_{12}^2 values. At each grid point, the nuisance parameters are allowed to vary to obtain the minimum effective χ^2 . The confidence contours for the oscillation parameters are defined by the difference in χ^2 from the best fit χ^2 .

9.3 Rate and Shape Analysis

The best fit values to the neutrino oscillation parameters of $\tan^2\theta_{12} = 0.45 \pm 0.11$ and $\Delta m_{12}^2 = (7.75 \pm 0.25) \times 10^5 \text{ eV}^2$ are obtained. The best fit to the visible energy spectrum is shown in Fig. 9.1, with the binned data overlaid. The reactor and background contributions are also individually shown: reactor antineutrino (blue), accidentals (red), ${}^9\text{Li}$ (cyan), ${}^{13}\text{C}(\alpha,n)$ (green), and total (black). The goodness-of-fit is 55%.

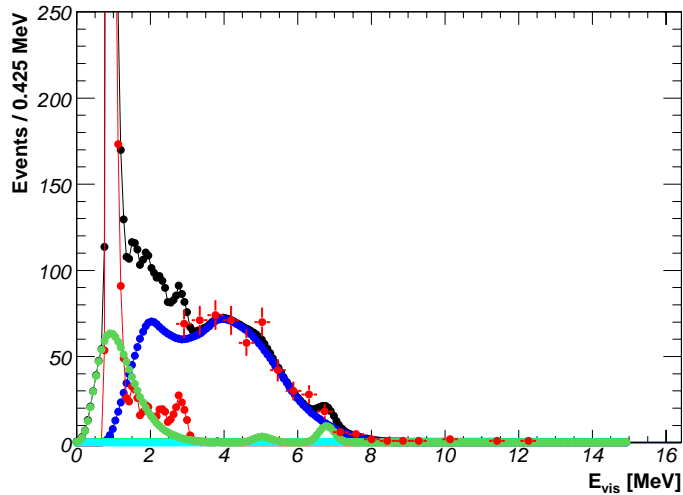


Figure 9.1: The best fit to the visible energy spectrum with the binned data overlaid. The reactor and background contributions are: reactor antineutrino (blue), accidentals (red), ${}^9\text{Li}$ (cyan), ${}^{13}\text{C}(\alpha,n)$ (green), and total (black).

Using the $\Delta\chi^2$ approach previously discussed, the allowed regions of the neutrino oscillation parameter space are identified in Fig. 9.2. The best fit values lie in the large mixing angle solution of the neutrino parameter space, in particular the central (LMA-I) region. The upper (LMA-II) region described in previous KamLAND analyses is excluded at the 3σ confidence level. The lower (LMA-0) region is still allowed at the 99% confidence

level.

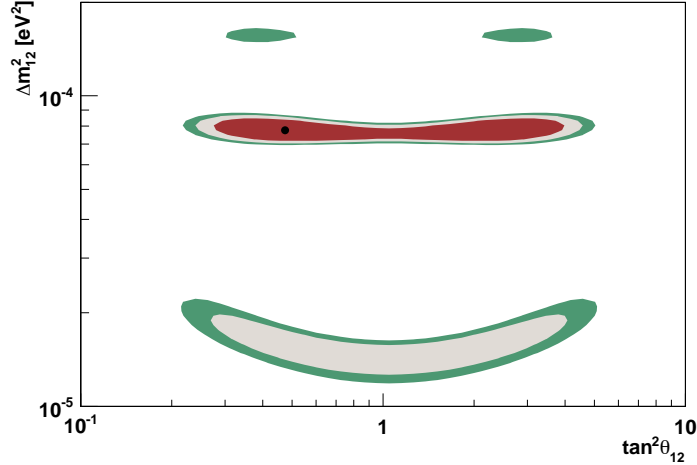


Figure 9.2: The KamLAND rate and shape analysis 95%, 99%, and 99.73% (3σ) confidence intervals. The best fit point of $\tan^2\theta_{12} = 0.45 \pm 0.11$ and $\Delta m_{12}^2 = (7.75 \pm 0.25) \times 10^5 eV^2$ is marked.

Neutrino oscillation predicts an oscillation of the electron neutrino survival probability based on the proper time in the neutrino rest frame. As discussed in Chap. 2, the proper time can be reexpressed in the laboratory by the propagation distance L divided by the neutrino energy E . Figure 9.3(a) shows the predicted oscillation signature for this theory. KamLAND detects neutrinos from 19 reactor sites located across Japan, but cannot discriminate between the sources. Figure 9.3(b) shows how the combination of two sources at different distances affects the oscillation pattern. The approximate flux-weighted mean distance L_0 of the KamLAND reactor neutrino sources is 180 km. In Fig. 9.4 the detected neutrino spectrum is binned in L_0/E . Each bin is background-subtracted and divided by the expected number of events assuming no oscillation. The value of each bin is therefore a measure of the electron neutrino survival probability. The predicted survival

probabilities of the three allowed LMA solutions are shown. Lower energy neutrino events (higher L/E) would improve the discrimination between the LMA-1 and LMA-0 solutions, but the backgrounds at lower energies must be properly characterized. Over the lifetime of the experiment, the relative flux from each reactor has changed significantly. This variation of flux alters the expected LMA solution shapes over time. In the next section, the neutrino detection time is incorporated to improve the measurement of neutrino oscillation parameters.

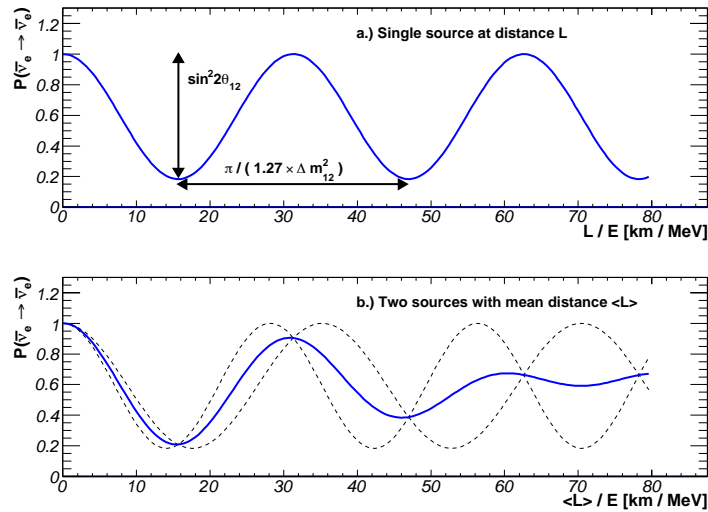


Figure 9.3: a.) The electron neutrino survival probability shown versus the propagation distance L divided by the neutrino energy E . b.) The combined survival probability due to two neutrino sources at different distances from the detector.

9.4 Rate, Shape, and Time Analysis

Given the large variation in the expected reactor neutrino flux over time, incorporating event time in the model provides an additional constraint on the neutrino

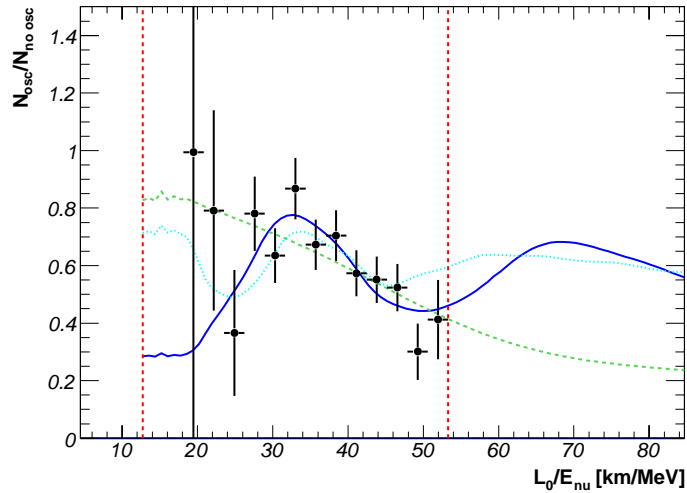


Figure 9.4: The electron neutrino survival probability versus L_0/E . The LMA-0 (dashed), LMA-1 (solid), and LMA-2 (dotted) solutions are shown. The energy range of the study is shown with the vertical dashed lines.

oscillation parameters. The resulting best fit values shift to $\tan^2\theta_{12} = 0.48 \pm 0.12$ and $\Delta m_{12}^2 = (7.72 \pm 0.24) \times 10^5 \text{ eV}^2$. The allowed parameter regions narrow slightly, yet both LMA-I and LMA-0 solutions are still allowed within the same confidence levels.

9.5 Global Analysis

KamLAND data are combined with the results of solar neutrino experiments to constrain oscillation parameters. The KamLAND results primarily constrain the difference of the squared masses, while the solar results orthogonally constrain the mixing angle. The solar neutrino flux measurements described in Chap. 3 are used. Instead of modeling the detailed MSW oscillation of neutrinos in the solar medium, an approximation can be made for oscillation parameters in the LMA region. The higher energy ^8B solar neutrinos

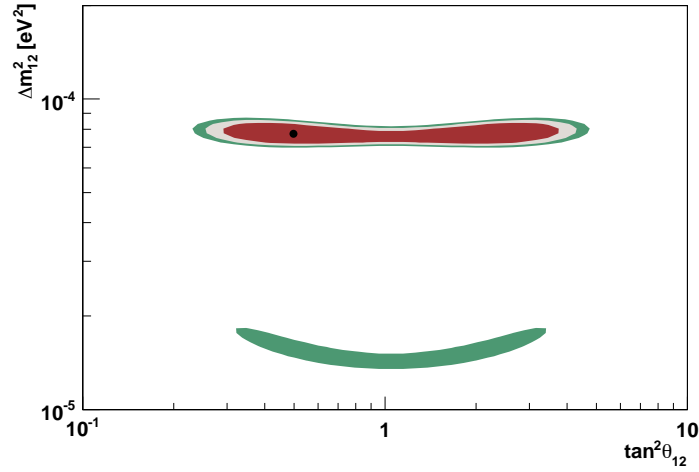


Figure 9.5: The KamLAND rate, shape, and time analysis 95%, 99%, and 99.73% (3σ) confidence intervals. The best fit point of $\tan^2\theta_{12} = 0.48 \pm 0.12$ and $\Delta m_{12}^2 = (7.72 \pm 0.24) \times 10^5 eV^2$ is marked. The inclusion of event time leads to a greater preference of neutrino oscillation parameters in the LMA-I (upper) region relative to the LMA-0 (lower) region.

are resonantly oscillated by the MSW effect. The matter-enhanced two-flavor oscillation results in a suppression of the electron neutrino flux given by,

$$P_{MSW}(\nu_e \rightarrow \nu_e) = \sin^2 \theta_{12}. \quad (9.10)$$

Lower-energy pp , pep , and ${}^7\text{Be}$ solar neutrinos are dominated by vacuum oscillation giving,

$$P_{vac}(\nu_e \rightarrow \nu_e) = 1 - \frac{1}{2} \sin^2 2\theta_{12}. \quad (9.11)$$

The best fit of the combined results are $\tan^2\theta_{12} = 0.49 \pm 0.05$ and $\Delta m_{12}^2 = (7.71 \pm 0.25) \times 10^5 eV^2$. The resulting allowed regions of the neutrino oscillation parameter are given in Fig. 9.6. The mixing angle value is dominated by the SNO charged-current to neutral-current flux ratio, which directly measures $P_{MSW}(\nu_e \rightarrow \nu_e)$.

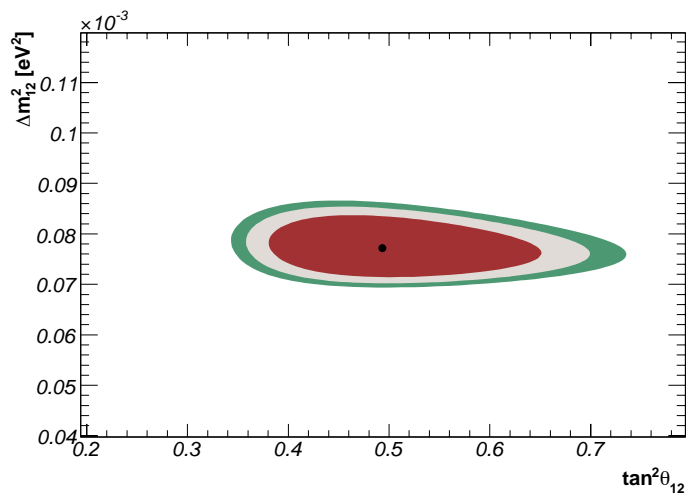


Figure 9.6: The combined KamLAND and solar experiment 95%, 99%, and 99.73% (3σ) confidence intervals. The best fit point of $\tan^2\theta_{12} = 0.49 \pm 0.05$ and $\Delta m_{12}^2 = (7.71 \pm 0.25) \times 10^5 \text{ eV}^2$ is marked.

Chapter 10

Conclusions

With the analysis presented in this dissertation, KamLAND has provided the strongest terrestrial evidence for neutrino flavor oscillation. This result culminates 50 years of reactor antineutrino experiments which began with the detection of the neutrino by Reines and Cowan. Previous experiments demonstrated that nuclear reactors produce a flux of antineutrinos understood to within 2%. No evidence of oscillation was found at distances up to 1 *km* from the reactor. Solar experiments implied that electron neutrinos were missing, and SNO showed that the ν_e were becoming ν_μ and ν_τ . Theoretical uncertainty of solar models, limited energy sensitivity of solar experiments, and the distance from the Sun prevented detection of a signature specific to oscillation.

The Kamioka mine in the Gifu prefecture of Japan provided an ideal location for a long-distance reactor $\bar{\nu}_e$ oscillation experiment. 19 Japanese reactor facilities at distances of 87 *km* to 830 *km* produce 10% of the world's total nuclear power. 1000 *m* of overburden provided 2700 *m.w.e* of shielding from cosmic rays. The delayed-coincidence signal of inverse

beta decay allowed the identification of the ~ 1 antineutrino interaction per day within 10^6 background signals.

Between Apr. 2002 and May 2006, 1179.3 days of data were collected. The 5.5 m-radius fiducial volume during this time yielded an exposure of 4.14×10^{34} *proton days*. 550 antineutrino interactions above a 3.4 MeV $\bar{\nu}_e$ energy threshold were detected, with an estimated 55 ± 18 from backgrounds. A fit to the rate and prompt spectrum of the antineutrino interactions support neutrino flavor oscillation with $\Delta m_{12}^2 = (7.75 \pm 0.25) \times 10^5 \text{ eV}^2$ and $\tan^2\theta_{12} = 0.45 \pm 0.11$. Including the daily variation of the reactor $\bar{\nu}_e$ flux gives a slightly improved estimate of $\Delta m_{12}^2 = (7.72 \pm 0.24) \times 10^5 \text{ eV}^2$ and $\tan^2\theta_{12} = 0.48 \pm 0.12$. The Large Mixing Angle solution of the solar neutrino problem is preferred. CPT invariance predicts identical oscillation for neutrinos and antineutrinos. Combining solar neutrino experiments with KamLAND, a unified analysis gives a best fit of $\Delta m_{12}^2 = (7.71 \pm 0.25) \times 10^5 \text{ eV}^2$ and $\tan^2\theta_{12} = 0.49 \pm 0.05$. Solar results constrain the mixing angle. KamLAND provides the most precise measurement of Δm_{12}^2 , and will continue to for the foreseeable future. The modulation of the detected antineutrino energy spectrum is a signature specific to neutrino oscillation, and therefore evidence of massive neutrinos.

Bibliography

- [1] <http://www2.slac.stanford.edu/vvc/egs/>.
- [2] <http://www.srim.org/>.
- [3] <http://www.ncnr.nist.gov/resources/n-lengths/>. Neutron News, Vol. 3, No. 3, 1992, pp. 29-37.
- [4] J. N. Abdurashitov et al. Measurement of the solar neutrino capture rate with gallium metal. *Phys. Rev.*, C60:055801, 1999.
- [5] J. N. Abdurashitov et al. Measurement of the solar neutrino capture rate by the Russian-American gallium solar neutrino experiment during one half of the 22-year cycle of solar activity. *J. Exp. Theor. Phys.*, 95:181–193, 2002.
- [6] A. I. Afonin et al. Anti-electron-neutrino spectra at two distances from the reactor of the Rovno nuclear power plant: Search for oscillations. *JETP Lett.*, 45:247–251, 1987.
- [7] A. A. Aguilar-Arevalo et al. A search for electron neutrino appearance at the $\Delta m^{**2} \approx 1 \text{ eV}^{**2}$ scale. 2007.
- [8] B. Aharmim et al. Electron energy spectra, fluxes, and day-night asymmetries of B-8

- solar neutrinos from the 391-day salt phase SNO data set. *Phys. Rev.*, C72:055502, 2005.
- [9] Q. R. Ahmad et al. Measurement of the charged current interactions produced by B-8 solar neutrinos at the Sudbury Neutrino Observatory. *Phys. Rev. Lett.*, 87:071301, 2001.
- [10] Q. R. Ahmad et al. Direct evidence for neutrino flavor transformation from neutral-current interactions in the Sudbury Neutrino Observatory. *Phys. Rev. Lett.*, 89:011301, 2002.
- [11] Q. R. Ahmad et al. Measurement of day and night neutrino energy spectra at SNO and constraints on neutrino mixing parameters. *Phys. Rev. Lett.*, 89:011302, 2002.
- [12] S. N. Ahmed et al. Measurement of the total active B-8 solar neutrino flux at the Sudbury Neutrino Observatory with enhanced neutral current sensitivity. *Phys. Rev. Lett.*, 92:181301, 2004.
- [13] F. Ajzenberg-Selove. Energy levels of light nuclei A=11-12. *Nucl. Phys.*, A506:1–158, 1990.
- [14] M. Altmann et al. GNO solar neutrino observations: Results for GNO I. *Phys. Lett.*, B490:16–26, 2000.
- [15] M. Altmann et al. Complete results for five years of GNO solar neutrino observations. *Phys. Lett.*, B616:174–190, 2005.
- [16] P. Antonioli, C. Ghetti, E. V. Korolkova, V. A. Kudryavtsev, and G. Sartorelli. A

- three-dimensional code for muon propagation through the rock: MUSIC. *Astropart. Phys.*, 7:357–368, 1997.
- [17] M. Apollonio et al. Initial results from the CHOOZ long baseline reactor neutrino oscillation experiment. *Phys. Lett.*, B420:397–404, 1998.
- [18] M. Apollonio et al. Limits on neutrino oscillations from the CHOOZ experiment. *Phys. Lett.*, B466:415–430, 1999.
- [19] T. Araki et al. Experimental investigation of geologically produced antineutrinos with kamland. *Nature*, 436:499–503, 2005.
- [20] T. Araki et al. Measurement of neutrino oscillation with kamland: Evidence of spectral distortion. *Phys. Rev. Lett.*, 94:081801, 2005.
- [21] T. Araki et al. Search for the invisible decay of neutrons with kamland. *Phys. Rev. Lett.*, 96:101802, 2006.
- [22] C. Athanassopoulos et al. Evidence for anti- $\nu/\mu \rightarrow \bar{\nu}_i$ anti- ν/e oscillation from the lsnd experiment at the los alamos meson physics facility. *Phys. Rev. Lett.*, 77:3082–3085, 1996.
- [23] John N. Bahcall and Carlos Pena-Garay. Global analyses as a road map to solar neutrino fluxes and oscillation parameters. *JHEP*, 11:004, 2003.
- [24] John N. Bahcall and M. H. Pinsonneault. What do we (not) know theoretically about solar neutrino fluxes? *Phys. Rev. Lett.*, 92:121301, 2004.

- [25] John N. Bahcall, Aldo M. Serenelli, and Sarbani Basu. New solar opacities, abundances, helioseismology, and neutrino fluxes. *Astrophys. J.*, 621:L85–L88, 2005.
- [26] Steve Baker and Robert D. Cousins. Clarification of the use of chi square and likelihood functions in fits to histograms. *Nucl. Instrum. Meth.*, A221:437–442, 1984.
- [27] Andrew Bazarko. Miniboone: Status of the booster neutrino experiment. *Nucl. Phys. Proc. Suppl.*, 91:210–215, 2001.
- [28] R. Becker-Szendy et al. The electron-neutrino and muon-neutrino content of the atmospheric flux. *Phys. Rev.*, D46:3720–3724, 1992.
- [29] R. M. Bionta et al. Observation of a neutrino burst in coincidence with supernova sn1987a in the Large Magellanic Cloud. *Phys. Rev. Lett.*, 58:1494, 1987.
- [30] F. Boehm et al. Final results from the Palo Verde neutrino oscillation experiment. *Phys. Rev.*, D64:112001, 2001.
- [31] F. Boehm and P. Vogel. Physics of massive neutrinos. Cambridge, UK: Univ. Pr. (1992) 249 p.
- [32] A. R. Calderbank, Ingrid Daubechies, Wim Sweldons, and Boon-Lock Yeo. Wavelet transforms that map integers to integers. *Applied and Computational Harmonic Analysis*, 5:332–369, 1998.
- [33] D. Casper et al. Measurement of atmospheric neutrino composition with imb- 3. *Phys. Rev. Lett.*, 66:2561–2564, 1991.

- [34] J. F. Cavaignac et al. Indication for neutrino oscillation from a high statistics experiment at the Bugey reactor. *Phys. Lett.*, B148:387–394, 1984.
- [35] M. B. Chadwick et al. ENDF/B-VII.0: Next generation evaluated nuclear data library for nuclear science and technology. *Nuclear Data Sheets*, 107:2931–3060, 2006.
- [36] B. T. Cleveland et al. Measurement of the solar electron neutrino flux with the Homestake chlorine detector. *Astrophys. J.*, 496:505–526, 1998.
- [37] Necia Grant Cooper. Celebrating the neutrino. *Los Alamos Science*, 25, 1997.
- [38] C. L. Cowan, F. Reines, F. B. Harrison, H. W. Kruse, and A. D. McGuire. Detection of the free neutrino: A confirmation. *Science*, 124:103–104, 1956.
- [39] G. Danby et al. Observation of high-energy neutrino reactions and the existence of two kinds of neutrinos. *Phys. Rev. Lett.*, 9:36–44, 1962.
- [40] Y. Declais et al. Search for neutrino oscillations at 15-meters, 40-meters, and 95-meters from a nuclear power reactor at Bugey. *Nucl. Phys.*, B434:503–534, 1995.
- [41] J. Detwiler. *Measurement of Neutrino Oscillation with KamLAND*. PhD thesis, Stanford University, 2005.
- [42] K. Eguchi et al. First results from kamland: Evidence for reactor anti- neutrino disappearance. *Phys. Rev. Lett.*, 90:021802, 2003.
- [43] K. Eguchi et al. A high sensitivity search for anti- ν/e 's from the sun and other sources at kamland. *Phys. Rev. Lett.*, 92:071301, 2004.
- [44] E. Fermi. An attempt of a theory of beta radiation. 1. *Z. Phys.*, 88:161–177, 1934.

- [45] E. Fermi. Trends to a theory of beta radiation. (in italian). *Nuovo Cim.*, 11:1–19, 1934.
- [46] J. A. Formaggio and C. J. Martoff. Backgrounds to sensitive experiments underground. *Ann. Rev. Nucl. Part. Sci.*, 54:361–412, 2004.
- [47] S. Fukuda et al. Constraints on neutrino oscillations using 1258 days of Super-Kamiokande solar neutrino data. *Phys. Rev. Lett.*, 86:5656–5660, 2001.
- [48] S. Fukuda et al. Determination of solar neutrino oscillation parameters using 1496 days of Super-Kamiokande-I data. *Phys. Lett.*, B539:179–187, 2002.
- [49] Y. Fukuda et al. Solar neutrino data covering solar cycle 22. *Phys. Rev. Lett.*, 77:1683–1686, 1996.
- [50] Y. Fukuda et al. Evidence for oscillation of atmospheric neutrinos. *Phys. Rev. Lett.*, 81:1562–1567, 1998.
- [51] Y. Fukuda et al. Measurements of the solar neutrino flux from Super-Kamiokande’s first 300 days. *Phys. Rev. Lett.*, 81:1158–1162, 1998.
- [52] T. K. Gaisser. Cosmic rays and particle physics. Cambridge, UK: Univ. Pr. (1990).
- [53] T. K. Gaisser and T. Stanev. Cosmic rays. *Phys. Lett.*, 592:228–234, B2004.
- [54] A. A. Hahn et al. Anti-neutrino spectra from Pu-241 and Pu-239 thermal neutron fission products. *Phys. Lett.*, B218:365–368, 1989.
- [55] K. Hirata et al. Observation of a neutrino burst from the supernova sn1987a. *Phys. Rev. Lett.*, 58:1490–1493, 1987.

- [56] K. S. Hirata et al. Experimental study of the atmospheric neutrino flux. *Phys. Lett.*, B205:416, 1988.
- [57] K. S. Hirata et al. Real time, directional measurement of B-8 solar neutrinos in the Kamiokande-II detector. *Phys. Rev.*, D44:2241–2260, 1991.
- [58] J. Hosaka et al. Solar neutrino measurements in Super-Kamiokande-I. *Phys. Rev.*, D73:112001, 2006.
- [59] F. James and M. Roos. 'minuit' a system for function minimization and analysis of the parameter errors and correlations. *Comput. Phys. Commun.*, 10:343–367, 1975.
- [60] Boris Kayser. Neutrino physics. 2005.
- [61] G. W. Kerr et al. Energy levels of ^{17}O from $^{13}\text{C}(\alpha,\alpha)^{13}\text{C}$ and $^{13}\text{C}(\alpha,n)^{16}\text{O}$. *Nucl. Phys.*, A110:637–656, 1968.
- [62] S. N. Ketov et al. Reactor experiments of a new type to detect neutrino oscillations. *JETP Lett.*, 55:564–568, 1992.
- [63] S. Klimenko, G. Mitzelmahker, and A. Sazonov. Lossless compression of ligo data. *LIGO Technical Note*, LIGO-T000076-00-D, 2000.
- [64] K. Kodama et al. Observation of tau-neutrino interactions. *Phys. Lett.*, B504:218–224, 2001.
- [65] Yu. V. Kozlov et al. Antineutrino deuteron experiment at Krasnoyarsk reactor. *Phys. Atom. Nucl.*, 63:1016–1019, 2000.

- [66] H. Kwon et al. Search for neutrino oscillations at a fission reactor. *Phys. Rev.*, D24:1097–1111, 1981.
- [67] S. P. Mikheev and A. Yu. Smirnov. Resonance enhancement of oscillations in matter and solar neutrino spectroscopy. *Sov. J. Nucl. Phys.*, 42:913–917, 1985.
- [68] T. Mitsui. Comment on vertex shift analysis using the reconstructed balloon shape. 2002.
- [69] S.F. Mughabghab, M. Divadeenam, and H.E. Holden. Neutron cross sections from neutron resonance parameters and thermal cross sections. <http://ie.lbl.gov/ngdata/sig.htm>, 1981.
- [70] K. Nakajima et al. A simple model of reactor cores for reactor neutrino flux calculations for the KamLAND experiment. 2006.
- [71] G. Nyman et al. The beta decay of Li-9 to levels in Be-9: A new look. *Nucl. Phys.*, A510:189, 1990.
- [72] Wolfgang Pauli. Pauli letter collection: letter to Lise Meitner. *CERN Archive: The Pauli Archive*, Dec. 1930. CERN-ARCH-PLC, Record Number 83282, Typed copy.
- [73] William H. Press, Brian P. Flannery, Saul A. Teukolsky, and William T. Vetterling. *Numerical Recipes in C: The Art of Scientific Computing*. Cambridge University Press, Cambridge (UK) and New York, 2nd edition, 1992.
- [74] Y. Prezado, U.C. Bergmann, M.J.G. Borge, J. Cederkall, C.Aa. Diget, L.M. Fraile, H.O.U. Fynbo, H. Jeppesen, B. Jonson, M. Meister, T. Nilsson, G. Nyman, K. Riisager,

- O. Tengblad, L. Weissmann, K. Wilhelmsen Rolander, and ISOLDE Collaboration. Large asymmetry in the strongest β -transition for $A = 9$. *Phys. Lett.*, B576:55–61, 2003.
- [75] B. Pritychenko and A. Sonzogni. Q-value calculator (QCalc). <http://www.nndc.bnl.gov/qcalc/>.
- [76] F. Reines and C. L. Cowan. Detection of the free neutrino. *Phys. Rev.*, 92:830–831, 1953.
- [77] F. Reines, C. L. Cowan, F. B. Harrison, A. D. McGuire, and H. W. Kruse. Detection of the free anti-neutrino. *Phys. Rev.*, 117:159–173, 1960.
- [78] K. Schreckenbach, G. Colvin, W. Gelletly, and F. Von Feilitzsch. Determination of the anti-neutrino spectrum from U-235 thermal neutron fission products up to 9.5-MeV. *Phys. Lett.*, B160:325–330, 1985.
- [79] K. Shibata, T. Kawano, T. Nakagawa, O. Iwamoto, J. Katakura, T. Fukahori, S. Chiba, A. Hasegawa, T. Murata, H. Matsunobu, T. Ohsawa, Y. Nakajima, T. Yoshida, A. Zukeran, M. Kawai, M. Baba, M. Ishikawa, T. Asami, T. Watanabe, Y. Watanabe, M. Igashira, N. Yamamuro, H. Kitazawa, N. Yamano, and H. Takano. Japanese evaluated nuclear data library version 3 revision-3: JENDL-3.3,. *J. Nucl. Sci. Technol.*, 39, 2002.
- [80] M. B. Smy et al. Precise measurement of the solar neutrino day/night and seasonal variation in Super-Kamiokande-I. *Phys. Rev.*, D69:011104, 2004.

- [81] D.R. Tilley, J.H. Kelley, J.L. Godwin, D.J. Millener, J.E. Purcell, C.G. Sheu, and H.R. Weller. Energy levels of light nuclei $A=8,9,10$. *Nucl. Phys.*, A745:155–362, 2004.
- [82] Nikolai R. Tolich. *Experimental study of terrestrial electron anti-neutrinos with KamLAND*. PhD thesis, Stanford University, 2005. UMI-31-62346.
- [83] P. Vogel and John F. Beacom. Angular distribution of neutron inverse beta decay, $\bar{\nu}_e + p \rightarrow e^+ + n$. *Phys. Rev.*, D60:053003, 1999.
- [84] P. Vogel, G. K. Schenter, F. M. Mann, and R. E. Schenter. Reactor anti-neutrino spectra and their application to anti-neutrino induced reactions. 2. *Phys. Rev.*, C24:1543–1553, 1981.
- [85] R. B. Walton et al. Interaction of neutrons with oxygen and a study of the $C^{13}(\alpha, n)O^{16}$ reaction. *Phys. Rev.*, 107:1065–1075, 1957.
- [86] L. Wolfenstein. Neutrino oscillations in matter. *Phys. Rev.*, D17:2369, 1978.
- [87] G. Zacek et al. Neutrino oscillation experiments at the Gösgen nuclear power reactor. *Phys. Rev.*, D34:2621–2636, 1986.

Appendix A

Lossless Compression of Waveform Data

A.1 Summary

Given the problems with data storage, transportation and even data flow rate with the KamLAND detector, reducing data size is of great importance. Described here is a method for lossless compression of waveform data to an average of 0.3 of its current size. The process combines three steps: pedestal separation, an integer wavelet transform, and Huffman encoding. Implementing this with some other minor changes reduces KDF files to 25% of their original size, with similar though slightly less compression for SF files.

Table A.1: The compression of KamLAND data files using the standard gzip routine.

File Type	File Size [MB]	.gz [MB]	Compression Ratio
KDF	268	159	0.59
SF	268	219	0.82

A.2 Introduction

Before implementing compression, the KamLAND Detector is producing an average of 3 LTO tapes (about 400 GB) of KDF and SF data per day. A large fraction (about 90%) of this is waveform data. Each waveform is a string of 128 10-bit integers (values between 0 and 1023); therefore, each uncompressed waveform is 1280 bits in length. Using a lossless compression method (wavelet transform [32] and Huffman encoding [73]), this data was compressed to an average of 384 bits per waveform, or a factor of 0.30 of its original size. This was an unoptimized first attempt, so it is likely that one can obtain even higher compression ratios. Using the standard compression program *gzip* set to the maximum compression, significantly less compression was achieved (Table A.1).

Although *gzip* is a good standard in data compression, the files are reduced to less than 80 MB by compressing using the method described. A better compression than *gzip* is obtained by using knowledge of the data structure.

A.3 Compression Method

This lossless compression method can be decomposed into two stages: entropy reduction and entropy encoding. To re-obtain the original data, these steps are reversed. This is similar to a method proposed for lossless archiving of LIGO data [63]. The premise

is that one first rewrites the data in a form which has low entropy (low redundancy), and then using this statistical information the data is encoded using a minimum number of bits. (Numbers that occur more frequently are replaced with short unique bit strings, and infrequent numbers are replaced with longer strings of bits.)

The zero-th order entropy of a set of integer data can be found from the probabilities p_i of each integer occurring,

$$H = - \sum_i p_i \ln(p_i). \quad (\text{A.1})$$

A flat distribution of integer values would have the highest entropy, and would result in no compression. The distribution of waveform ADC values can be transformed to a distribution which is far from flat. In the method described here, pedestal separation and an integer wavelet transformation [32] were used to reduce entropy, and then zero-th order Huffman encoding was used to compress the data.

A.3.1 Entropy Reduction

Pedestal Separation

Not to be confused with pedestal subtraction described in Sec. 6.1.2, pedestal separation maintains copies of integer pedestals which can then be used to restore the original data including its pedestal distortion. By removing one copy of the pedestal from all the waveforms from a specific ATWD, the entropy of these waveforms as calculated by Eq. A.1 is significantly reduced. This is because the fine structure exhibited by neighboring ADC values is an approximately constant result for each ATWD.

Integer Wavelet Transformation

Wavelets have gained fame for their ability to compress images, and are used in the current version of the JPEG image format. The method discussed in this paper does not use wavelets for compression, since this is a lossy form of compression. Here, wavelets are used solely to rewrite the 128 integers of the waveform as another set of 128 integers which have lower entropy.

There are an infinite possible set of wavelet transforms, and the 2-2 Interpolating Transform from Ref. [32] was chosen somewhat arbitrarily. One condition is that an integer to integer transformation is used since the entropy would most likely increase if an integer to real transformation was used. The 2-2 integer interpolating wavelet transform is very simple, taking only 20 lines to code with the transform itself summarized with only two equations.

A.3.2 Entropy Encoding

For expediency, the Huffman encoding routines from Numerical Recipes were used [73], and a detailed description can be found there. There are better algorithms, such as arithmetic coding, but in this process simplicity was given preference.

The Huffman algorithm takes in a table of symbols (integers in our case), and their corresponding frequency in the data to be compressed. It then generates an optimized translation table between the symbols and unique strings of bits. Encoding is done by replacing the symbols with their bit strings, and decoding is done vice-versa. Of course, this means that the translation table must be stored with the encoded data so that it can

Table A.2: The entropy of the distribution of waveform integer values under a series of operations. The first is just the raw ADC values. Next, the ATWD pedestal is subtracted from the signal. For the last two entries, the integer wavelet transform has been applied.

	Entropy
ADC Only	4.2
ADC - Ped	3.4
ADC / Wavelet	3.1
ADC - Ped / Wavelet	1.8

be later decoded. One important detail is that lossless compression done in this fashion results in a variable size for the compressed data.

A.4 Compression Results

A.4.1 Entropy Reduction Results

The entropy for four different scenarios were computed according to Eq. A.1. The integer sample data was taken from the first event (229 waveforms) of the SF file run_001222_000000_000092.sf. The first scenario is the entropy from just the ADC values themselves, the second is ADC value after pedestal separation, the third is ADC value after wavelet transformation and the last is ADC after pedestal subtraction and wavelet transformation.

A.4.2 Entropy Encoding Results

As a test, a standard frequency table was generated from the first 1000 waveforms of the previously mentioned SF file from run 1222 and this was used to compress waveforms from a different run (run_001233_000000_000374.sf). If any integer was not encountered

in this set of data, it was given a frequency of one in 1000 waveforms by default so that the encoder would not fail if it encountered it in future data. A different set of data was compressed with this table to support the idea that one standard frequency table could be used for compression of all KamLAND data. By using one frequency table some optimization is lost in compression (since the frequency table is *tuned* to the data from which it was generated), but as a benefit only one translation table must be stored for all data. This also improves the simplicity of implementation. Alternatives span the range of storing translation tables all the way down to a waveform by waveform basis, but at this point the overhead of the table negatively impacts compression.

The average compression obtained for 250,000 waveforms (1000 events) from run 1233 is 0.31. There is a long tail which goes out to a ratio of 1.6, where some waveforms actually expand instead of compress. This is most likely correlated with high energy events such as muons, which produced non-standard waveforms.

A.4.3 Speed and Reliability

The above 250,000 waveforms were compressed, decompressed and compared to their original values and no difference was found. This entire test ran in under 30 seconds on a single standard PC desktop computer.

A.5 Implementation for KamLAND

For the KamLAND data compression, a fixed Huffman table was generated from a sample data set and was hard-coded into the compression routines. A fixed set of mean

pedestal data was generated for compression use, but this was not hard-coded into the decompression software. It is instead written to the data at the beginning of every run for use in decompression.

An alternate entropy reduction transform was written by Misha Batygov to replace the integer wavelet transform. While the resulting compression ratio is similar for both transforms, the new algorithm is twice as fast. This is the transform that is currently used for compressing the KamLAND data; for the details of this transform refer to the DiffEntropyHuffmanCoDec software.